The Consultative Committee for Space Data Systems

Report Concerning Space Data System Standards

SCCC – SUMMARY OF DEFINITION AND PERFORMANCE

DRAFT INFORMATIONAL REPORT

CCSDS 130.11-G-0

DRAFT GREEN BOOK

March 2018

AUTHORITY

Issue:	Draft Green Book, Issue 0
Date:	March 2018
Location:	Not Applicable

(WHEN THIS INFORMATIONAL REPORT IS FINALIZED, IT WILL CONTAIN THE FOLLOWING STATEMENT OF AUTHORITY:)

This document has been approved for publication by the Management Council of the Consultative Committee for Space Data Systems (CCSDS) and reflects the consensus of technical experts from CCSDS Member Agencies. The procedure for review and authorization of CCSDS documents is detailed in *Organization and Processes for the Consultative Committee for Space Data Systems* (CCSDS A02.1-Y-4).

This document is published and maintained by:

CCSDS Secretariat
Space Communications and Navigation Office, 7L70
Space Operations Mission Directorate
NASA Headquarters
Washington, DC 20546-0001, USA

FOREWORD

[Foreword text specific to this document goes here. The text below is boilerplate.]

Through the process of normal evolution, it is expected that expansion, deletion, or modification of this document may occur. This document is therefore subject to CCSDS document management and change control procedures which are defined in *Organization and Processes for the Consultative Committee for Space Data Systems* (CCSDS A02.1-Y-4). Current versions of CCSDS documents are maintained at the CCSDS Web site:

http://www.ccsds.org/

Questions relating to the contents or status of this document should be addressed to the CCSDS Secretariat at the address indicated on page i.

At time of publication, the active Member and Observer Agencies of the CCSDS were:

Member Agencies

- Agenzia Spaziale Italiana (ASI)/Italy.
- Canadian Space Agency (CSA)/Canada.
- Centre National d'Etudes Spatiales (CNES)/France.
- China National Space Administration (CNSA)/People's Republic of China.
- Deutsches Zentrum für Luft- und Raumfahrt (DLR)/Germany.
- European Space Agency (ESA)/Europe.
- Federal Space Agency (FSA)/Russian Federation.
- Instituto Nacional de Pesquisas Espaciais (INPE)/Brazil.
- Japan Aerospace Exploration Agency (JAXA)/Japan.
- National Aeronautics and Space Administration (NASA)/USA.
- UK Space Agency/United Kingdom.

Observer Agencies

- Austrian Space Agency (ASA)/Austria.
- Belgian Federal Science Policy Office (BFSPO)/Belgium.
- Central Research Institute of Machine Building (TsNIIMash)/Russian Federation.
- China Satellite Launch and Tracking Control General, Beijing Institute of Tracking and Telecommunications Technology (CLTC/BITTT)/China.
- Chinese Academy of Sciences (CAS)/China.
- Chinese Academy of Space Technology (CAST)/China.
- Commonwealth Scientific and Industrial Research Organization (CSIRO)/Australia.
- Danish National Space Center (DNSC)/Denmark.
- Departamento de Ciência e Tecnologia Aeroespacial (DCTA)/Brazil.
- European Organization for the Exploitation of Meteorological Satellites (EUMETSAT)/Europe.
- European Telecommunications Satellite Organization (EUTELSAT)/Europe.
- Geo-Informatics and Space Technology Development Agency (GISTDA)/Thailand.
- Hellenic National Space Committee (HNSC)/Greece.
- Indian Space Research Organization (ISRO)/India.
- Institute of Space Research (IKI)/Russian Federation.
- KFKI Research Institute for Particle & Nuclear Physics (KFKI)/Hungary.
- Korea Aerospace Research Institute (KARI)/Korea.
- Ministry of Communications (MOC)/Israel.
- National Institute of Information and Communications Technology (NICT)/Japan.
- National Oceanic and Atmospheric Administration (NOAA)/USA.
- National Space Agency of the Republic of Kazakhstan (NSARK)/Kazakhstan.
- National Space Organization (NSPO)/Chinese Taipei.
- Naval Center for Space Technology (NCST)/USA.
- Scientific and Technological Research Council of Turkey (TUBITAK)/Turkey.
- South African National Space Agency (SANSA)/Republic of South Africa.
- Space and Upper Atmosphere Research Commission (SUPARCO)/Pakistan.
- Swedish Space Corporation (SSC)/Sweden.
- Swiss Space Office (SSO)/Switzerland.
- United States Geological Survey (USGS)/USA.

DOCUMENT CONTROL

Document	Title and Issue	Date	Status
CCSDS 130.11-G-0	SCCC – Summary of definition and performance, Draft Informational Report, Issue 0	August 2018	First draft following CCSDS Review

CONTENTS

Section Page

1 INTRODUCTION

1.1 PURPOSE AND SCOPE

It is expected that a number of *Earth Exploration Satellite Service* (EESS) missions will embark payloads producing substantial data rates, i.e., starting from a few hundred Mbps. Such missions would benefit from employing transmitters using state-of-the-art air interface that exploits link adaption, i.e., achieve high spectral efficiency by adjusting the modulation and coding to the link budget. In this respect, the *Consultative Committee for Space Data Systems* (CCSDS) developed a flexible advanced coding and modulation scheme for high rate telemetry applications [1] that offers precisely such benefits, by means of powerful serially concatenated convolutional codes (SCCC) with modulations belonging to the family of phase shift keying (PSK) and amplitude PSK (APSK), providing efficiencies up to 5.39 bit per channel symbol.

The goal of this document is to provide additional informative material for [1]. Namely, this Green Book includes a tutorial overview of CCSDS specification in [1] (aimed at helping first-time readers to understand the recommendation) together with performance information supported by illustrations.

This Report is not intended to provide all necessary knowledge for successfully designing telemetry communication links and it provides supporting and descriptive material only: this document is a CCSDS informational report and is therefore not to be taken as a CCSDS Recommended Standard. The actual Recommended Standard is in reference [1]. In the event of any conflict between the [1] and the material presented herein, the Recommended Standard [1] shall prevail.

In no event will CCSDS or its members be liable for any incidental, consequential, or indirect damages, including any lost profits, lost savings, or loss of data, or for any claim by another party related to errors or omissions in this Report.

1.2 ORGANIZATION

The remainder of this Report is organized as follows: Section 2 covers a tutorial overview of CCSDS specification in [1] (aimed at helping first-time readers to understand the recommendation), describing its main functions and parameters with focus on the encoding function, constellations and mapping, PL frame and pilot insertion, and baseband filtering. Section 3 shows the performance of the recommended codes and modulations by means of error rate curves on the linear AWGN channel assuming ideal synchronization. Then, Section 4 provides the performance on a nonlinear channel, that models nonlinear distortions due to amplification. Section 5 focuses on the synchronization chain and it provides a possible reference receiver with details on its performance on the AWGN channel with phase noise and Doppler. Finally, in Section 6 and 7 end-to-end performance is provided, while in Section 8 conclusions are drawn.

1.3 TERMINOLOGY

The terminology here adopted tries to comply with the one adopted in [1], but for the reader convenience, some of the most important terms and symbols are here reported with the aim of avoiding confusion with other meanings, sometimes adopted in other documents.

Recommended Standard	Reference to CCSDS Blue Book 131.2-B-1, for which this Green Book provides additional informative material.
Information bit	Bit at the input interface of the SCCC encoding block coming from the ACM Mode adaptation (see Figure 2-1 in Section 2).
Encoded bit	Bit at the output interface of the SCCC encoding block and at the input of the PL Framing (see Figure 2-1 in Section 2).
Channel symbol	Modulated symbol at the output of the constellation mapping.
Efficiency	Number of information bits per channel symbol, excluding physical layer (PL) signaling and pilot insertion. It shall not be confused with the classical spectral efficiency denoting the information rate per Hz of bandwidth adopted, although it is proportional to it.
ModCod	Modulation and coding format.
E_s/N_0	Signal-to-noise ratio defined as energy per channel symbol over noise power spectral density.
E_b/N_0	Signal-to-noise ratio defined as energy per information bit over noise power spectral density.
R_{chs}	Channel symbol rate, measured in MBaud.

1.4 MATHEMATICAL NOTATION

x	Scalar value (real or complex)
x^*	Complex conjugated
$\mathcal{R}(x)$	Real part
$\|x\|$	Absolute value
$\angle x$, angle(x)	Phase angle
x_k	Indexed scalar value (e.g., for indexing of signal samples)

$\{x_k\}$	Sequence of the indexed values
$x(t)$	Analog signal (as function of time)
$\oplus$	Sum modulo 2 (XOR)
$E\{\cdot\}$	Expected value

1.5 LIST OF MOST USED ACRONYMS

ACM	Adaptive coding and modulation
AOS	Advanced orbiting systems (space data link protocol)
APSK	Amplitude phase shift keying
AWGN	Additive white Gaussian noise
BER	Bit error rate
CER	Codeword error rate
DAGC	Digital automatic gain control
FD	Frame descriptor
FLL	Frequency locked loop
FM	Frame marker
IBO	Input back-off
LLR	Log-likelihood ratio
OBO	Output back-off
PL	Physical layer
PLL	Phase-locked loop
PSK	Phase shift keying
QPSK	Quadrature phase shift keying
SCCC	Serial concatenated convolutional code

SNR	Signal-to-noise ratio
SRRC	Square root raised cosine
TD	Total degradation
TWTA	Traveling wave tube amplifier

1.6 REFERENCES

The following documents are referenced in this Report. At the time of publication, the editions indicated were valid. All documents are subject to revision, and users of this Report are encouraged to investigate the possibility of applying the most recent editions of the documents indicated below. The CCSDS Secretariat maintains a register of currently valid CCSDS documents.

[1] CCSDS, "Flexible Advanced Coding and Modulation Scheme for High Rate Telemetry Applications," Recommendation for Space Data System Standards, CCSDS 131.2-B-1 Blue Book, March, 2012.

[2] Ryan, W. E., Lin S., "Channel Codes: Classical and Modern," *Cambridge University Press*, October, 2009.

[3] Benedetto, S., Montorsi, G., "Serial Concatenation of Block and Convolutional Codes," *Electronics Letters*, Vol. 32, n. 10, pp. 887-888, May, 1996

[4] Shannon, C., "A Mathematical Theory of Communication," *Bell System Technologies Journal*, pp. 379-423, July, 1948.

[5] Dolinar, S., Divsalar, D., "Weight Distributions for Turbo Codes Using Random and Nonrandom Permutations," technical note available on ntrs.nasa.gov, 1995.

[6] Holmes, J. K, "Spread Spectrum Systems for GNSS and Wireless Communications," *GNSS Technology and Applications Series*, June, 2007.

[7] Karam, G., Sari H., "A data pre-distortion technique with memory for QAM radio systems," *IEEE Transactions on Communications*, pp. 336–344, February, 1991.

[8] Ding, L. et al., "A robust digital baseband predistorter constructed using memory polynomials," IEEE Transactions on Communications, vol. 52, no. 1, pp. 159-165, January 2004.

[9] Gardner, F., "A BPSK/QPSK timing-error detector for sampled receivers," *IEEE Transactions on Communications*, pp. 423-429, May, 1986.

[10] Scholtz, R., "Frame Synchronization Techniques," *IEEE Transactions on Communications*, vol. 28, pp. 1204-1213, August, 1980.

[11] CCSDS, "Radio Frequency and modulation systems – Part 1, Earth Stations and Spacecraft," Recommendation for Space Data System Standards, CCSDS 401.0-B-27 Blue Book, October, 2017.

[12] Cioni, S., Bousquet, M., "An Analytical Characterization of Maximum Likelihood Signal-to-Noise Ratio Estimation," in proc. of *2nd International Symposium on Wireless Communication Systems*, Siena, Italy, 2009.

[13] Gardner, F., "Phaselock techniques," *Wiley-interscience*, 3rd edition, July, 2005.

[14] Casini, E., Gaudenzi, R. D. and Ginesi, A., "DVB-S2 modem algorithms design and performance over typical satellite channels," *Int. J. Satell. Commun. Network.*, Volume 2, pp. 281–318, 2004.

[15] Tesat-Spacecom, Konsberg Spacetec, "FleXLink, Multi-Gigabit Data Downlink End-to-End Chain," White Paper: Maximizing throughput in satellite to ground transmissions, June 2017.

2 OVERVIEW

This section provides a quick overview of the coding and modulation scheme of the Recommended Standard. In particular, it aims at providing additional informative material for an easier understanding of the Recommended Standard [1] and of the results shown later in this report.

This section is not meant to provide a full description of the functions needed at the sending end. It only provides a preliminary overview of some functions and for the full and detailed description the reader shall refer to [1].

2.1 FLEXIBLE ADVANCED CODING AND MODULATION SCHEME

The *Flexible Advanced Coding and Modulation Scheme for High Rate Telemetry Applications* is designed for space communications links, primarily between spacecraft and ground elements, and is based on *serially concatenated convolutional codes* (SCCC, see [2]) able to support a wide range of spectral efficiency values based on a single coding structure. The frame structure deployed by this standard is agnostic as to the protocol used at higher layer (e.g., AOS or TM) while providing support for maintaining synchronization during transition from one ModCod to another.

An overview of the functional blocks of the architecture at the sending end is shown in Figure 2-1[1]. At its input the system accepts *transfer frames* (from the Data Link protocol sublayer), it performs the functions illustrated, and deliver a continuous stream of channel symbols to the physical layer.

[1] Figure 2-1 and Figure 2-2 are taken from [1], which should be referred to for normative purpose, and they are copied here for readers' convenience only.

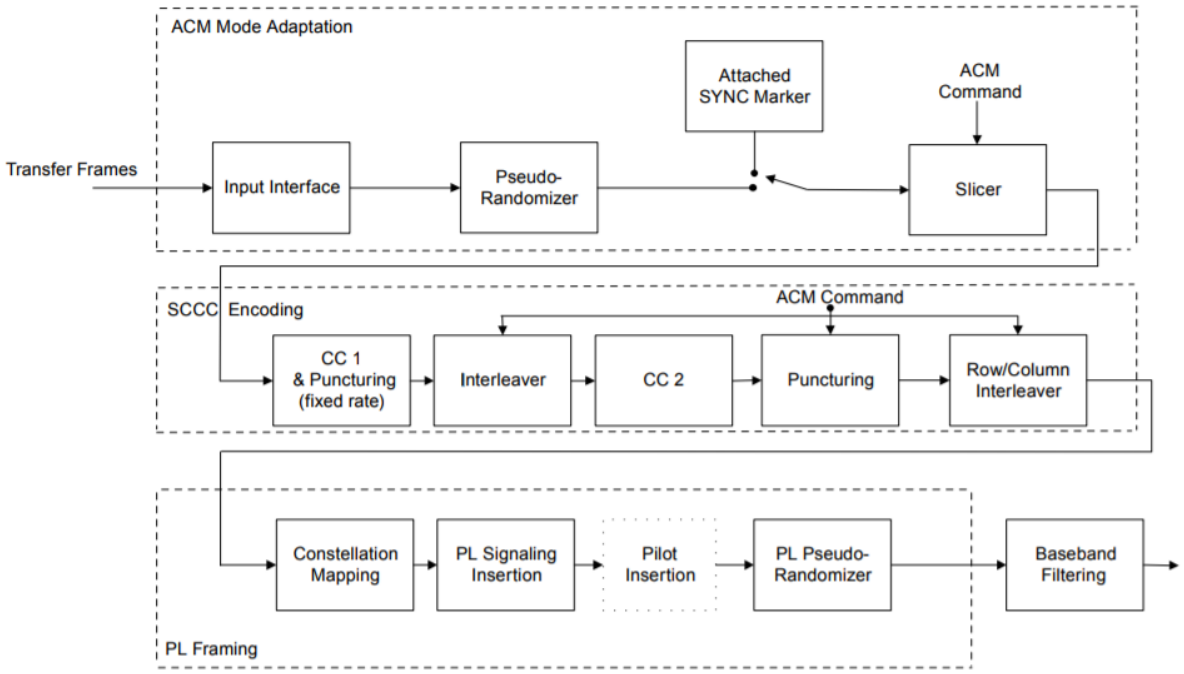

Figure 2-1: Functional diagram at sending end (figure taken from [1]).

The stream format at different stages of processing is shown in Figure 2-2: Attached SYNC Markers (ASMs) are inserted between transfer frames, generating a stream of CADUs, prior to the slicer block. Then, the stream of CADUs is sliced into *information blocks* of K bits that are fed to the SCCC encoding function that provides as output e*ncoded blocks* of N bits. Afterwards, constellation mapping is performed and its output stream is a block of e*ncoded (channel) symbols* belonging to a PSK or APSK modulation and with block length always equal to 8100 symbols. Finally, physical layer (PL) signaling and (optional) pilot insertion is done, followed by PL pseudo-randomization.

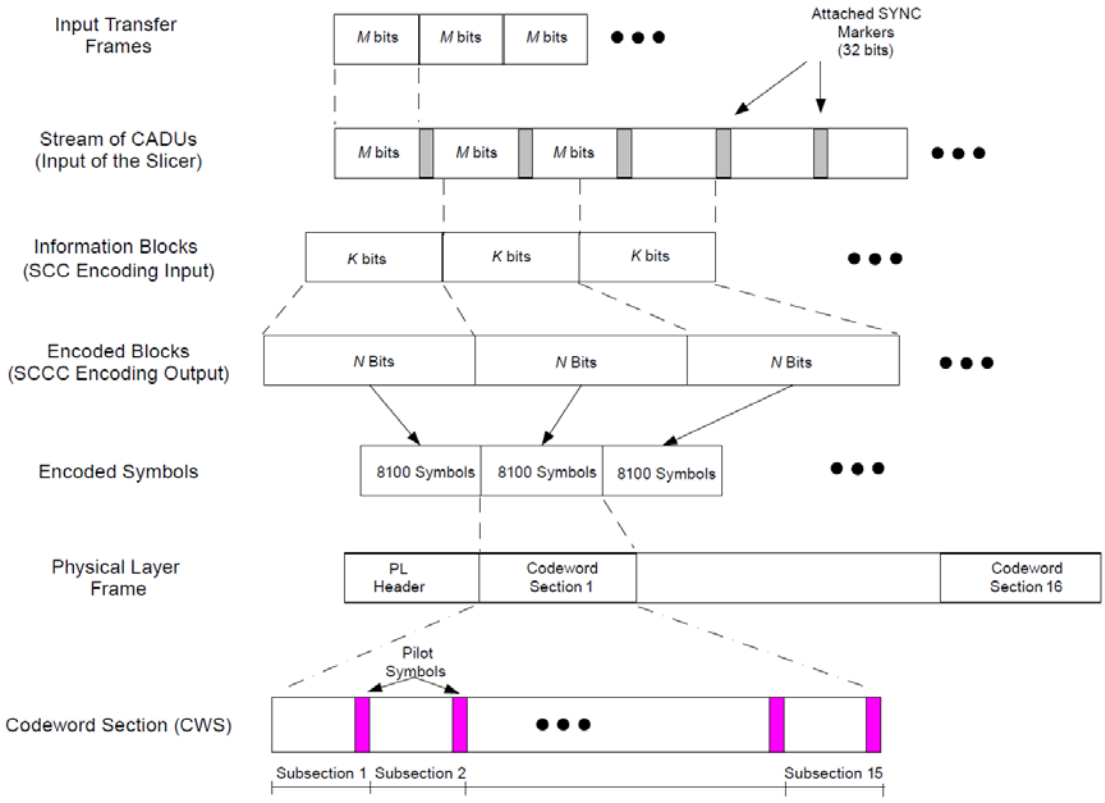

Figure 2-2: Stream format at different stages of processing (figure taken from [1]).

The configuration of all functional blocks is performed by means of a list of *managed parameters*, for which full list and description can be found in Section 9 of [1]. Among these, the *ACM format* can be seen as the main parameter, and it is identified with an integer number ranging from 1 to 27. By changing the ACM format parameter, the modulation and coding format changes, and thus the spectral efficiency can be selected as required. The ACM format is the only parameter that supports reconfiguration during operation, meaning that it can be changed without interruption or significant delay in data transmission.

Table 2-1[2] shows how the ACM format selection varies some of the main figures of the modulation and encoding scheme. In particular, it varies the constellation cardinality m (number of encoded bits per channel symbol), the length of the information block K, the length of the encoded block N, the *coding rate* defined as K/N (i.e., information bits per encoded bit), and the *efficiency* defined as Km/N (i.e., information bit per channel symbol). It can be seen that the ACM allows one to select five different constellations mapping ranging from 2 to 6 bits per channel symbol. It also allows one to select several coding rates for each constellation, hence the efficiency can change from a minimum of 0.71 bit/channel symbol, to a maximum of 5.39 bit/channel symbol.

[2] As for Figure 2-1 and 2-2, Table 2-1 is copied from [1].

Table 2-1: Modulation cardinality, information block length, encoded block length, coding rate, and efficiency as function of the ACM format.

	ACM	m	K	N	K/N	Efficiency
QPSK	1	2	5758	16200	0.36	0.71
	2		6958		0.43	0.86
	3		8398		0.52	1.04
	4		9838		0.61	1.21
	5		11278		0.70	1.39
	6		13198		0.81	1.63
8PSK	7	3	11278	24300	0.46	1.39
	8		13198		0.54	1.63
	9		14878		0.61	1.84
	10		17038		0.70	2.10
	11		19198		0.79	2.37
	12		21358		0.88	2.64
16APSK	13	4	19198	32400	0.59	2.37
	14		21358		0.66	2.64
	15		23518		0.73	2.90
	16		25918		0.80	3.20
	17		28318		0.87	3.50
32APSK	18	5	25918	40500	0.64	3.20
	19		28318		0.70	3.50
	20		30958		0.76	3.82
	21		33358		0.82	4.12
	22		35998		0.89	4.44
64APSK	23	6	33358	48600	0.69	4.12
	24		35998		0.74	4.44
	25		38638		0.80	4.77
	26		41038		0.84	5.06
	27		43678		0.90	5.39

For the functional blocks in Figure 2-1(i.e. SCCC encoding, constellation, bit mapping , pseudo-randomization and baseband filter), the reader should refer to [1], where the normative description for each elements is provided. The rest of this section provides additional explanatory details on the PL signaling (as specified in [1]).

2.1.1 PL SIGNALLING, PILOT INSERTION, AND PSEUDO-RANDOMIZATION

As explained in [1] and shown in Figure 2-3, 16 *encoded blocks* of 8100 symbols, each of them representing a codeword, are collected into a PL frame structure, to which a header is prepended, with pilots groups inserted periodically (see [1] for details).

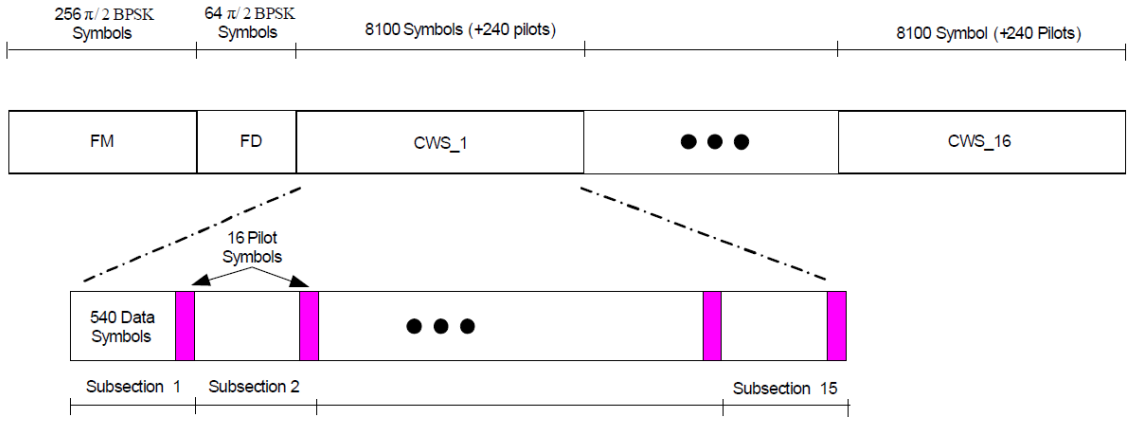

Figure 2-3: PL frame structure (figure taken from [1]).

Such header is composed by a frame marker (FM) and a descriptor (FD) , which are mapped to $\pi/2$-BPSK symbols, as shown in Figure 2-4. The $\pi/2$-BPSK transmits on the I and III quadrants bisector for odd bit positions (first, third, etc.), and on the II and IV quadrants bisector for even bit positions. Mathematically, for all bits b_i $i = 1, \ldots, 320$, of the FM and FD the I and Q component of the transmitted channel symbol shall be

$$I_i = Q_i = \frac{1}{\sqrt{2}}(1 - 2b_i), \qquad \text{if } i = 1,3,5, \ldots$$

$$I_i = -Q_i = -\frac{1}{\sqrt{2}}(1 - 2b_i), \qquad \text{if } i = 2,4,6, \ldots$$

that are exactly the same mathematical expression of (5-2) in the Recommended Standard [1].

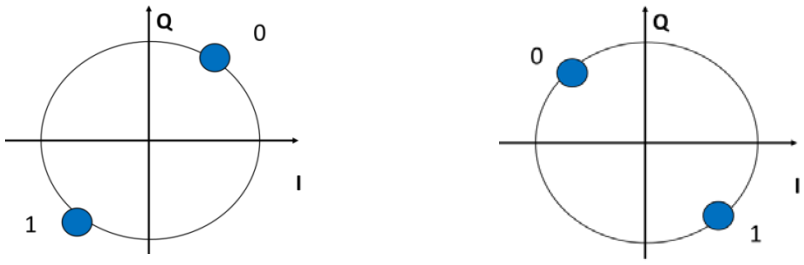

Figure 2-4: $\pi/2$-BPSK constellation at odd bit position (left) and even bit position (right).

In case pilots are used (signaled by the proper field in the FD, as described in [1]), they are un-modulated QPSK symbol, with I and Q components

$$I_i = Q_i = \frac{1}{\sqrt{2}} \ .$$

The overhead of PL signaling is less than 1%, and increases up to ~3% when pilot insertion is performed.

The resulting frame is finally randomized by means of the PL pseudo-randomization process described in Annex C of [1]. The randomization process is done by means of a complex multiplication of the channel symbol with a randomization sequence that is uniquely identified by a *code number* denoted in [1] as n.

3 PERFORMANCE OF THE RECOMMENDED CODES AND MODULATIONS ON THE AWGN CHANNEL WITH IDEAL SYNCHRONIZATION

This section reports the performance of the recommended codes and modulations over the linear channel affected by *additive white Gaussian noise* (AWGN). In particular, Section 3.1 describes the channel model adopted, while Section 3.2 shows the numerical results derived by means of computer simulations.

3.1 CHANNEL MODEL

The baseband model of the transmitted signal by the sending end is

$$x(t) = \sum_k x_k p(t - kT) \ , \tag{3-1}$$

where x_k are the transmitted channel symbols at the output of the PL framing function (described in Section 2), $p(t)$ is the shaping pulse, and T the channel symbol duration. The constellation of symbols is properly normalized such that $E\{|x_k|^2\} = E_s$, where E_s denotes the energy per symbol. The shaping pulse is SRRC, hence in ideal conditions it satisfies the intersymbol-interference free condition (the so called Nyquist condition), i.e.,

$$\int_{-\infty}^{\infty} p(t)p(t - kT)dt = \begin{cases} 1, & k = 0 \\ 0, & k \neq 0 \end{cases} .$$

The channel is considered affected only by AWGN, hence the baseband model of the received signal is given by

$$y(t) = \sum_k x_k p(t - kT) + w(t) \ ,$$

where $w(t)$ is white complex Gaussian noise with power spectral density N_0. A sufficient statistic for the computation of the *log-likelihood ratios* (LLR) is sampled at the output of a matched filter. The received samples after the matched filter read

$$y_k = x_k + w_k \ , \tag{3-2}$$

where w_k are independent Gaussian random variables with variance equal to N_0. For this discrete-time received signal, the *signal-to-noise ratio* (SNR) can be expressed as E_s/N_0 or E_b/N_0 where E_b is the energy per information bit. The E_b/N_0 is related to the E_s/N_0 by

$$\frac{E_b}{N_0}\left(\frac{K}{N}\right)m = \frac{E_s}{N_0}, \tag{3-3}$$

where m and K/N are the modulation order (number of bits per channel symbol) and the coding rate respectively (as defined in Section 2).

3.2 NUMERICAL RESULTS

The performance results of the Recommended Standard's modulation and coding scheme has been evaluated over the AWGN channel described in Section 3.1, by means of computer simulations and under the assumption of ideal synchronization. Clearly, with the AWGN channel model, results are independent of the channel symbol rate and roll-off.

As first results, Figure 3-1 and Figure 3-2 show the measured *bit error rate* (BER) as a function of the E_s/N_0 for all PSK/APSK constellations that are adopted by the various ACM formats in absence of SCCC turbo coding (uncoded). It can be noticed that for ACM formats using 16APSK (from 13 to 17) and 32APSK (from 18 to 22), constellations have different performance even when the cardinality is the same, because of the different radii (see Table 5-1 of [1]).

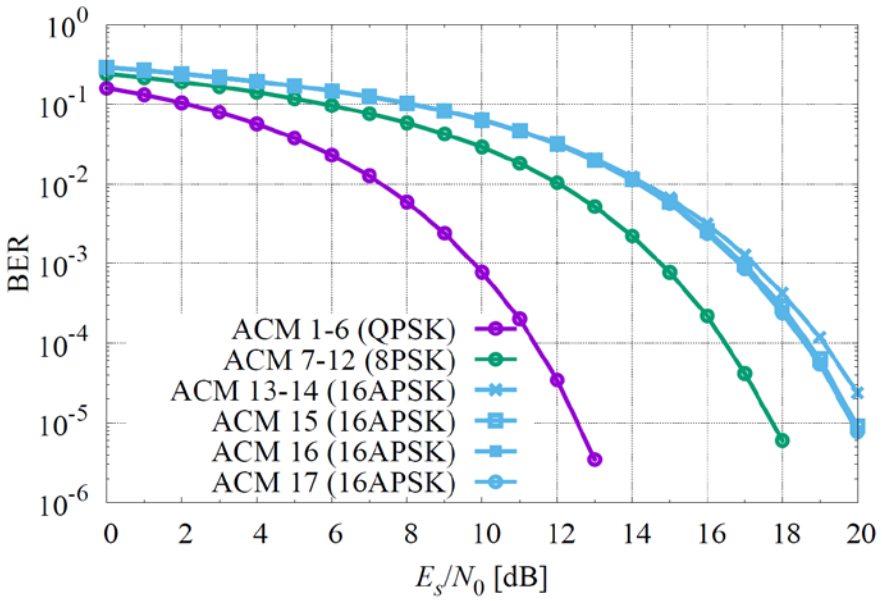

Figure 3-1: BER on linear AWGN channel for PSK/APSK constellations adopted by the ACM formats (uncoded BER).

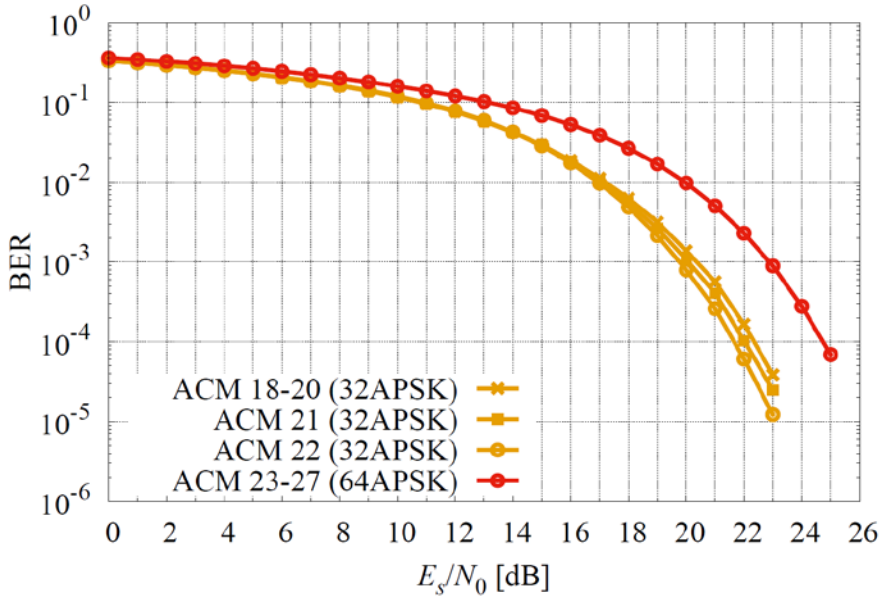

Figure 3-2: BER on linear AWGN channel for APSK constellations adopted by the ACM formats (uncoded BER).

Figures 3-3 to 3-6 show the BER and *codeword error rate* (CER) as function of the E_b/N_0 for all the 27 ACM formats, when 10 iterations of the SCCC turbo decoder are performed.

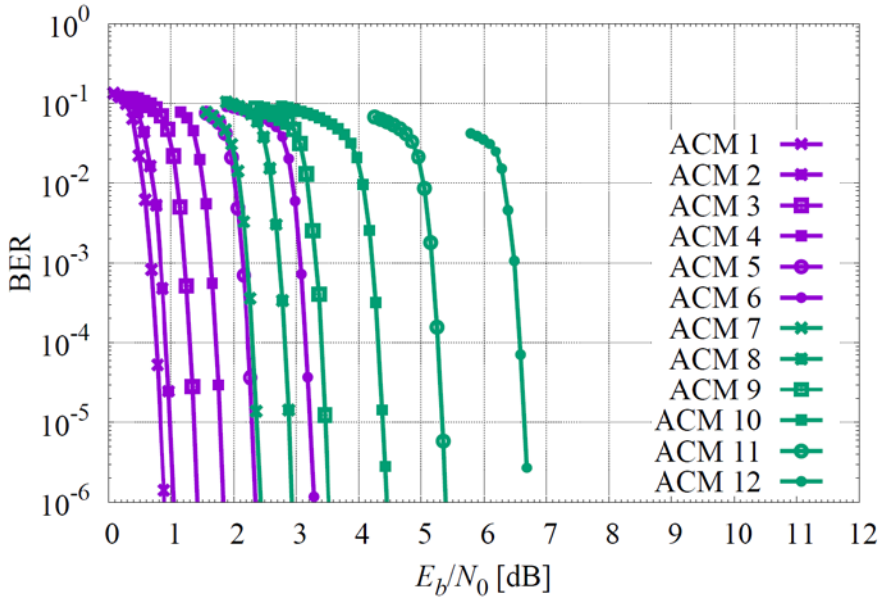

Figure 3-3: BER on linear AWGN channel for ACM formats from 1 to 12 (PSK modulations).

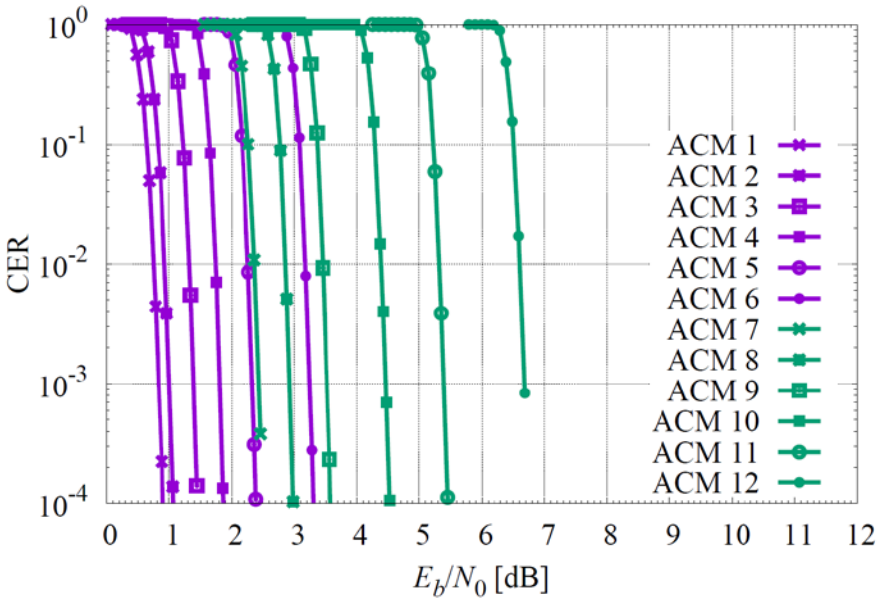

Figure 3-4: CER on linear AWGN channel for ACM formats from 1 to 12 (PSK modulations).

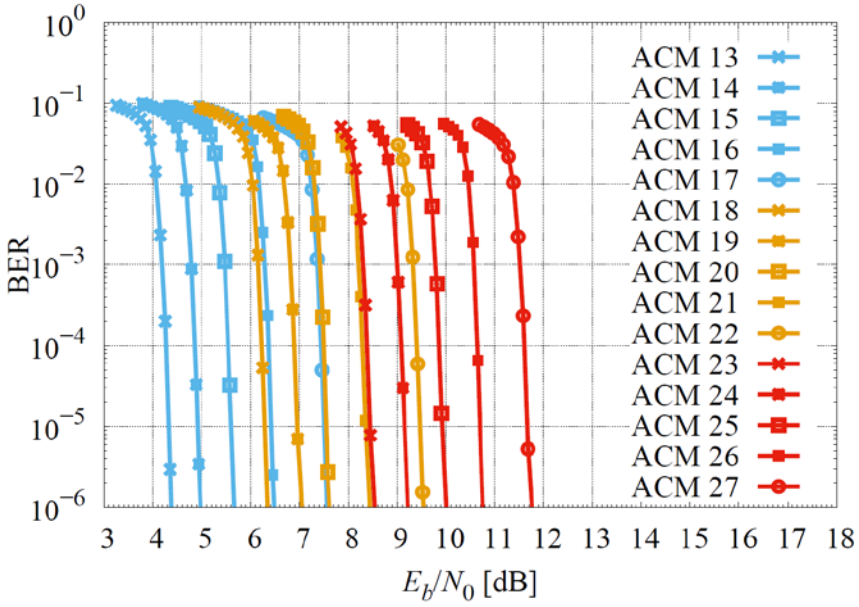

Figure 3-5: BER on linear AWGN channel for ACM formats from 13 to 27 (APSK modulations).

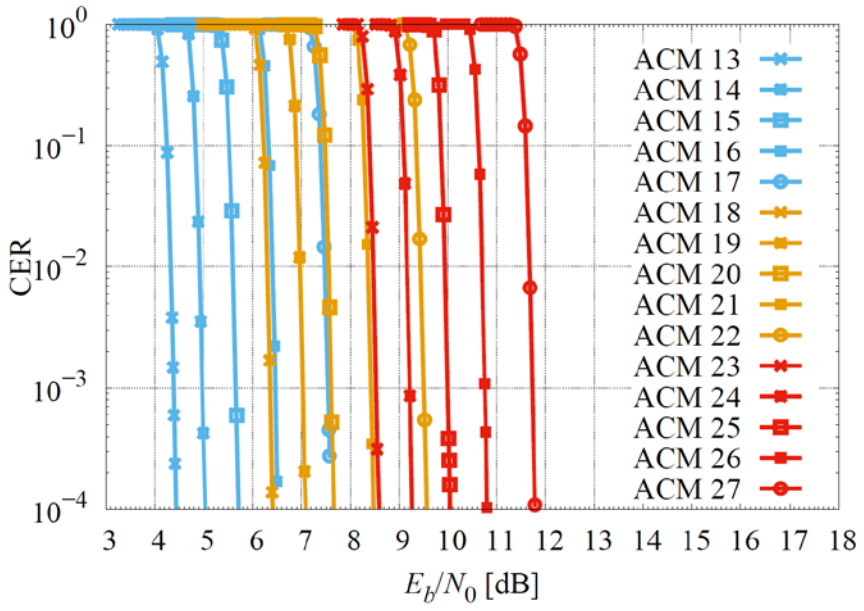

Figure 3-6: CER on linear AWGN channel for ACM formats from 13 to 27 (APSK modulations).

Table 3-1 shows the required signal-to-noise ratio (in terms of both E_s/N_0 and E_b/N_0) for achieving a target CER of 10^{-4}, and the corresponding efficiency in terms of bits per transmitted channel symbol. These values can be shown also in a plane with the efficiency versus E_b/N_0 as shown in Figure 3-7. For comparison, also the AWGN capacity (*Shannon limit*, [2]) is shown.

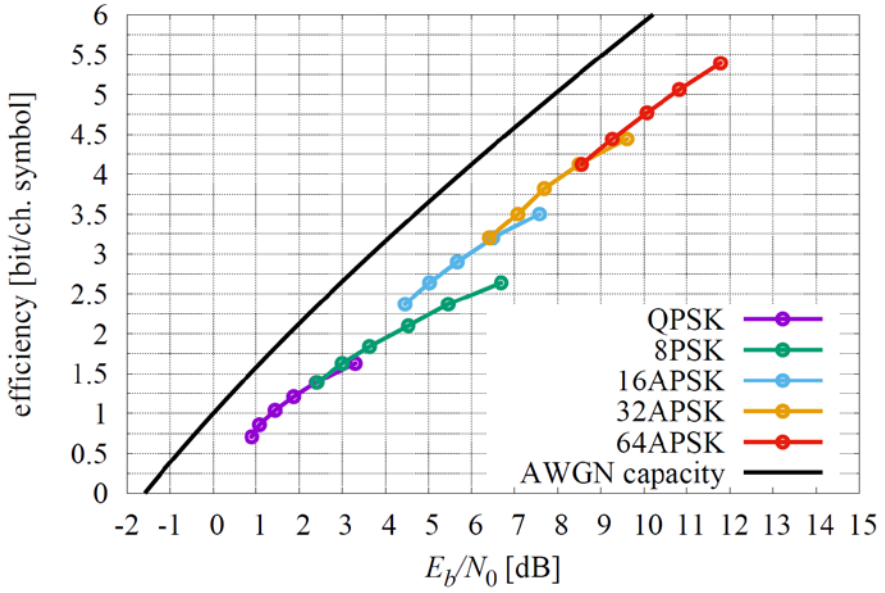

Figure 3-7: Efficiency of the recommended ACM formats on the linear AWGN channel w.r.t. channel capacity.

Table 3-1: SNR thresholds for CER=1e-4, achieved on the AWGN channel by the ACM formats.

	ACM	E_s/N_0 [dB]	E_b/N_0 [dB]	Efficiency
QPSK	1	-0.58	0.90	0.71
	2	0.42	1.08	0.86
	3	1.60	1.44	1.04
	4	2.71	1.87	1.21
	5	3.83	2.39	1.39
	6	5.42	3.30	1.63
8PSK	7	3.91	2.41	1.39
	8	5.10	3.00	1.63
	9	6.25	3.63	1.84
	10	7.75	4.53	2.10
	11	9.21	5.46	2.37
	12	10.90	6.69	2.64
16APSK	13	8.18	4.45	2.37
	14	9.24	5.03	2.64
	15	10.34	5.67	2.90
	16	11.55	6.50	3.20
	17	13.02	7.58	3.50
32APSK	18	11.46	6.41	3.20
	19	12.52	7.08	3.50
	20	13.49	7.69	3.82
	21	14.62	8.49	4.12
	22	16.04	9.61	4.44
64APSK	23	14.73	8.56	4.12
	24	15.74	9.27	4.44
	25	16.83	10.07	4.77
	26	17.85	10.83	5.06
	27	19.10	11.78	5.39

4 PERFORMANCE OF THE RECOMMENDED CODES AND MODULATIONS ON NONLINEAR CHANNELS WITH IDEAL SYNCHRONIZATION

This section focuses on the performance of the Recommended Standard's codes and modulations over a nonlinear channel model with ideal synchronization. In particular, Section 4.1 provides a channel model that includes nonlinear distortions typically due to a *traveling wave tube amplifier* (TWTA), an output filter (aimed at mitigating spectral regrowth), and AWGN. Starting from this channel model, Section 4.2 describes how to optimize the input and output back-off (IBO/OBO) by means of the total degradation (TD). Finally, Section 4.3 shows the numerical results for the recommended codes and modulations, in particular their TD, BER/FER curves, and the bandwidth expansion after the nonlinearity (due to spectral regrowth). It will be also shown how pre-distortion can improve the performance, especially for ACMs 13-17 (based on APSK modulations).

4.1 NONLINEAR CHANNEL MODEL

The linearly modulated signal of Equation (3-1) is applied to the nonlinear channel as shown in Figure 4-1, that included a TWTA and a RF output filter (mitigating spectral regrowth). The distorted signal is then further corrupted by AWGN.

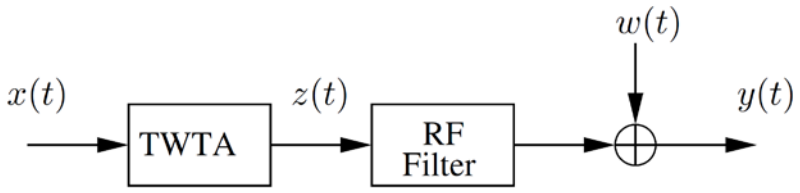

Figure 4-1: Block diagram of the overall channel model considered in simulations.

The TWTA was modelled by means of the input/output relationship

$$z(t) = f_{AM}(|x(t)|)e^{j\angle x(t)+f_{PM}(|x(t)|)} \quad ,$$

where $f_{AM}(|x(t)|)$ and $f_{PM}(|x(t)|)$ are the AM/AM and AM/PM characteristics respectively.

For all simulations a channel symbol rate of 100 MBaud and SRRC with roll-off 0.35 were assumed (unless differently specified), while at the receiver a symbol-by-symbol detector was adopted for computing the soft information (the LLRs), that are input of the decoder. A maximum of 10 decoding SCCC turbo iterations were assumed for the simulations. The specific AM/AM and AM/PM characteristics adopted for simulations (modelling a typical TWTA operating in the 25.5-27 GHz band) are as shown in Figure 4-2, while the output filter is a 5th order Elliptical filter with frequency response as shown in Figure 4-3, having ripple 0.1 dB, and passband and stopband 75 MHz and 93.75 MHz respectively.

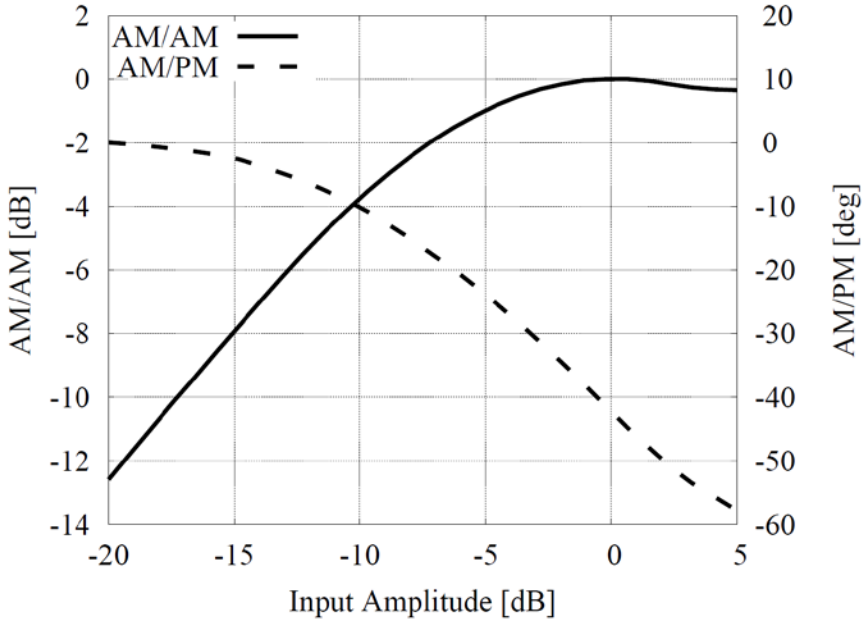

Figure 4-2: AM/AM and AM/PM nonlinear transfer characteristics adopted for simulations.

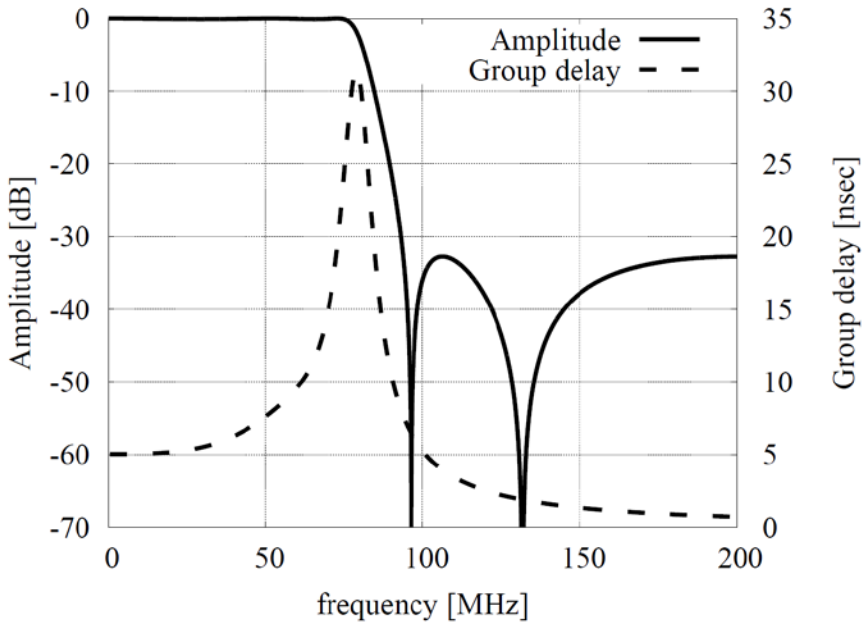

Figure 4-3: RF filter frequency response.

4.2 IBO/OBO OPTIMIZATION BY MEANS OF TOTAL DEGRADATION

A useful figure of merit for optimizing the operating point is the total degradation, defined as

$$TD = \left(\frac{E_b}{N_0} + \mathrm{OBO}\right) - \left(\frac{E_b}{N_0}\right)_{\mathrm{AWGN}} \quad [\mathrm{dB}]$$

where $\left(\frac{E_b}{N_0} + \mathrm{OBO}\right)$ is the signal-to-noise ratio and OBO values required for obtaining a specific target codeword error rate (CER) with the channel model assumed. The value $\left(\frac{E_b}{N_0}\right)_{\mathrm{AWGN}}$ represents instead the signal-to-noise ratio required on the ideal AWGN channel to achieve the same target CER (and reported in Table 3-1). With this definition, TD provides a useful representation of the overall losses experienced by the link, both in term of distortion as well as reduced available power (due to the back-off). In this report a target CER equal to 10^{-4} has been adopted for the optimization of the operating point.

The operating point optimization is achieved as explained in the following. CER curves must be computed for different IBO[3], and the total degradation is derived as loss between each of the curves with respect the AWGN curve at CER=10^{-4}. Finally, the resulting TD values shall be reported as function of the IBO. An example of this process is shown in in Figure 4-4 and Figure 4-5 for ACM format 15. In the first figure all CER curves are shown down to CER=10^{-4}, and the total degradation is measured as loss from the AWGN curve. In the second figure, the loss is reported as function of the IBO, and it can be seen that the optimal IBO is around 5 dB.

[3] While IBO is an input parameter, the OBO is measured at the output of the amplifier and cannot be directly derived, for the modulated signal, by the AM/AM curve of Figure 4-2 (that is valid for an unmodulated carrier).

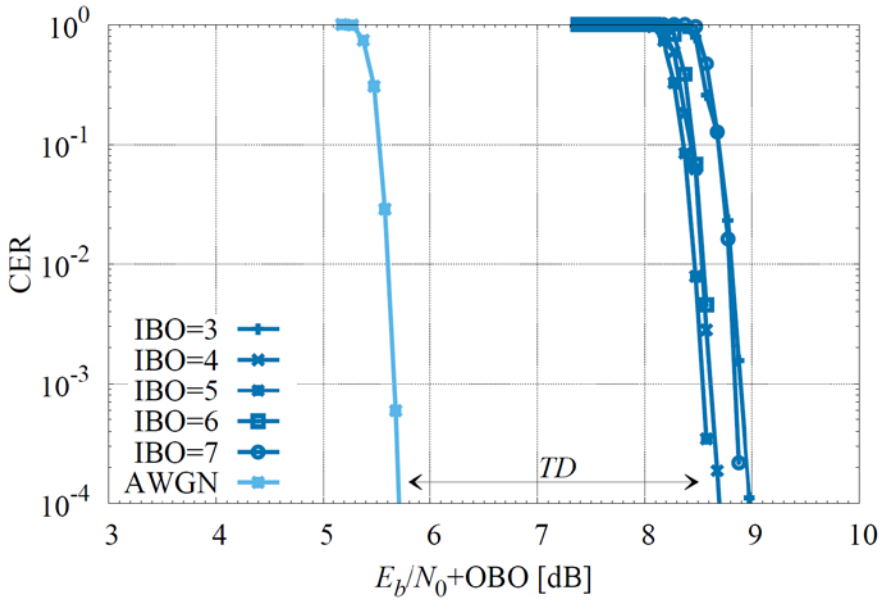

Figure 4-4: CER for different IBO for ACM 15 on nonlinear AWGN channel.

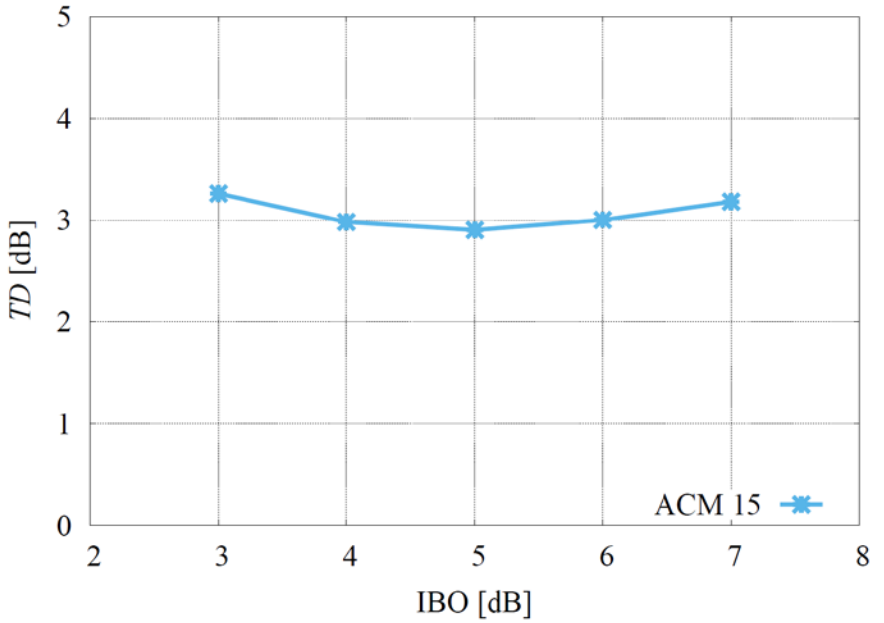

Figure 4-5: Total degradation for ACM format 15.

4.3 NUMERICAL RESULTS

4.3.1 TOTAL DEGRADATION AND ERROR RATE CURVES

Numerical simulations have been carried out with the channel model described in the previous section in order to assess the impact of the TWTA together with the RF filter.

Figure 4-6 and Figure 4-7 show the total degradation for all the ACM formats as function of the IBO. It can be noticed that the optimal IBO and the minimum total degradation tends to increase with the modulation order. In particular the optimal IBO for PSK modulations is between 0 and 1 dB and the total degradation ranges from 0.6 to 1.3 dB. Whereas the optimal IBO for APSK modulations can range from 4 to 12 dB with corresponding total degradation from 2 to 8 dB.

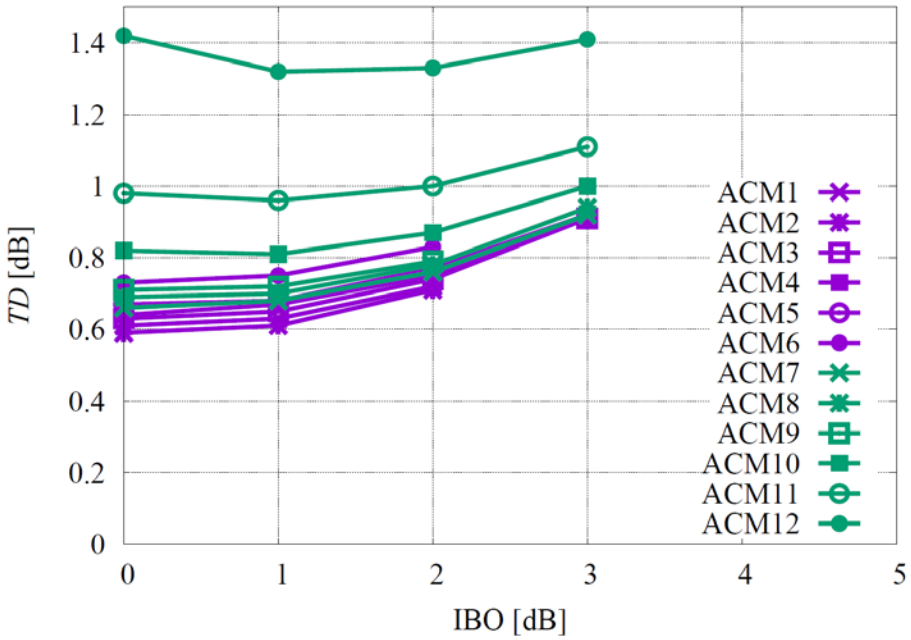

Figure 4-6: Total degradation for ACM formats from 1 to 12 (PSK modulations).

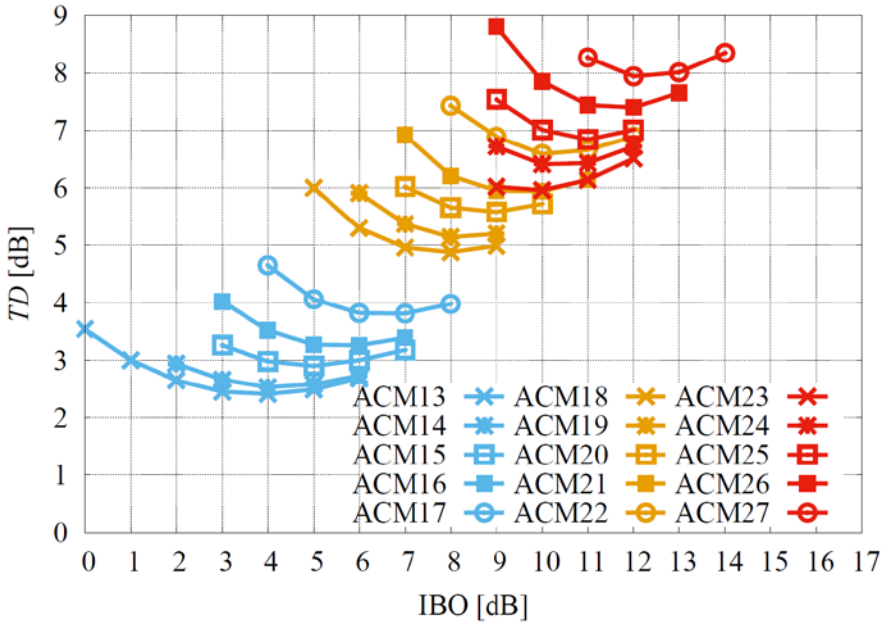

Figure 4-7: Total degradation for ACM formats from 13 to 27 (APSK modulations).

Figures 4-8 to 4-11 shows the BER and CER for all the possible ACM using the optimal IBO found by means of the total degradation analysis. The corresponding SNR thresholds for CER equal to 10^{-4} and OBO for each individual ACM mode (to be taken into account when performing system level design) can be found in Table 4-1.

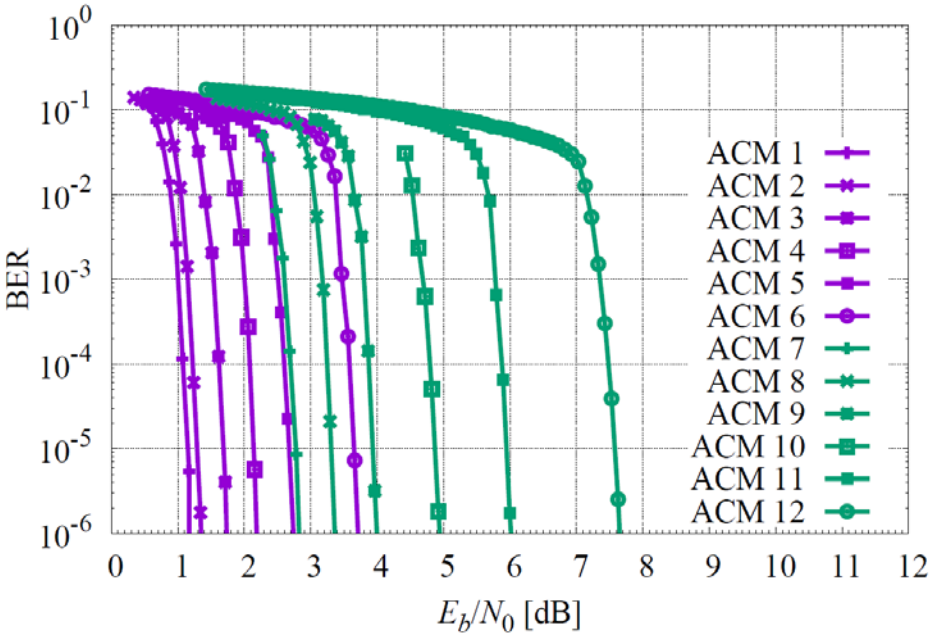

Figure 4-8: BER on nonlinear AWGN channel for ACM formats from 1 to 12 (PSK modulations) with the optimal IBO.

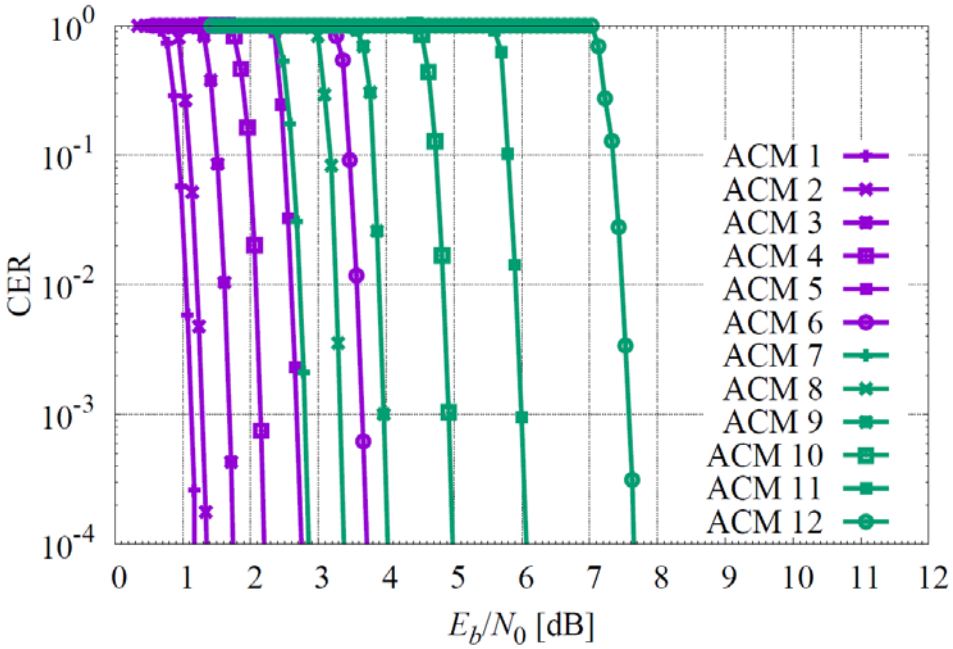

Figure 4-9: CER on nonlinear AWGN channel for ACM formats from 1 to 12 (PSK modulations) with the optimal IBO.

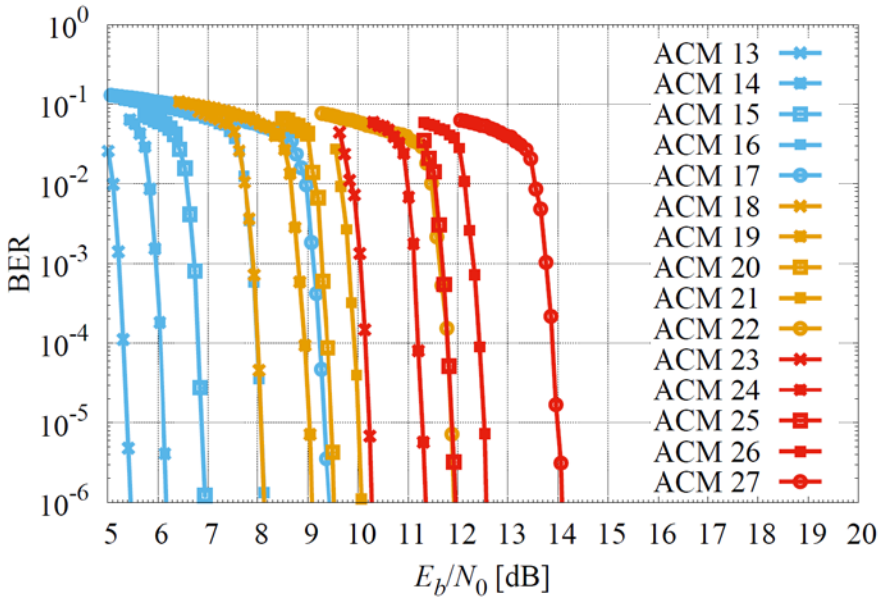

Figure 4-10: BER on nonlinear AWGN channel for ACM formats from 13 to 27 (APSK modulations) with the optimal IBO.

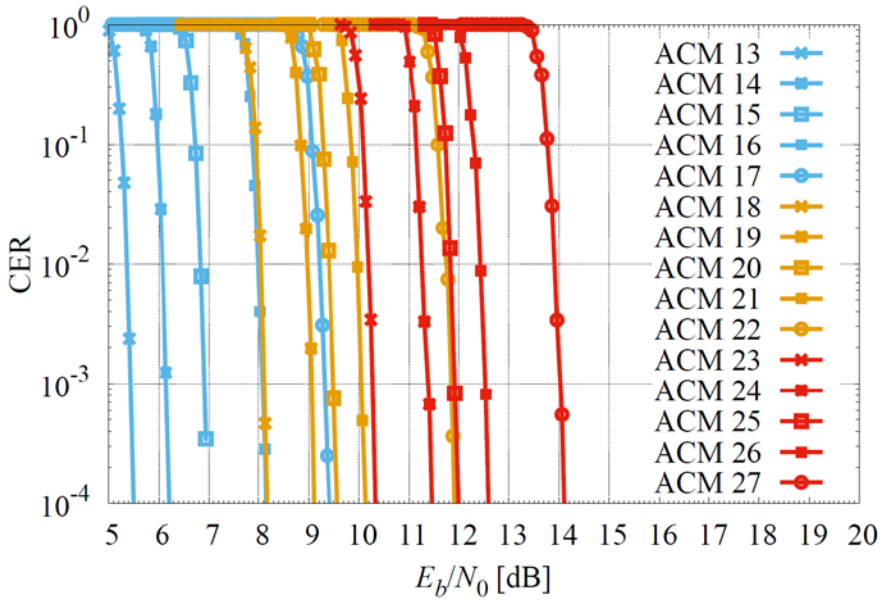

Figure 4-11: CER on nonlinear AWGN channel for ACM formats from 13 to 27 (APSK modulations) with the optimal IBO.

Table 4-1: SNR thresholds for CER=1e-4, and corresponding OBO and TD, achieved by the recommended ACM formats on the nonlinear AWGN channel without pre-distortion.

	ACM	E_s/N_0 [dB]	E_b/N_0 [dB]	OBO [dB]	TD [dB]	Efficiency
QPSK	1	-0.28	1.20	0.32	0.61	0.71
	2	0.70	1.35	0.32	0.59	0.86
	3	1.91	1.74	0.32	0.63	1.04
	4	3.03	2.20	0.32	0.64	1.21
	5	4.18	2.75	0.32	0.67	1.39
	6	5.84	3.72	0.32	0.73	1.63
8PSK	7	4.29	2.86	0.29	0.66	1.39
	8	5.50	3.38	0.29	0.69	1.63
	9	6.67	4.02	0.29	0.71	1.84
	10	8.20	4.98	0.36	0.81	2.10
	11	9.82	6.07	0.36	0.96	2.37
	12	11.87	7.65	0.36	1.32	2.64
16APSK	13	9.25	5.50	1.34	2.41	2.37
	14	10.43	6.21	1.34	2.53	2.64
	15	11.61	6.99	1.63	2.90	2.90
	16	13.19	8.14	1.63	3.27	3.20
	17	14.85	9.41	1.99	3.82	3.50
32APSK	18	13.22	8.17	3.12	4.88	3.20
	19	14.54	9.09	3.12	5.14	3.50
	20	15.39	9.57	3.68	5.58	3.82
	21	16.29	10.14	4.27	5.94	4.12
	22	18.37	11.88	4.27	6.59	4.44
64APSK	23	16.48	10.33	4.21	5.96	4.12
	24	17.94	11.47	4.21	6.41	4.44
	25	18.78	12.00	4.89	6.84	4.77
	26	19.63	12.59	5.62	7.40	5.06
	27	21.42	14.10	5.62	7.94	5.39

4.3.2 STATIC PRE-DISTORTION

The total degradation can be effectively decreased by means of pre-distortion. A static data pre-distorter (at the transmitter), as the one in [7], was assumed for the simulations presented in this section. Such pre-distortion is basically a simple look-up table that transmits the constellation symbols with a fixed correction of the radii amplitudes and phases (computed off-line).

Figures 4-12 to 4-14 show the total degradation as function of IBO for ACM formats using 16APSK, 32APSK and 64APSK. For comparison, also the total degradation without pre-distortion (as in Section 4.3.1) is shown. It can be seen how, already with this simple pre-distorter, a performance gain of more than 0.5 dB is possible with 16APSK and more than 2 dB with 32APSK and 64-APSK.

On the other hand, in case of PSK modulations there are no performance gains since the constellation has a constant amplitude. Figure 4-15 shows the total degradation for some ACM formats having 8PSK modulation and it can be seen that the static pre-distorter does not provide any improvement.

It is pointed out that the pre-distortion algorithm adopted here is just a reference and it shall not be considered as optimal. For instance it is expected that pre-distortion based on more complex model, e.g., a polynomial representation of the amplifier (see [8]), can provide a performance gain of up to 5 dB for 64-APSK, in addition to reducing the spectral occupation.

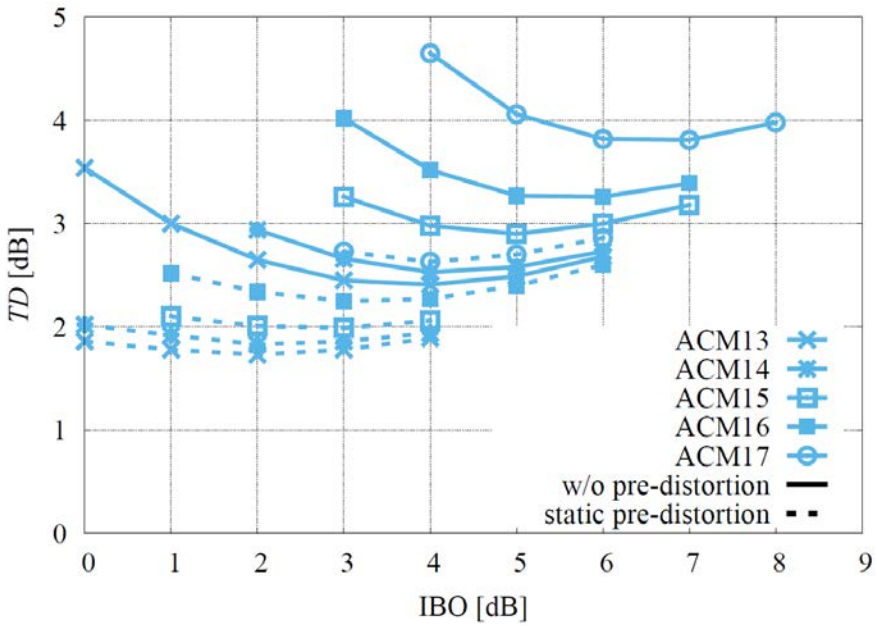

Figure 4-12: Total degradation for ACM formats from 13 to 17 (16APSK) with and without pre-distortion.

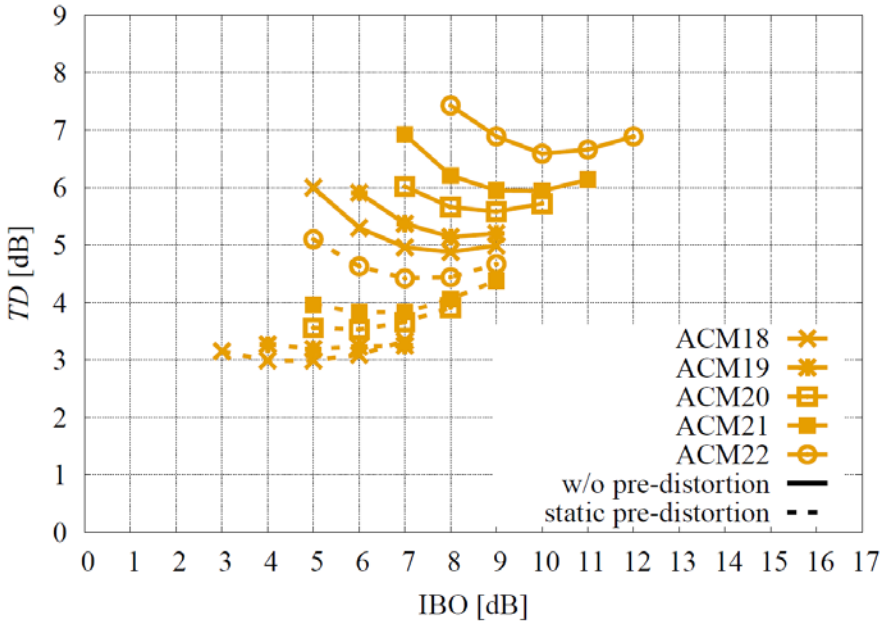

Figure 4-13: Total degradation for AMC formats from 18 to 22 (32APSK) with and without pre-distortion.

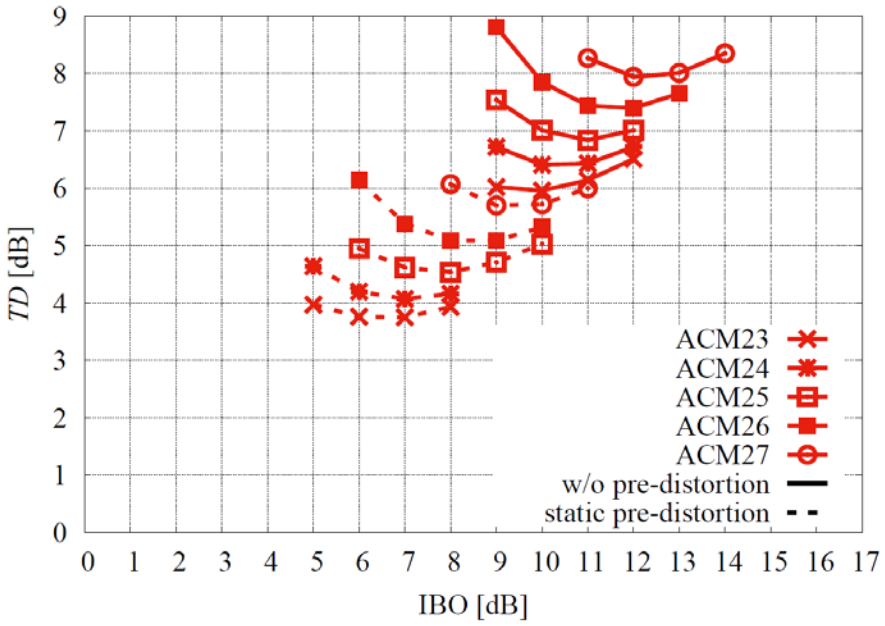

Figure 4-14: Total degradation for ACM formats from 23 to 27 (64APSK) with and without pre-distortion.

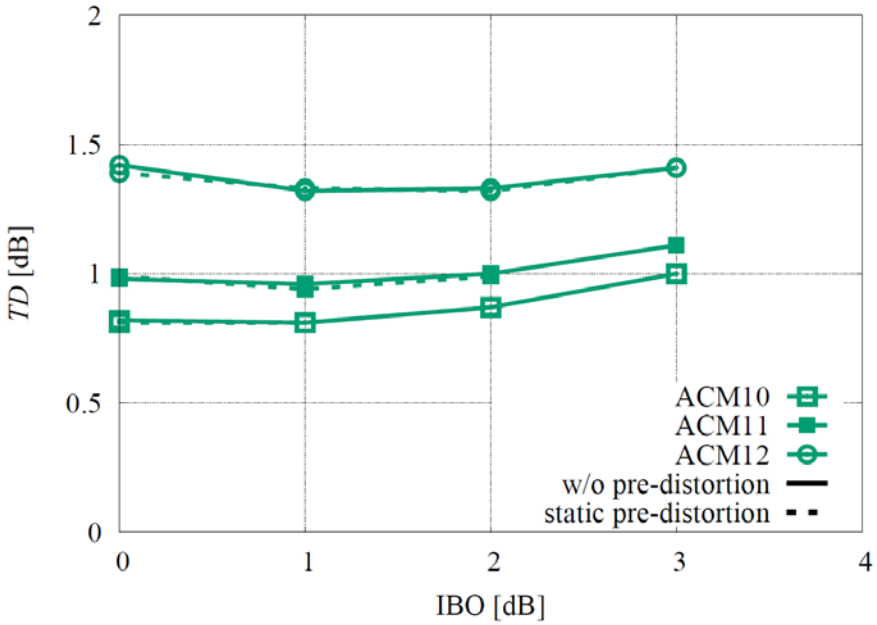

Figure 4-15: Total degradation for ACM formats from 10 to 12 (8PSK) with and without pre-distortion.

The SNR values for APSK modulations that allows a CER equal to 10^{-4} when static pre-distortion is adopted are summarized in Table 4-2. In the table is reported also the corresponding OBO, total degradation TD, and its gain w.r.t. the scenario without pre-distortion (see Table 4-1). The total degradation gain can be seen also in a SNR plane as the one in Figure 4-16, where the $E_b/N_0 + OBO$ is shown for each E_b/N_0 threshold for the AWGN channel and the distance from the bisector is the total degradation.

Table 4-2: SNR thresholds for CER=1e-4, and corresponding OBO and TD, achieved by the recommended ACM formats with pre-distortion.

	ACM	E_s/N_0 [dB]	E_b/N_0 [dB]	OBO [dB]	TD [dB]	TD Gain [dB]
16APSK	13	8.91	5.16	1.00	1.73	0.68
	14	10.07	5.86	1.00	1.83	0.70
	15	11.18	6.55	1.14	1.99	0.91
	16	12.26	7.61	1.15	2.25	1.02
	17	14.30	8.86	1.35	2.63	1.19
32APSK	18	12.42	7.37	2.03	2.99	1.89
	19	13.68	8.24	2.03	3.19	1.95
	20	14.68	8.86	2.34	3.53	2.05
	21	16.10	9.95	2.35	3.83	2.11
	22	17.79	11.31	2.67	4.42	2.17
64APSK	23	16.29	10.13	2.20	3.76	2.20
	24	17.19	10.71	2.62	4.07	2.34
	25	18.27	11.48	3.10	4.54	2.30
	26	19.29	12.25	3.65	5.09	2.31
	27	21.15	13.83	3.65	5.70	2.24

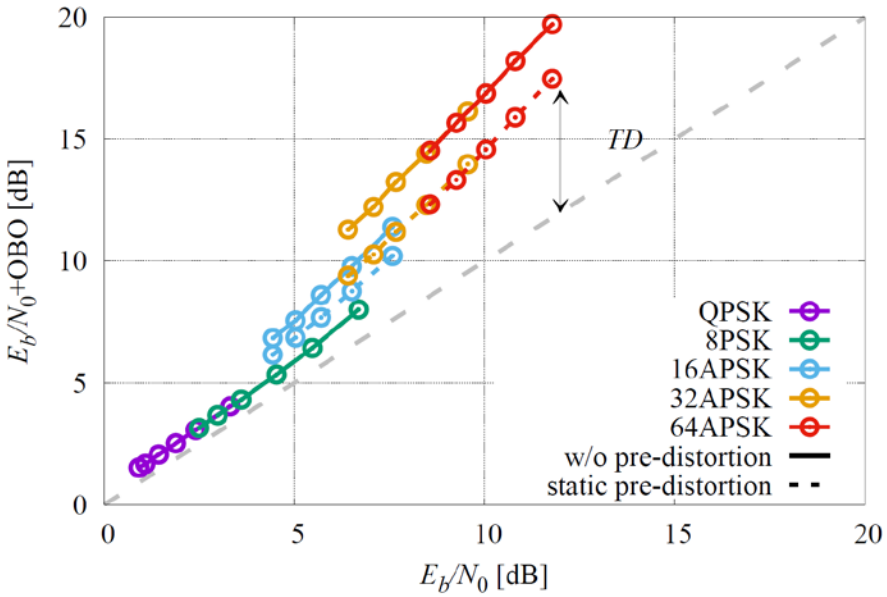

Figure 4-16: SNR threshold plane for all the ACM formats.

4.3.3 OCCUPIED BANDWIDTH

The bandwidth W, defined as the bandwidth containing 99% of the signal power, has been computed after the nonlinearity for roll-off 0.2 and 0.35. Figure 4-17 and Figure 4-18 show W before a post-amplifier RF Filter and normalized to the channel symbol rate R_{chs} as function of OBO. Since 16APSK and 32APSK have circumference radii that depends on the actual ModCod, it is shown only ACM13 and ACM18 that have the highest peak-to-average ratio of their set. It can be seen that for OBO greater than 4 dB a bandwidth equal to the one in linear regime is reached, i.e., all the modulations have bandwidth $1.07R_{chs}$ and $1.17R_{chs}$ for roll-off 0.2 and 0.35 respectively. Additionally, it can be seen that 32APSK has the largest bandwidth occupancy. This is due to its peak-to-average ratio that can be demonstrated to be higher than those for 16APSK and 64APSK.

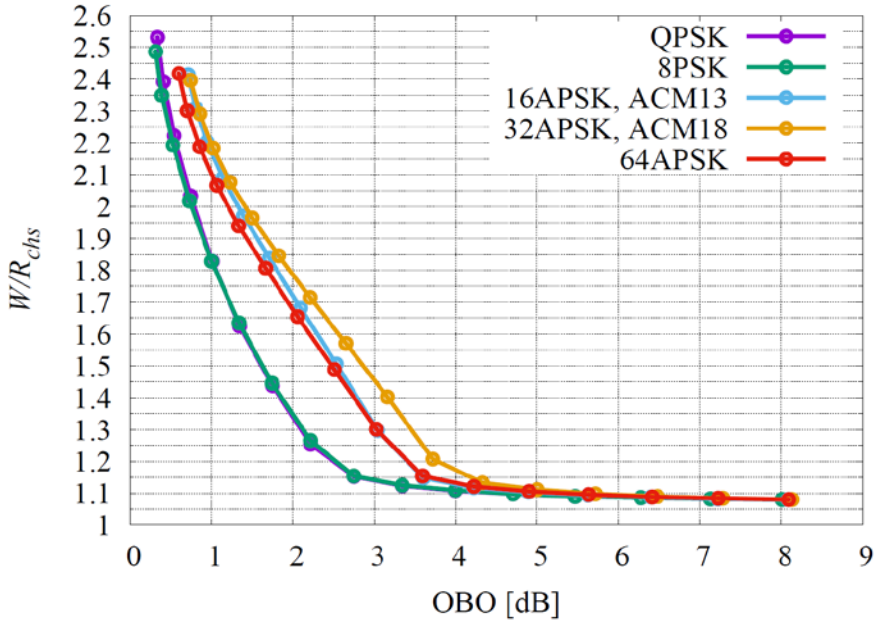

Figure 4-17: Bandwidth normalized to the channel symbol rate as a function of the OBO (SRRC with roll-off 0.20).

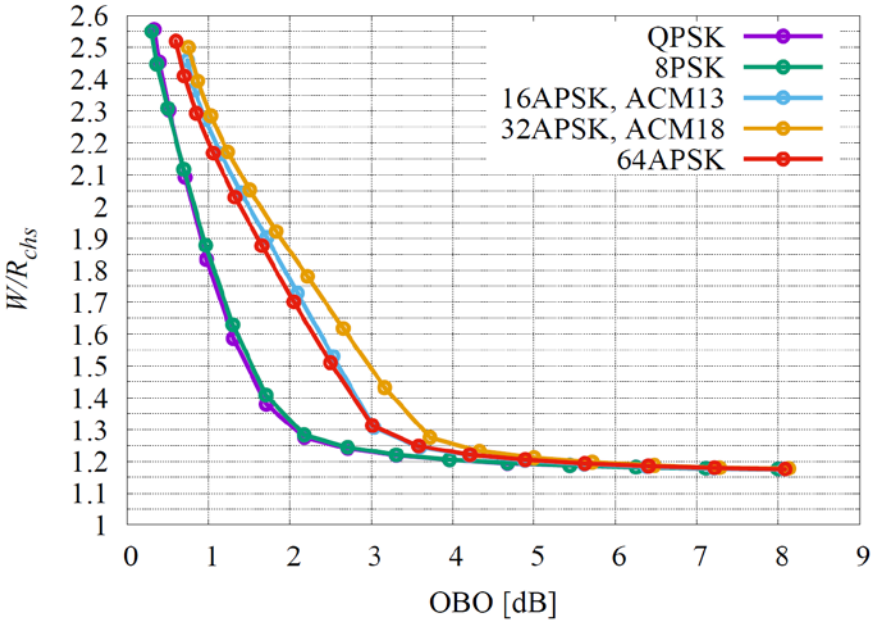

Figure 4-18: Bandwidth normalized to the channel symbol rate as a function of the OBO (SRRC with roll-off 0.35).

The RF filter aims to minimize the spectral regrowth outside the signal bandwidth. Figure 4-19 and Figure 4-20 show the bandwidth for all the modulations after the filter. It can be seen that in all cases the bandwidth is always less than $1.4R_{chs}$.

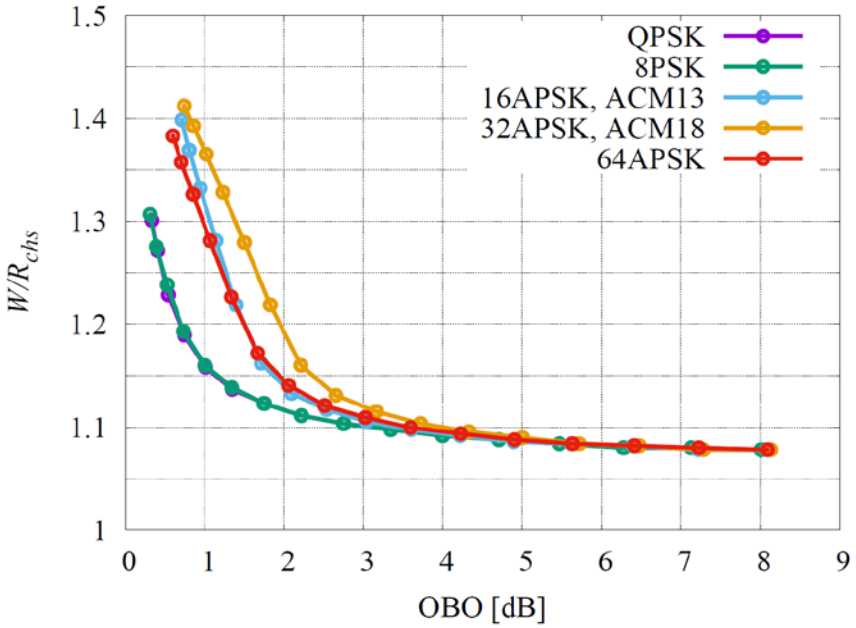

Figure 4-19: Bandwidth after the RF filter normalized to the channel symbol rate as a function of the OBO (SRRC with roll-off 0.20).

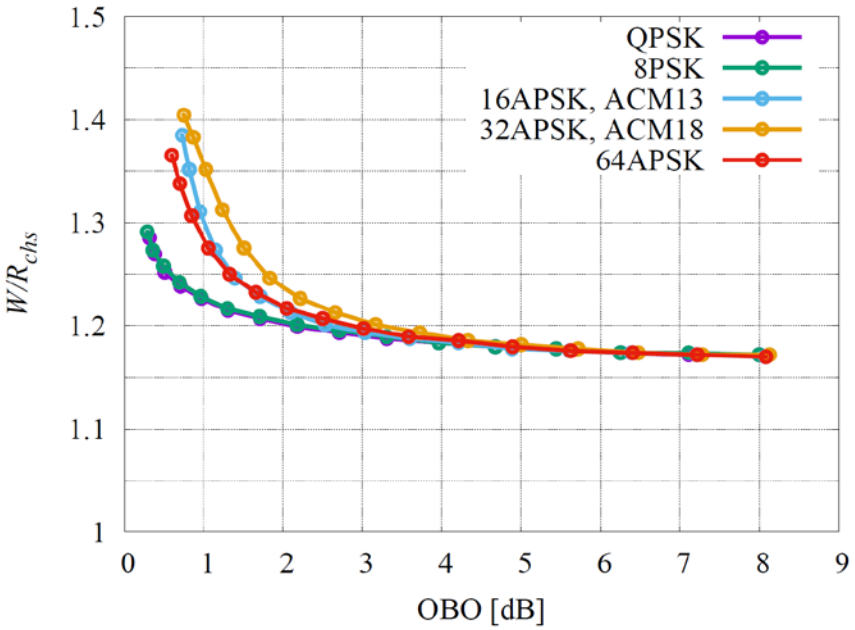

Figure 4-20: Bandwidth after the RF filter normalized to the channel symbol rate as a function of the OBO (SRRC with roll-off 0.35).

Table 4-3 shows a summary of the expected bandwidth for some of the ACM formats considered in previous sections when the shaping pulse has roll-off 0.35 and the IBO is selected as the one that minimize the total degradation. For comparison, Table 4-4 shows the bandwidth occupancy with pre-distortion at the transmitter (adopted only for APSK modulations). It can be seen that if RF filtering is adopted, pre-distortion allows to decrease noticeably the IBO/OBO, while the bandwidth increase due to spectral re-growth is maintained acceptable.

Table 4-3: Bandwidth for different ACM at the optimal IBO when no pre-distortion is adopted at the transmitter (SRRC with roll-off 0.35).

ACM	Optimal IBO [dB]	Corresponding OBO [dB]	Bandwidth at optimal IBO before RF filtering	Bandwidth at optimal IBO after RF filtering
4	0	0.32	2.56· R_{chs}	1.29· R_{chs}
10	1	0.36	2.44 · R_{chs}	1.27 · R_{chs}
14	4	1.34	2.04· R_{chs}	1.24· R_{chs}
20	9	3.68	1.27· R_{chs}	1.19· R_{chs}
25	11	4.89	1.21· R_{chs}	1.18· R_{chs}

Table 4-4: Bandwidth for different ACM at the optimal IBO when pre-distortion is adopted at the transmitter (SRRC with roll-off 0.35).

ACM	Optimal IBO [dB]	Corresponding OBO [dB]	Bandwidth at optimal IBO before RF filtering	Bandwidth at optimal IBO after RF filtering
14	2	1.00	$2.27 \cdot R_{chs}$	$1.31 \cdot R_{chs}$
20	6	2.34	$1.78 \cdot R_{chs}$	$1.22 \cdot R_{chs}$
25	8	3.10	$1.31 \cdot R_{chs}$	$1.20 \cdot R_{chs}$

5 SYNCHRONIZATION

This section deals with the synchronization for the recommended codes and modulations. In particular, a possible synchronization chain is described and performance evaluated on the AWGN channel when affected by phase noise and Doppler shift. The remainder of this section is organized as follows: Section 5.1 describes the adopted channel model with focus on the mathematical models adopted for generating Doppler and phase noise. Section 5.2 introduces the synchronization chain that has been adopted for evaluation of the performance. Sections 5.3 to 5.6 analyze the performance and characteristics of each algorithm adopted in the synchronization chain. Finally, in Section 5.7 performance results in terms of CER are presented.

5.1 CHANNEL MODEL AFFECTED BY DOPPLER AND PHASE NOISE

The linearly modulated signal of Equation (3-1) is transmitted over an AWGN channel affected by Doppler shift, Doppler rate, and phase noise. Hence, the baseband model of the received is given by

$$y(t) = \sum_k x_k p(t - kT) e^{j\phi(t)} + w(t) \ , \tag{5-1}$$

where x_k are the transmitted channel symbols belonging to a constellation (PSK/APSK) properly normalized such that $E\{|x_k|^2\} = E_s$ (being E_s the energy per symbol) and $w(t)$ is AWGN with power spectral density N_0. The SNR is equal to E_s/N_0. Instead, $\phi(t)$ reads

$$\phi(t) = 2\pi \int_0^t f(\tau) d\tau + \theta(t) \ ,$$

with $f(t)$ and $\theta(t)$ the Doppler profile and the phase noise respectively. Once again, all simulations assumed a channel symbol rate of $R_{chs} = 100$ MBaud and SRRC with roll-off 0.35, while for comparison purposes with AWGN results the E_b/N_0 does not take into account the overhead due to frame header and pilots (for which another ~0.15 dB should be taken into account due to the 3% overhead of PL signaling and pilot insertion, see Section 2.1.1).

For $f(t)$ two possible profiles were adopted for testing different Doppler shift and rate conditions. Namely, a s*inusoidal profile* having expression and derivative as

$$f(t) = f_{\mathrm{D}} \cos\left(\frac{f_{\mathrm{R}}}{f_{\mathrm{D}}} t\right), \qquad \frac{df(t)}{dt} = -f_{\mathrm{R}} \sin\left(\frac{f_{\mathrm{R}}}{f_{\mathrm{D}}} t\right) \ , \tag{5-2}$$

where f_D is the maximum Doppler shift and f_R is the maximum Doppler rate, and a *triangular wave*, having maximum Doppler shift f_D and derivative $\pm f_R$. For both the profiles, unless differently specified, f_D =1 MHz and a f_R =50 kHz/s were considered.

Notice that the sinusoidal profile tries to reproduce the satellite passes. Figure 5-1 show the Doppler profile sampled at begin of each frame when f_D =1 MHz and a f_R =50 kHz/s, while, Figure 5-2 shows the Doppler profile of a satellite at 700 km from Earth, transmitting at 27 GHz, and passing at zenith. It can be noticed that the sinusoidal profile is adequate for reproducing the Doppler shift and rate experienced in real passes and that the adopted value f_D and f_R are well above the ones that can be experienced in K-Band. In fact, the example of Figure 5-2 shows a Doppler shift of 600 kHz and a maximum Doppler rate of 7 kHz/s.

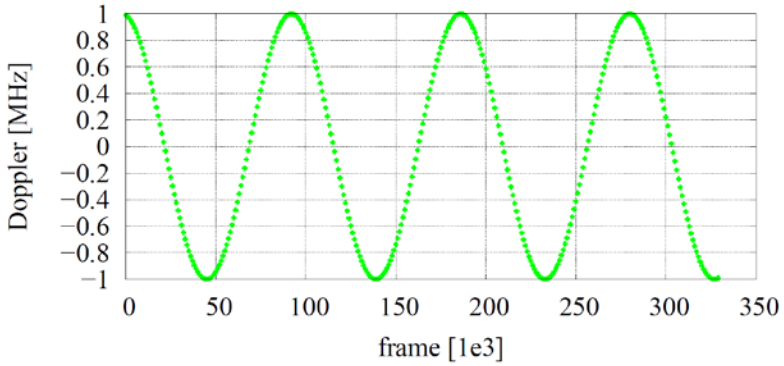

Figure 5-1: Sinusoidal profile for Doppler shift and rate at 1 MHz and 50 kHz/s.

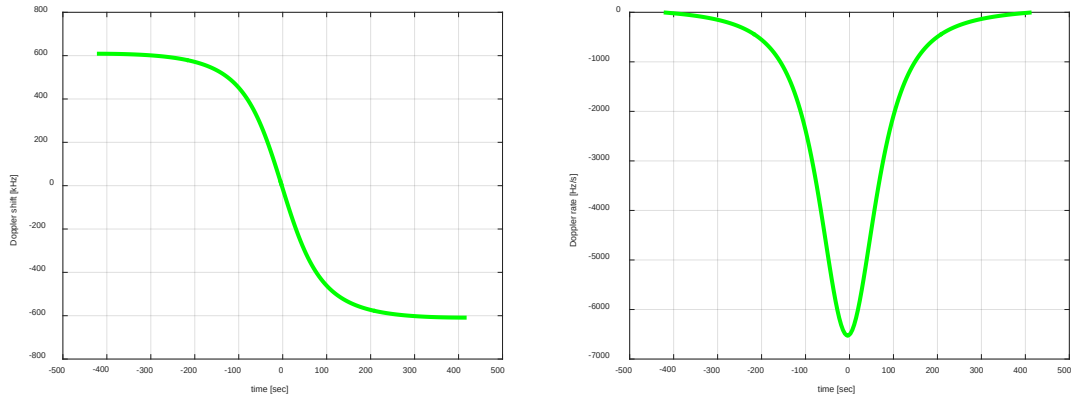

Figure 5-2: Doppler rate and shift for an Earth Observation satellite at 700 km, passing at zenith, and transmitting at 27 GHz.

Similarly, the triangular wave tries to model the carrier sweep, and it has been included as worst case of this Report's simulations. An example is reported in Figure 5-3 that shows the triangular wave sampled at begin of each frame when f_D =1 MHz and a f_R =50 kHz/s.

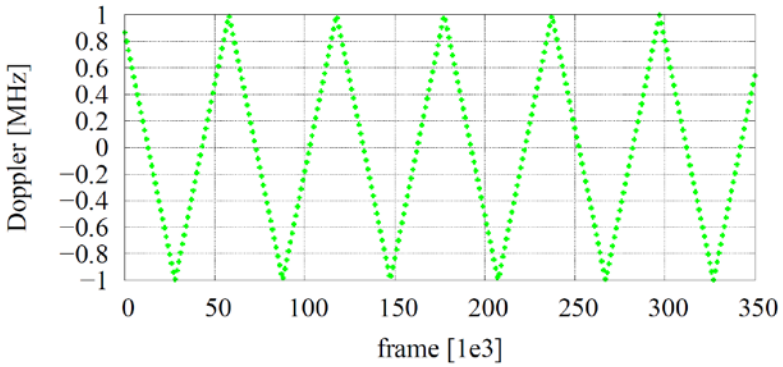

Figure 5-3: Triangular wave frequency profile for Doppler shift and rate at 1 MHz and 50 kHz/s.

Differently, the phase noise $\theta(t)$ is a coloured Gaussian random process. Its power spectral density is defined by the Fourier transform of $E\{\theta(t+\tau)\theta(t)\}$, which is usually known as *phase noise mask*. For phase noise, all simulations were carried out by using a phase noise mask as shown in Figure 5-4, as recommended in [11] for channel symbol rates above 1 MBaud. In particular, this phase noise mask has standard deviation $\sigma = 1.45$ degrees in the bandwidth $[10^2, R_{chs}/2]$ Hz (being $R_{chs} = 100$ MBaud the channel symbol rate) and it is slightly worse than phase noise measured in actual hardware (26 GHz modulator).

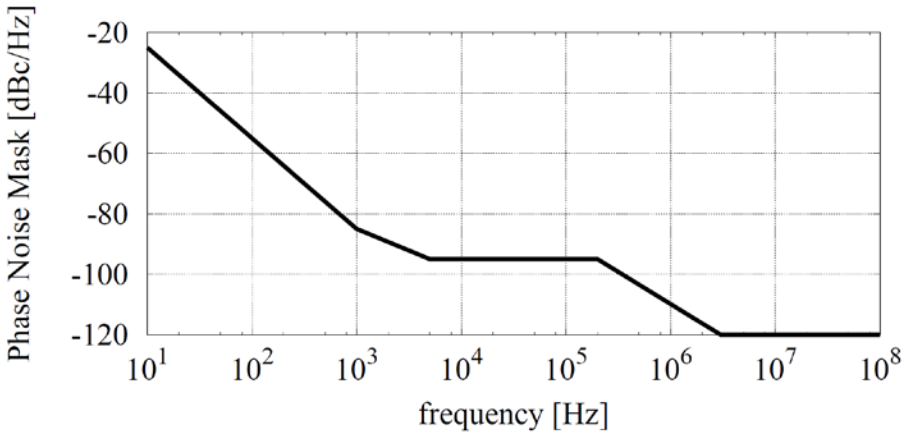

Figure 5-4: Phase noise mask adopted for simulation of the phase noise experienced in K-Band.

5.2 STUDIED SYNCHRONIZATION SCHEME

If the received signal in (5-1) pass through a filter matched to the shaping pulse, the sequence of samples $\{y_k\}$ at its output reads

$$y_k = \sum_i x_{k-i} g_{i,k-i} + w_k \quad ,$$

where

$$g_{i,k-i} = \int_{-\infty}^{\infty} e^{j\phi(t+(k-i)T)} p(t)p(t-iT)\mathrm{d}t \quad ,$$

and w_k are independent Gaussian random variables with variance equal to N_0. Under the assumption that $\phi(t)$ is 'slow' with respect the channel symbol time, the expression above simplifies to

$$y_k \cong x_k e^{j\phi_k} + w_k \quad ,$$

where $\phi_k = \phi(kT)$. Hence, frequency and phase synchronization and SNR estimation can be performed at channel symbol time.

In light of this assumption, the synchronization scheme that has been analyzed in next sections is the one shown in Figure 5-5, where:

- Frequency synchronization is carried out with a frequency locked loop (FLL) that estimates the frequency on the FM,
- Phase synchronization is carried out with a data-aided phase estimator operating on the FM and the pilots, with linear interpolation of the phase between pilot fields,
- SNR estimation with digital automatic gain control (DAGC) is based on estimators of the received average power.

Sections 5.3-5.7 show the design and performance analysis of the adopted algorithms, starting from the final stage till the first stage. Namely, at each stage, design and performance analysis are carried out assuming perfect synchronization of the previous stages. Hence, Section 5.3 will focus on the frame descriptor decoding assuming perfect estimation of frequency, phase, and SNR, while Section 5.7 will consider the performance of the full chain.

It is pointed out that this receiver is just a reference and it shall not be considered as optimal. Clock recovery (timing) and FM acquisition have been not considered in the simulation model adopted, since they are believed as straightforward. For instance, Gardner's timing recovery in [9] and the frame synchronization techniques based on correlation shown in [10] can be easily adopted.

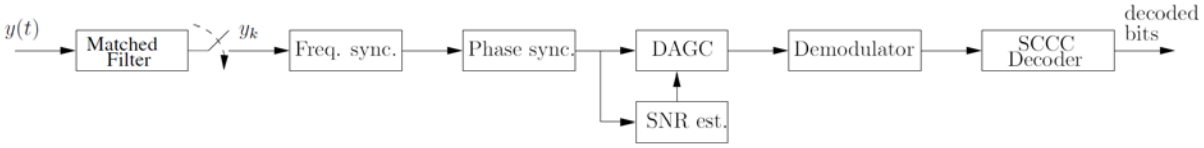

Figure 5-5: Synchronization scheme adopted for performance evaluation.

5.3 FRAME DESCRIPTOR DECODING

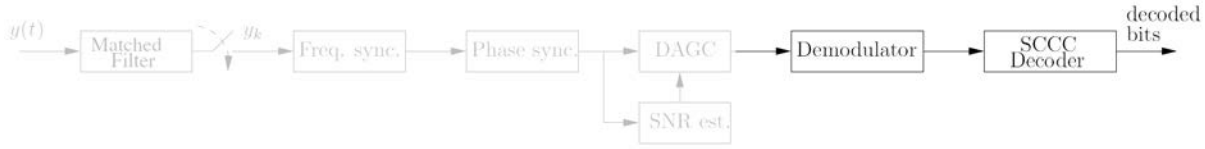

Figure 5-6: Highlight of the section of the synchronization scheme that is analyzed for FD decoding.

The synchronization chain is analyzed starting from the last stage as shown in Figure 5-6, i.e., at the demodulator input that computes LLRs for SCCC turbo decoding. At such stage, FD decoding shall be performed before constellation de-mapping.

Assuming perfect synchronization in terms of all previous stages, the performance of the FD code described in Section 2.1.1 has been analyzed for two different implementations of the FD decoder: maximum likelihood (ML) soft decoder versus a ML hard decoder. In turn, for both hard and soft decoding two cases have been considered:

- a decoding approach, that knowns that the 7th information bit b_7 of the FD is '0' (as currently set by the Recommended Standard), or
- a future-proof decoding approach, that assumes b_7 as extra bit of information to be decoded.

For these four cases, Figure 5-7 shows the FD error rate as function of E_s/N_0. It can be seen that the hard implementation achieves FD error rate equal to 1e-5 at $E_s/N_0 \cong -2$ dB, that is 1.4 dB below the minimum E_s/N_0 required for decoding all ACM format (see Table 3-1). Instead, a soft implementation of the FD decoder allows an extra 2 dB of margin, achieving FD error rate equal to 1e-5 at $E_s/N_0 \cong -4$ dB. Finally, it can be noticed that for both the soft and hard decoding the knowledge of b_7 allows a small improvement of 0.2 dB.

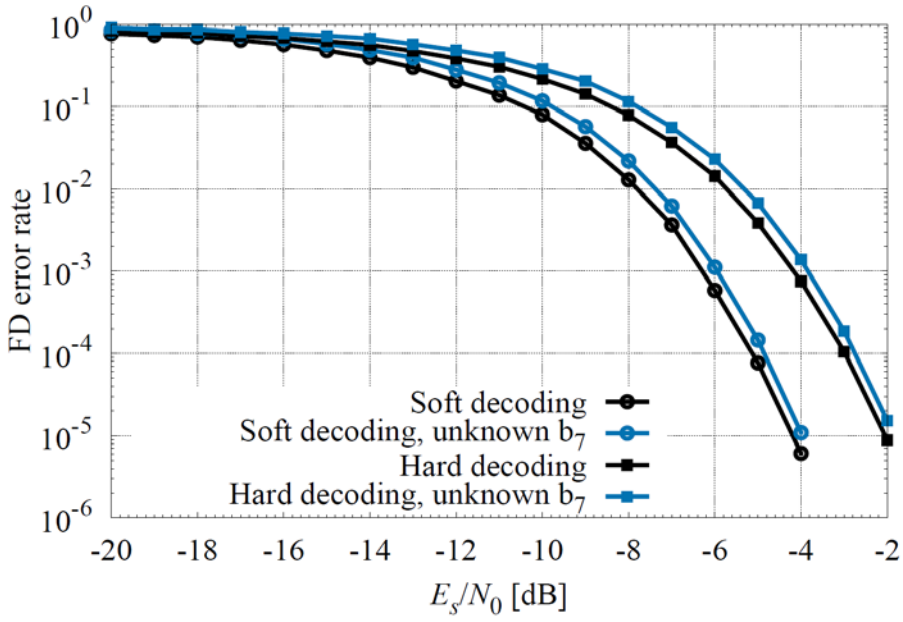

Figure 5-7: FD error rate with hard and soft decoding and whether bit b7 (currently set to 0 in [1]) is known at the receiver

5.4 SNR ESTIMATOR AND DAGC

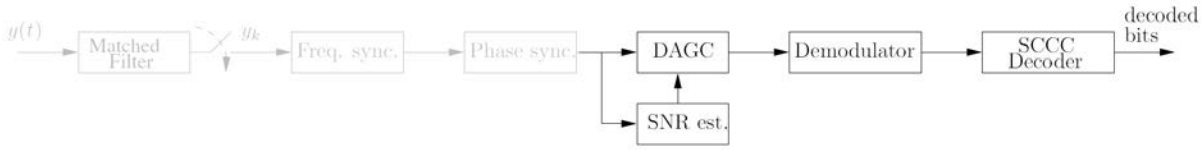

Figure 5-8: Highlight of the section of the synchronization scheme that is analyzed for SNR estimation and DAGC.

In this section the synchronization chain is analyzed and simulated starting at the input of the digital AGC (DAGC) and the SNR estimator as shown in Figure 5-8, assuming perfect frequency and phase synchronization.

The block diagram of this stage is shown in Figure 5-9. Its objective is to amplify the signal at the output of the phase synchronization (that will be denoted by r_k in following) such that the channel symbols at demodulator input have power P_{ref}. Without loss of generality, it was chosen P_{ref} such that channel symbols at demodulator input have unitary power, i.e., $P_{\text{ref}} = 1 + 1/(E_s/N_0)$. Notice that the SNR estimator and DAGC operate exclusively on the FM with removed modulation, i.e., by performing a multiplication $r_k x_{\text{p},k}^*$, where $x_{\text{p},k}^*$ is the complex conjugate of the k-th FM channel symbol.

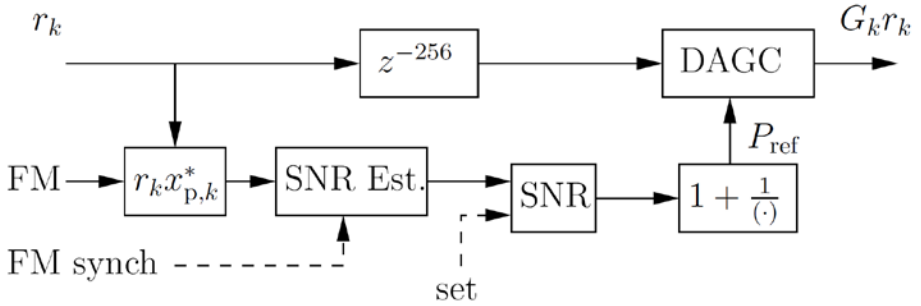

Figure 5-9: Detailed block diagram of the combined interaction between SNR estimator and DAGC.

For computing the SNR, a simple average power estimator was adopted as shown in Figure 5-10. In particular, the average of the in-phase component of $r_k x^*_{\text{p},k}$ (real part of the complex baseband model) is proportional to the square root of the energy-per-channel-symbol, i.e.,

$$E\{\mathcal{R}(r_k x^*_{\text{p},k})\} \propto \sqrt{E_s} \ ,$$

while

$$E\{\mathcal{R}^2(r_k x^*_{\text{p},k})\} \propto E_s + N_0/2 \ .$$

Hence, combining the two expressions above, the SNR can be found as

$$SNR = \frac{E_s}{N_0} = \frac{b^2}{2(a-b^2)}$$

where $a = E\{\mathcal{R}^2(r_k x^*_{\text{p},k})\}$ and $b = E\{\mathcal{R}(r_k x^*_{\text{p},k})\}$.

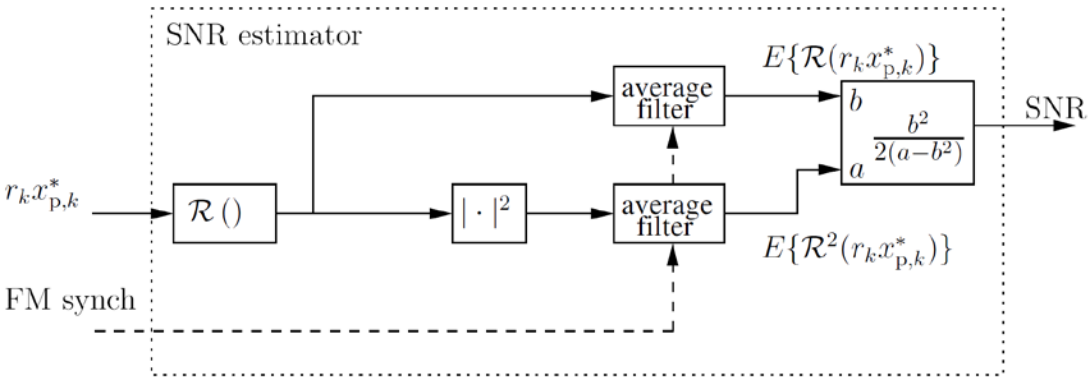

Figure 5-10: Adopted SNR estimator.

For the DAGC, a simple closed-loop algorithm was adopted as shown in Figure 5-11. In particular, the gain G_k is updated as

$$G_k = G_{k-1} + e_k \gamma_{\text{DAGC}} \ ,$$

where γ_{DAGC} is the open-loop gain, while e_k is the error, defined as

$$e_k = |G_k r_k|^2 - P_{\text{ref}} \ .$$

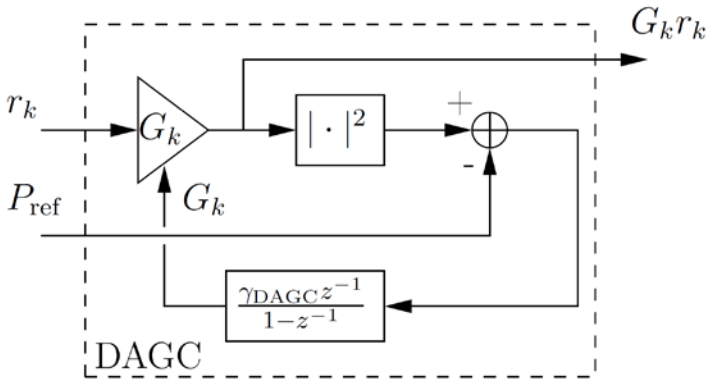

Figure 5-11: Adopted closed-loop DAGC.

Assuming perfect synchronization of the previous stages, the joint SNR estimator and DAGC have been simulated.

Figure 5-12 shows the convergence of the adopted SNR estimation. The estimated SNR is compared with the real SNR by varying the number of PL frames N_F. It can be seen that already at the first frame (i.e., by using only the first 256 FM channel symbols), the SNR estimator is able to provide a good estimation if $E_s/N_0 < 8$ dB, while for higher E_s/N_0 the estimation tends to diverge. It can be shown mathematically that this divergence is common to all SNR estimators, since an increase of the SNR makes the noise power level to be estimated more and more negligible [12]. Hence, for reducing the error is sufficient to adopt a higher number of frames, and already at 5-6 frames the estimation is perfect in the full SNR range for all ACM formats.

Figure 5-13 and Figure 5-14 show instead the convergence of the adopted closed-loop DAGC at low and high SNR, namely, $E_s/N_0 = -1.4$ dB (equivalent to $E_b/N_0 \cong 0$ for ACM format 1) and $E_s/N_0 = 18.5$ dB (equivalent to $E_b/N_0 \cong 11.2$ for ACM format 27). The convergence has been analyzed for different close-loop gain γ_{DAGC}. It is well known that for first-type closed-loop, the γ_{DAGC} shall be selected as trade-off between convergence speed and residual error [13]. By means of a preliminary coarse optimization $\gamma_{\text{DAGC}} = 1/160$ has been found the best for limiting the noise and achieving convergence by means of a single frame (for all ACMs), i.e., BER/CER curves show no losses w.r.t. the case with ideal synchronization.

Figure 5-15 and Figure 5-16 show the codeword error rate (CER) when using the joint SNR estimator and DAGC. CER is shown as function of the E_b/N_0 for a subset of the ACM formats, i.e., ACM format 1 and 6 (QPSK modulated), 12 (8PSK), 17 (16APSK), 22 (32APSK), and 27 (64APSK). For comparison also the CER with perfect synchronization is shown (colored solid lines). It can be seen that the adopted algorithms are able to synchronize almost perfectly, with performance near to optimal, while a poor selection of γ_{DAGC} can cause a non-negligible loss.

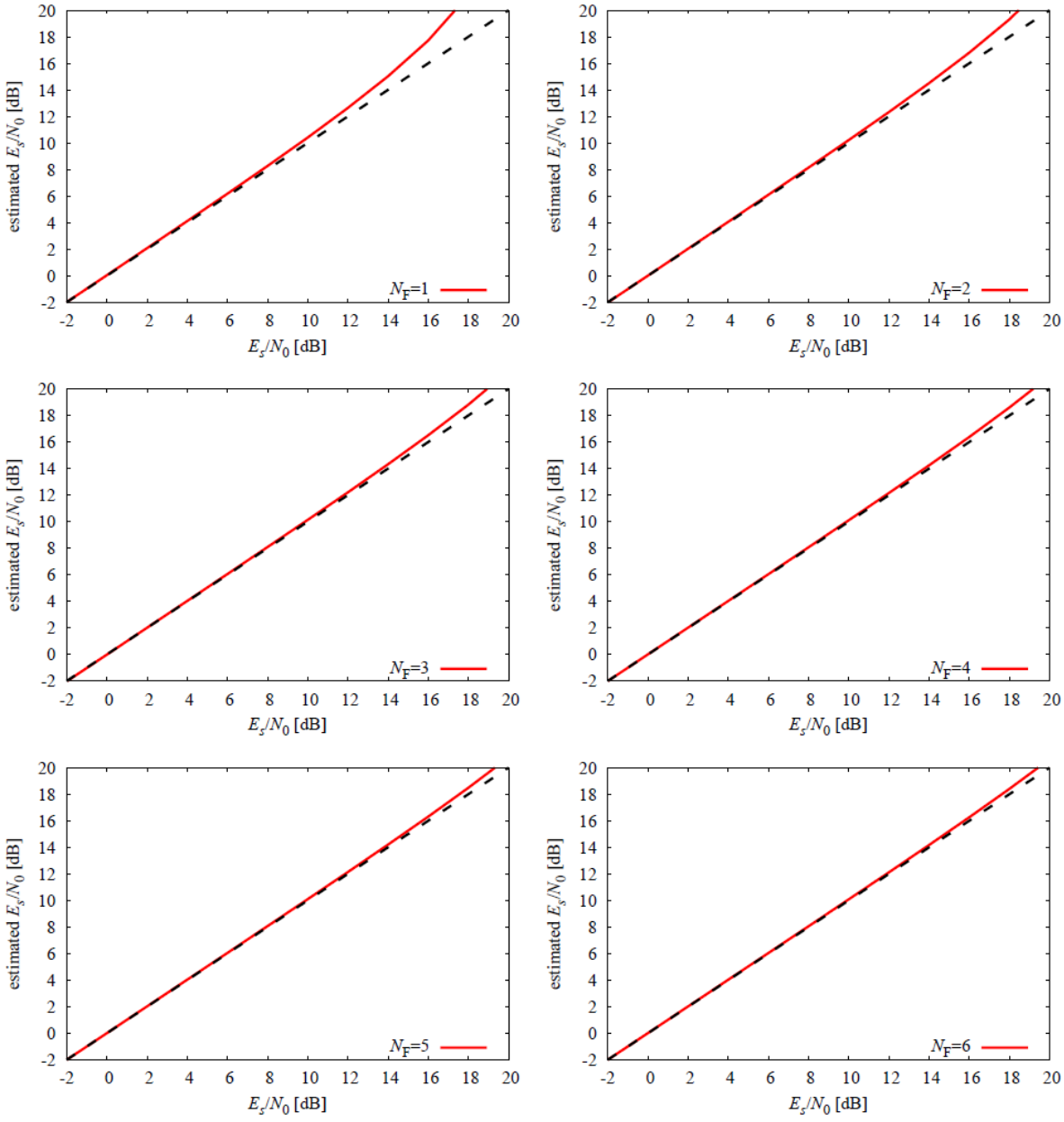

Figure 5-12: Estimated SNR versus real SNR for different number of PL frames adopted.

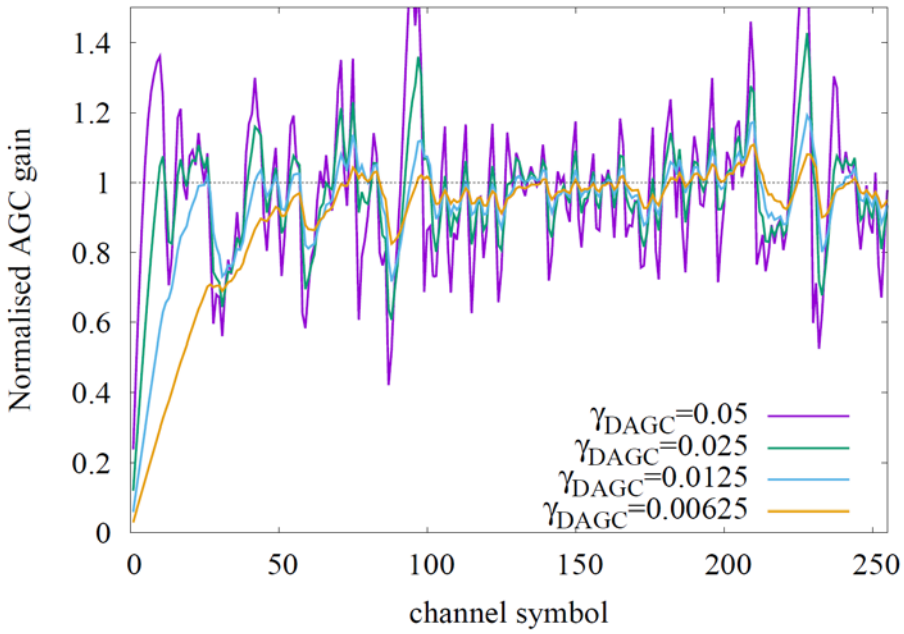

Figure 5-13: Convergence of the DAGC gain at Es/N0=-1.4 dB (Eb/N0= 0.0 dB for ACM 1).

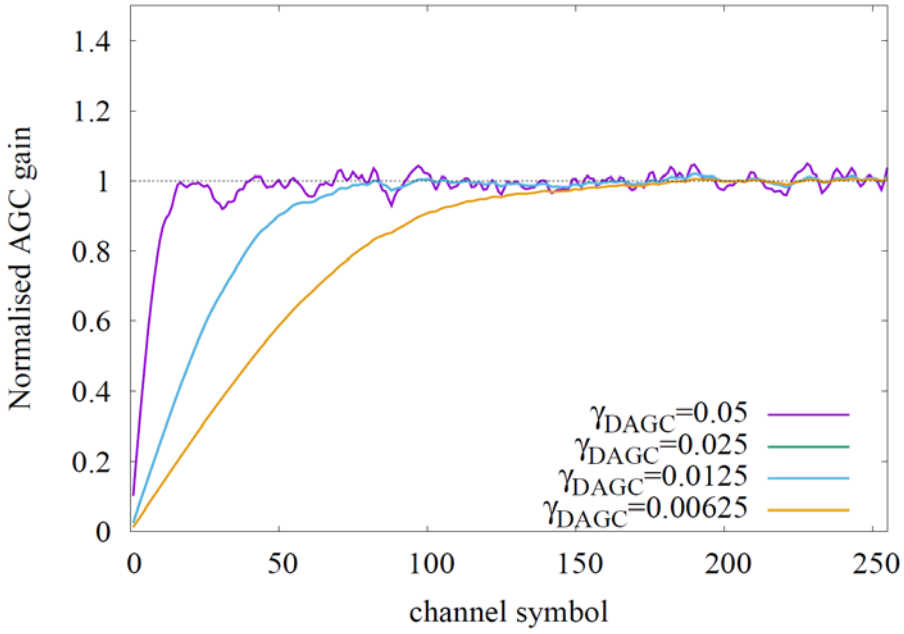

Figure 5-14: Convergence of the DAGC gain at Es/N0= 18.5 dB (Eb/N0=11.2 dB for ACM 27).

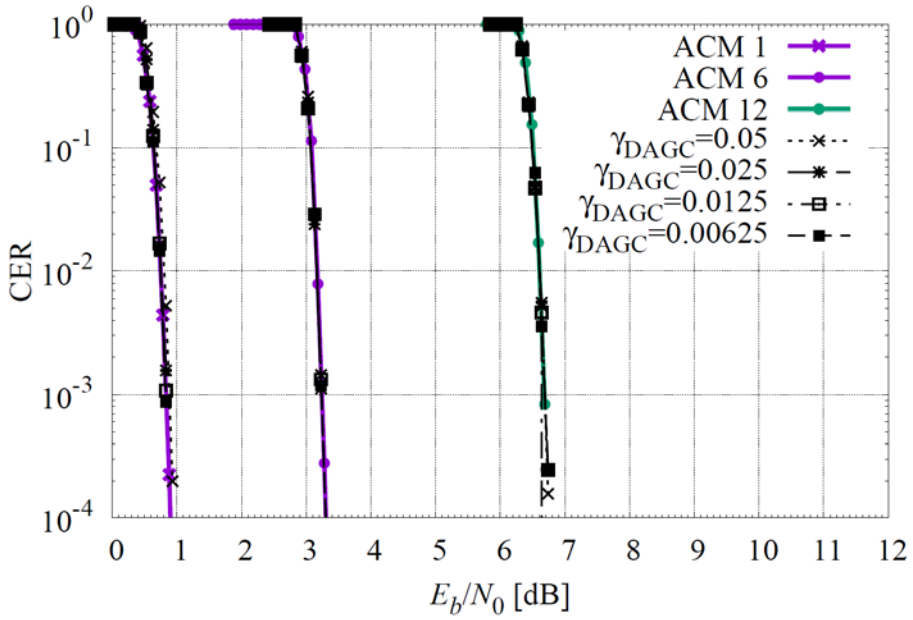

Figure 5-15: CER for ACM 1, 17, and 22 (PSK modulations), for different values of the DAGC loop gain

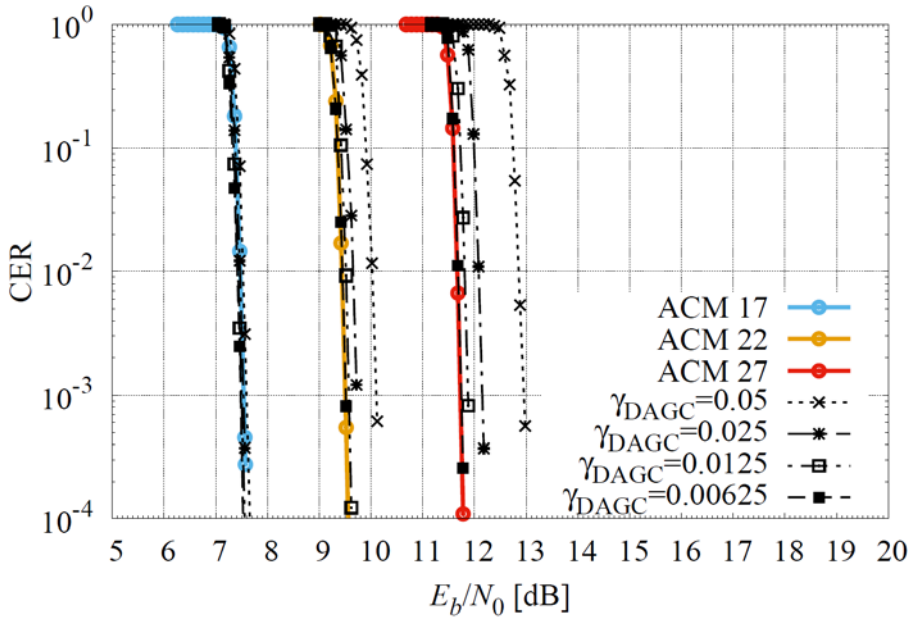

Figure 5-16: CER for ACM 1, 17, and 22 (APSK modulations), for different values of the DAGC loop gain

5.5 PHASE SYNCHRONIZATION

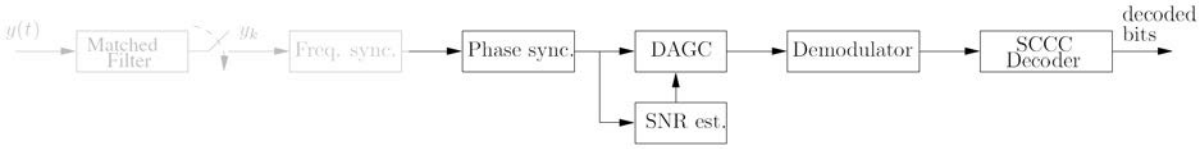

Figure 5-17: Highlight of the section of the synchronization scheme that is analyzed for phase synchronization.

In this section the synchronization chain is analyzed and simulated starting at the input of the phase synchronizer as shown in Figure 5-17, assuming perfect frequency synchronization.

The adopted algorithm is based on a ML estimator operating on the frame marker and pilot fields. The estimated phase values are then linearly interpolated between fields. It is pointed out that this algorithm operates at PL frame level, hence it can be carried out independently frame by frame.

Concerning the ML estimation, if $\{r_k\}$ is (with a little abuse of notation) the signal samples at the input of the phase synchronizer, with $k = 1$ identifying the first channel symbol of the PL frame, the phases on each m-th pilot field are estimated as

$$\theta_{\mathrm{p}}^{(m)} = \mathrm{angle}\left(\sum_{i=0}^{15} r_{k+i} x_{\mathrm{p},k+i}^{*}\right), \qquad \begin{matrix} m = 1, \ldots, 16 \\ k = 556m + 305 \end{matrix} .$$

Similarly, the phase estimation on the FM is carried out with the formula above by dividing the FM in blocks of 16 symbols each. This approach has been found a good trade-off for limiting the impact of possible residual frequency errors after frequency synchronization on the FM that is then adopted for SNR estimation.

Between two phase estimates (separated by 540 channel symbols), $\theta_{\mathrm{p}}^{(m)}$ and $\theta_{\mathrm{p}}^{(m+1)}$, a linear interpolation is performed. Hence, the phase on the channel symbols can be estimated as

$$\theta_{k+\ell} = \frac{(\theta_{\mathrm{p}}^{(m+1)} - \theta_{\mathrm{p}}^{(m)})}{541}\ell + \theta_{\mathrm{p}}^{(m)} \quad , \quad \begin{matrix} k = 556m + 320 \\ \ell = 1, \ldots, 540 \end{matrix} ,$$

where sum and subtraction are performed as modulo operation in the co-domain $(-\pi, \pi]$ for taking into account phase wraps [14].

Figure 5-18 shows a sketch on how the adopted phase synchronization algorithm works: assuming a phase noise process as depicted in purple, the estimator provides a constant phase on the pilot fields, i.e., $\theta_{\mathrm{p}}^{(1)}$, $\theta_{\mathrm{p}}^{(2)}$, …, that are then linearly interpolated each other as shown by the green solid line. On the FM, as mentioned, the estimation is done instead in chunks of 16 channel symbols. Hence, only the estimation provided by the last 16 FM channel symbols is then interpolated with $\theta_{\mathrm{p}}^{(1)}$.

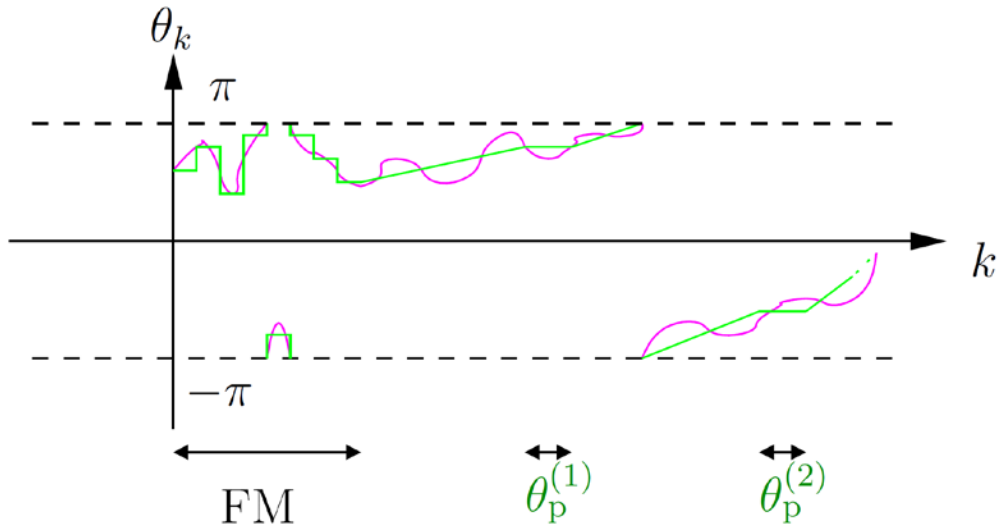

Figure 5-18: Sketch of the phase linear interpolation.

Figure 5-19 and Figure 5-20 show the CER when using the phase synchronization algorithm discussed. CER is shown as function of the E_b/N_0 for a subset of the ACM formats, i.e., ACM format 1 and 6 (QPSK modulated), 12 (8PSK), 17 (16APSK), 22 (32APSK), and 27 (64APSK). It can be seen that the adopted algorithm is able to synchronize with a loss between 0.2-0.4 dB with respect to AWGN with ideal synchronization.

It is interesting to notice that by increasing the SNR, the loss from AWGN curves does not tend to decrease. In fact, although at higher SNR the phase estimation improves, the adopted ACM formats relies on high-cardinality APSK constellations and on SCCC with high rate, providing hence less tolerance to phase errors. On the other hand, at low SNR the adopted phase estimator provides a noisy estimation, that is mitigate only thanks to low cardinality and low rate SCCC. This can be better seen from Figure 5-21 to Figure 5-24. In these figures, a realization of the phase noise is shown versus the phase estimated by the proposed algorithm at low SNR ($E_b/N_0 = 1.3$ dB for ACM format 1) and high SNR ($E_b/N_0 = 12.3$ dB for ACM format 27), and with and without a frequency shift (250 Hz, arbitrary value just for illustration purposes). At low SNR the phase estimator performance are very poor, and tends to follow only low frequency components but, as mentioned, the ACM format is well protected by QPSK with low rate SCCC. At high SNR the phase estimator performance improves but, as shown by CER curves, the ACM format is more sensitive to the residual phase error.

As already pointed out in previous sections, the phase synchronization can be improved, hence the proposed algorithm shall not be taken as optimal. For instance, a possible alternative that could improve results for certain ModCods is the use of a phase-locked loop (PLL) that is data aided on FM and pilot fields, and decision direct on the other channel symbols.

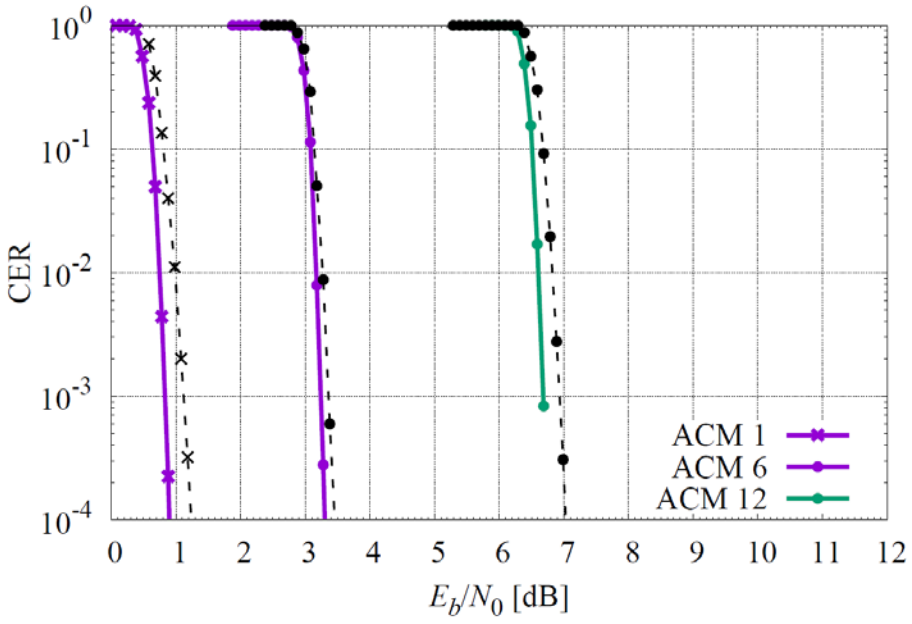

Figure 5-19: CER for ACM format 1, 6, and 12 (PSK modulations) in presence of phase noise and using a phase synchronizer with linear interpolation.

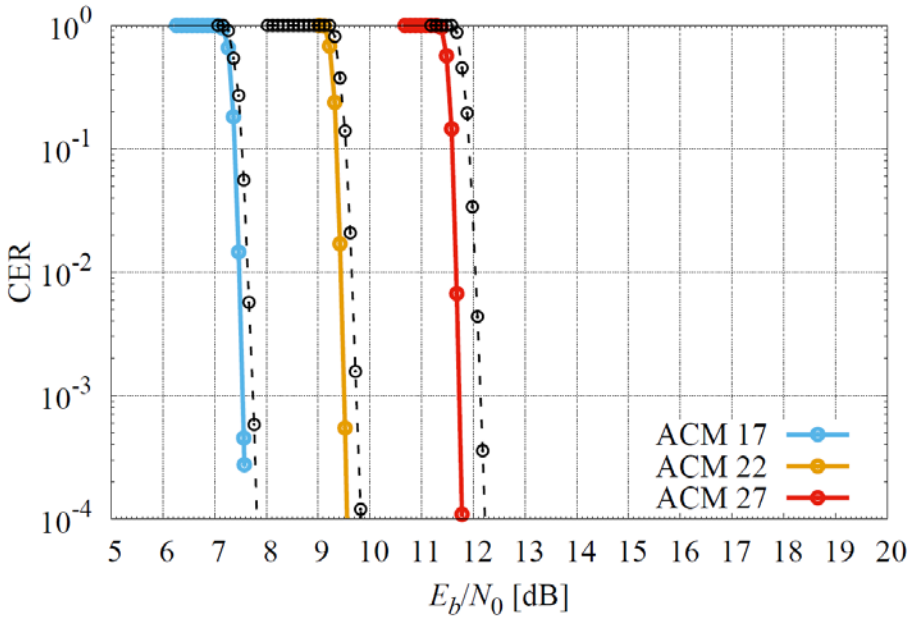

Figure 5-20: CER for ACM format 17, 22, and 27 (APSK modulations) in presence of phase noise and using a phase synchronizer with linear interpolation.

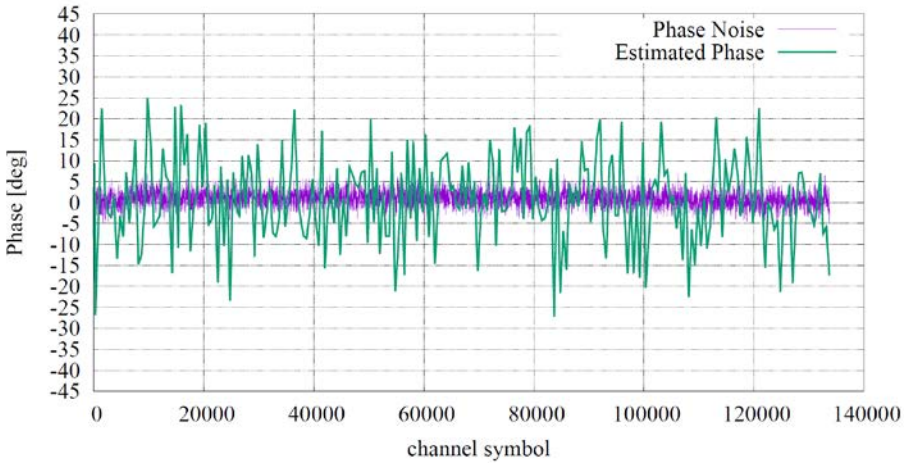

Figure 5-21: Phase noise versus tracked phase for ACM 1 at Eb/N0=1.3 dB.

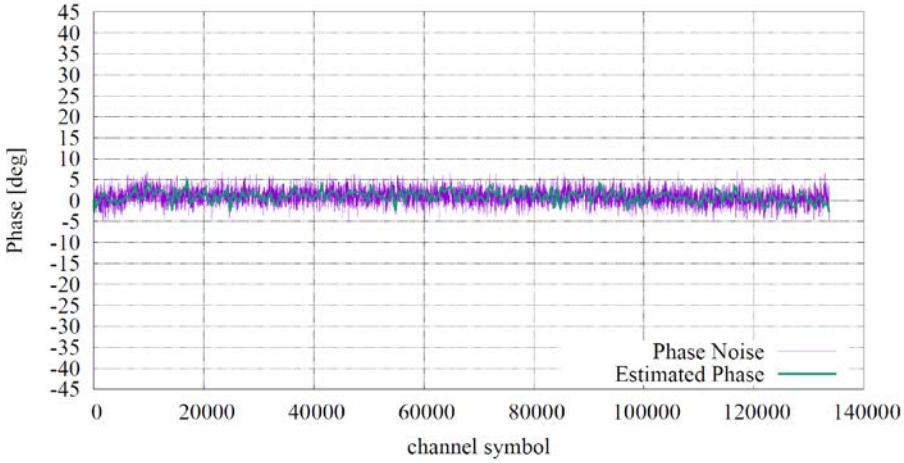

Figure 5-22: Phase noise versus tracked phase for ACM 27 at Eb/N0=12.3 dB.

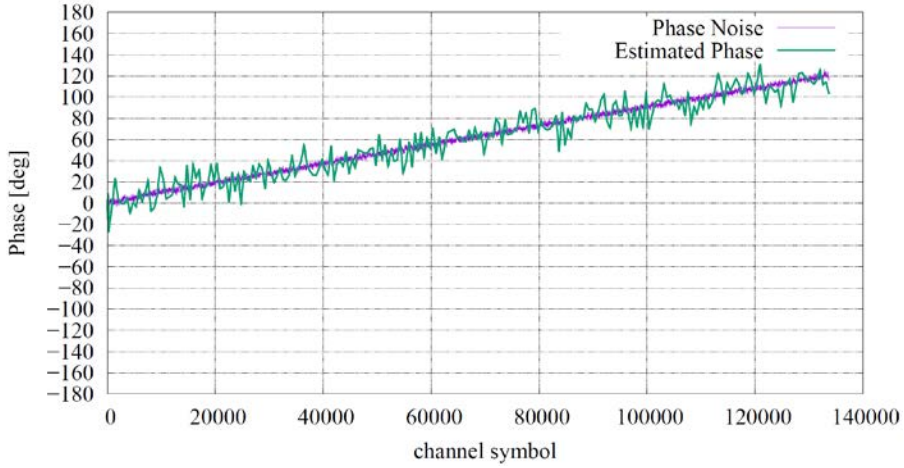

Figure 5-23: Phase noise with frequency shift of 250 Hz, versus tracked phase for ACM 1 at Eb/N0=1.3 dB.

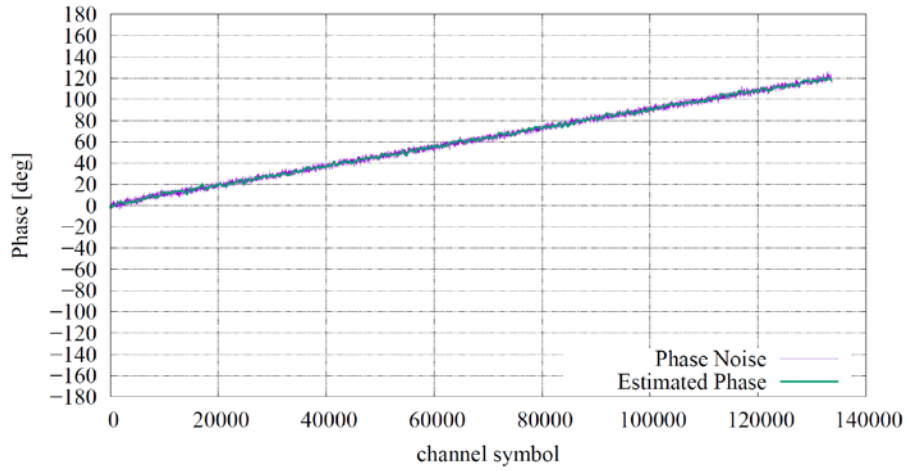

Figure 5-24: Phase noise with frequency shift of 250 Hz, versus tracked phase for ACM 27 at Eb/N0=12.3 dB.

5.6 FREQUENCY SYNCHRONIZATION

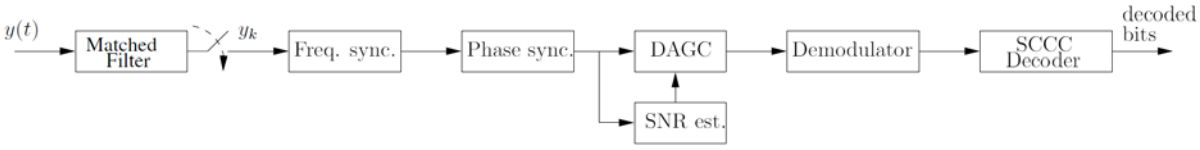

Figure 5-25: Synchronization scheme that is analyzed for frequency synchronization.

In this section the frequency synchronization is analyzed for the chain shown in Figure 5-25, when all the following stages are the ones studied in previous sections.

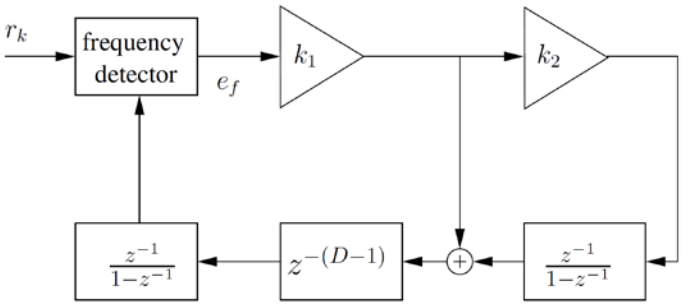

Figure 5-26: Adopted FLL.

The adopted frequency synchronization algorithm is based on a digital second-type FLL working at frame level as shown in Figure 5-26. The frequency detector computes the error e_f between real and estimated frequency. The error is then fed to a loop filter, characterized by the gains k_1 and k_2 and excess delay equal to $D = 2$ (for taking into account a possible process delay of real implementations [13]). Notice that when $k_2 = 0$, the FLL reduced to the first type.

With regard the frequency detector, a fast Fourier transform (FFT) approach has been adopted. Namely, a FFT with 1024 points was done on the 256 channel symbols of the FM. With abuse of notation, if $\{r_k\}$ is defined as the sequence of samples at the input of the

frequency synchronizer (with $k = 1$ identifying the first channel symbol of the PL frame under processing) the FFT operation reads

$$R_\ell = \sum_{k=1}^{256} r_k x_{\mathrm{p},k}^* \, e^{-j2\pi(k-1)\frac{\ell}{1024}} \quad , \qquad \ell = -511, \ldots, 0, \ldots, 512$$

where $x_{\mathrm{p},k}^*$ is the complex conjugate of the k-th FM channel symbol. The magnitude of R_ℓ provides information about the frequency bin centered in $\ell R_{chs}/1024$. Hence, the frequency error can be estimated as

$$e_f = \mathrm{argmax}_\ell |R_\ell| \quad .$$

However, this method is limited by the resolution of the FFT. Hence, for improving the resolution of e_f Newton interpolation is done around the maximum.

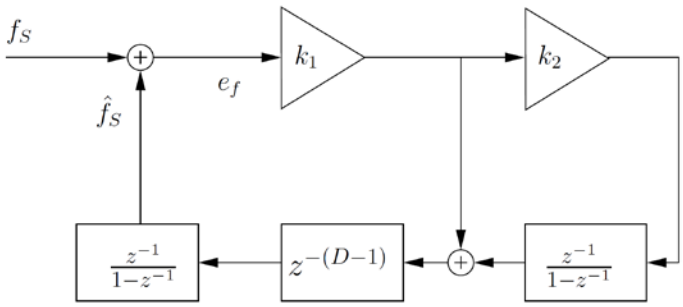

Figure 5-27: Linearized scheme of the adopted FLL.

For this FLL, it can be shown that the linearized equivalent scheme is the one shown in Figure 5-27. Such FLL has a noise bandwidth B_L well approximated by the following formula [13]

$$B_L \cong \frac{R_{FM}}{4}(k_1 + k_2) \quad ,$$

where R_{FM} is the number of FM (or PL frames) per second, i.e., $R_{FM} = R_{chs}/133760$ (when using pilot fields), while the SNR in the loop is given by

$$\mathrm{SNR}_{\mathrm{FLL}} = \frac{E_s R_{FM} 256}{N_0 B_L} \quad .$$

Considering that for stability reasons $(k_1 + k_2) < 1$, and that $E_s/N_0 > -0.6$ dB for all ACM formats (see AWGN results in Section 3.2), at 100 MBaud it holds that $B_L < 186.9$ Hz, hence

$$\mathrm{SNR}_{\mathrm{FLL}} > 29.5 \quad \mathrm{dB} \quad ,$$

or in other terms the adopted FLL works in almost noise-less conditions. This can be easily seen by the following figures. Figure 5-28 shows the theoretical convergence of the

frequency error of the FLL linearized scheme for different k_1 (k_2 =0 for sake of simplicity), for constant Doppler shift. Figure 5-29 shows instead the convergence of the frequency error for the adopted FLL with FFT-based frequency detector and when simulating the ACM format in noisy conditions ($E_s/N_0 = -0.9$ dB, i.e., $E_b/N_0 = 0.6$ dB for ACM format 1). It can be seen that the real convergence has perfect match with the theoretical convergence, proving that noise has no impact.

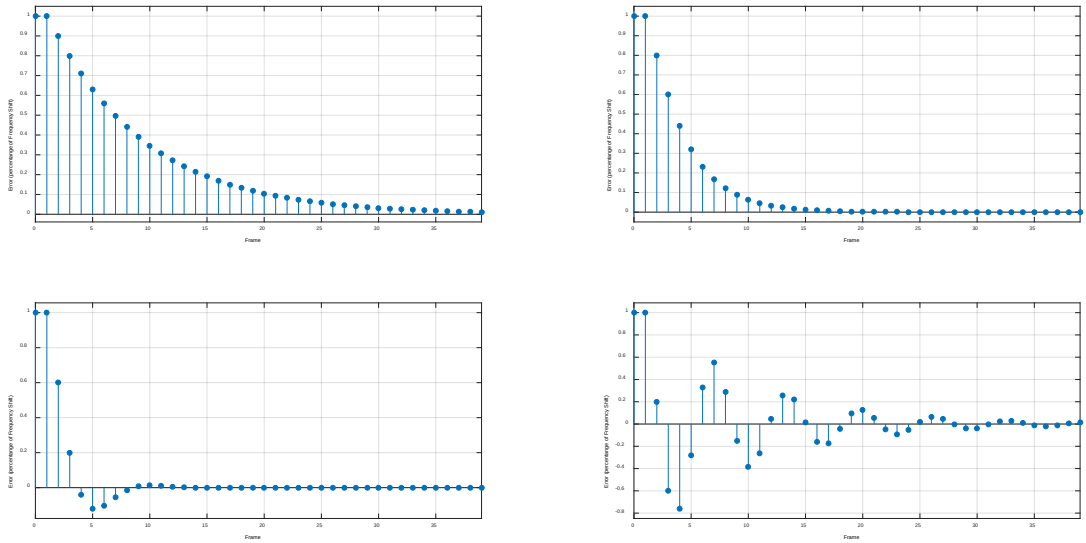

Figure 5-28: Theoretical frequency error convergence (in absence of thermal noise) for the linearized scheme when (left to right) k1 is 0.1, 0.2, 0.4, and 0.8.

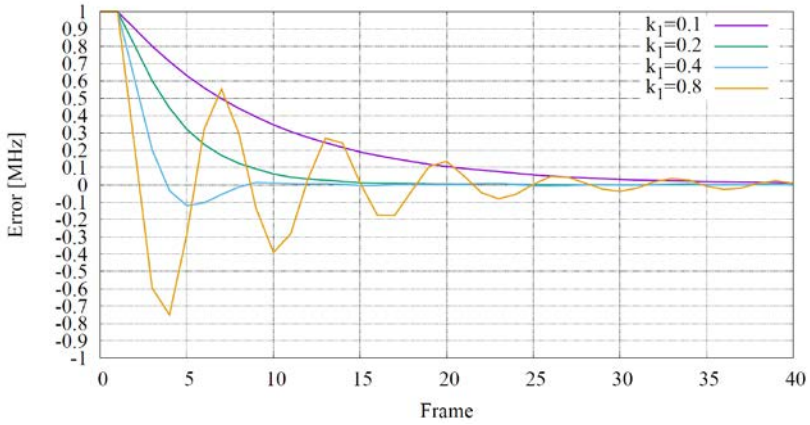

Figure 5-29: Simulated frequency error convergence Es/N0=-0.9 dB (Eb/N0=0.6 dB for ACM1).

For tuning the FLL coefficients k_1 and k_2, the FLL has been tested with the Doppler profiles described in Section 5.1. For Doppler shifts up to 1 MHz, and Doppler rate 50 kHz/s, it has been found that a FLL of the first type $k_1 = 0.2$, $k_2 = 0$ is more than sufficient, since the residual error due to Doppler rate is compensated by the phase synchronizer. Hence, the FLL can be simplified in favor of the adopted phase synchronization algorithm. For the reader reference, the detailed analysis of the FLL tuning is reported in Annex A.

5.7 NUMERICAL RESULTS

The performance results of the Recommended Standard's modulation and coding scheme has been evaluated over the AWGN channel affected by phase noise and Doppler of Section 5.1, and with the synchronization chain described in previous sections.

Figure 5-30 and Figure 5-31 show the CER as function of the E_b/N_0 for a subset of the ACM formats, i.e., ACM format 1 and 6 (QPSK modulated), 12 (8PSK), 17 (16APSK), 22 (32APSK), and 27 (64APSK). For comparison also the CER with perfect synchronization is shown (colored solid lines). It can be seen that the adopted algorithms are able to synchronize with a performance loss between 0.2-0.4 dB (at CER=1e-4) with respect to AWGN with ideal synchronization. Finally, it is pointed out that CER has been computed also adopting the triangular Doppler profile and identical results were found.

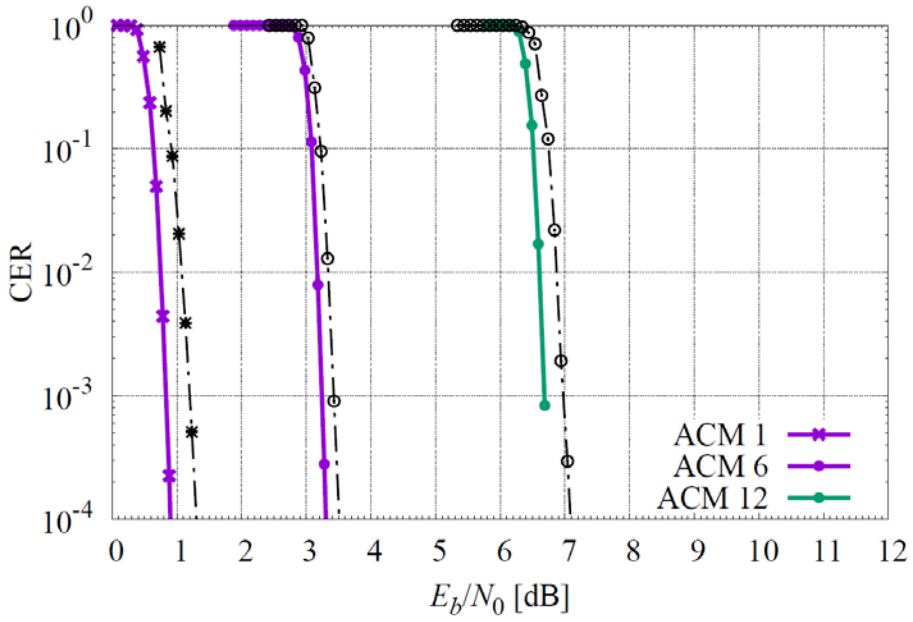

Figure 5-30: CER for ACM format 1, 6, and 12 (PSK modulations) in presence of sinusoidal Doppler profile (f_D = 1 MHz, f_R = 50 kHz/sec) and phase noise when using the described synchronization chain.

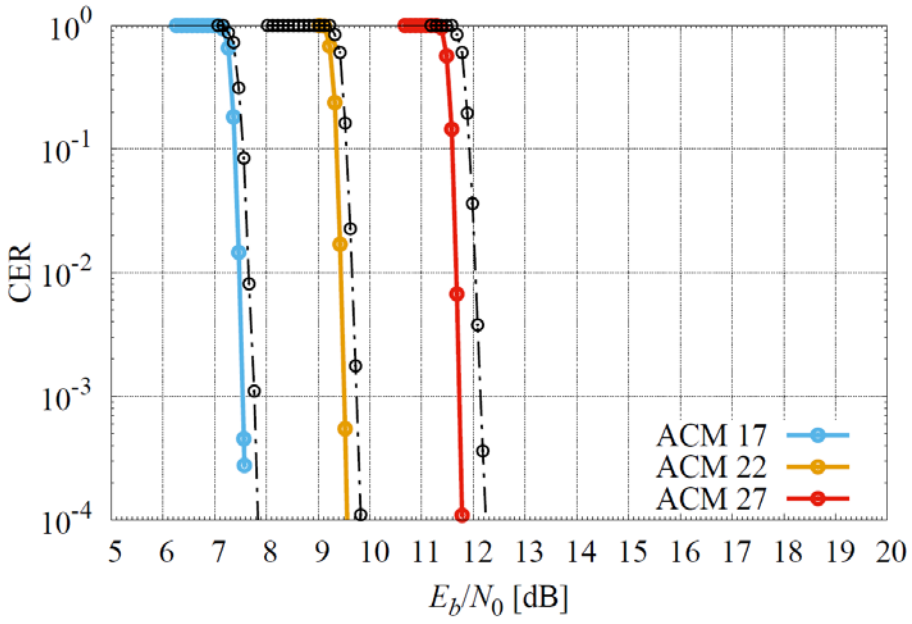

Figure 5-31: CER for ACM format 17, 22, and 27 (APSK modulations) in presence of sinusoidal Doppler profile ($f_D = 1$ MHz, $f_R = 50$ kHz/sec) and phase noise when using the described synchronization chain.

6 END-TO-END SIMULATIONS

In this section, the performance of the recommended codes and modulations is evaluated by means of end-to-end simulations. In particular this section considers the nonlinear channel of Section 4 and the synchronization chain of Section 5. The optimal input and output back-off (IBO/OBO) is re-verified by means of the total degradation provided in Section 6.1. This is done for verifying the possible increase of the required back-off for making the synchronization chain working in presence of nonlinear distortions. Then, performance are assessed for all 27 ACM formats in Section 6.2, where it will be also shown how pre-distortion can improve the performance, especially for ACMs 13-27 that use APSK modulations.

6.1 TOTAL DEGRADATION

Similarly to Section 4, the adopted total degradation definition for end-to-end simulations is defined as

$$TD = \left(\frac{E_b}{N_0} + \mathrm{OBO}\right)_{\mathrm{E2E}} - \left(\frac{E_b}{N_0}\right)_{\mathrm{AWGN}} \qquad [\mathrm{dB}]$$

where $\left(\frac{E_b}{N_0} + \mathrm{OBO}\right)_{\mathrm{E2E}}$ is the signal-to-noise ratio and OBO required for obtaining a specific target codeword error rate (CER) with the assumed channel model and receiver. The value $\left(\frac{E_b}{N_0}\right)_{\mathrm{AWGN}}$ represents instead the signal-to-noise ratio required on the ideal AWGN channel with ideal synchronization to achieve the same target CER. A target CER equal to 10^{-4} has been adopted. Notice that, differently from Section 4, TD does provide not only a useful representation of the overall losses experienced by the link (in terms of distortion as well as reduced available power due to the back-off) but also due to the synchronization in presence of phase noise and Doppler. Hence, the optimal IBO/OBO is found as the value that minimizes TD (see Section 4.2 for optimization examples).

6.2 NUMERICAL RESULTS

6.2.1 TOTAL DEGRADATION AND ERROR RATE CURVES

Figure 6-1 shows the total degradation for a subset of the ACM formats as function of the IBO, in particular ACM format 1 and 6 (QPSK modulated), 12 (8PSK), 17 (16APSK), 22 (32APSK). For comparison the total degradation with ideal synchronization (results of Section 4.3.1) have been reported. From the figure it can be seen that optimal IBO/OBO is approximately still the same of the one found when using ideal synchronization. On the other hand, a performance loss between 0.2 dB and 0.8 dB is found due to the synchronization in presence of phase noise, Doppler, and nonlinear distortions.

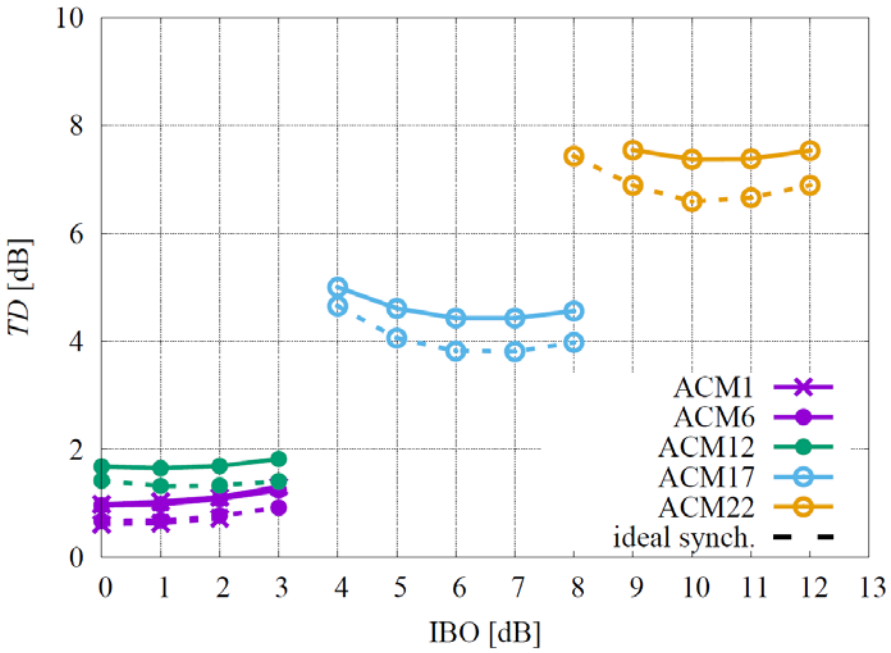

Figure 6-1: TD (end-to-end) for ACM formats 1, 6, 12, 17, and 22.

Different conclusions were found for the ACM formats from 23 till 27, that are based on the 64APSK. Figure 6-2 shows the total degradation as function of IBO compared with ideal synchronization (results of Section 4.3.1). It can be seen that the synchronization chain for the 64APSK is highly penalized by nonlinear effects, and even increasing the back-off, losses as high as 2 dB can be experienced. The reason of such penalty has been found in the phase synchronizer. In particular, the adopted phase synchronization algorithm relies on the estimation done on the FM and pilots whose I/Q amplitude with respect to 64APSK channel symbols is as shown in Figure 6-3. Hence after phase synchronization, the I/Q samples (see the figure) of the intermediate circles will be well aligned with respect the original constellation, while the external circle (representing 43% of the probability) will be misaligned. As further evidence, the CER for the ACM format 27 has been computed in Figure 6-4 when different impairments are enabled step by step. It can be seen, that the figure confirms that the loss is mostly due to the phase synchronization in presence of nonlinearities, while the fraction of loss due to phase noise is similar to the one seen in the linear channel in Section 5.5. Hence, for 64APSK the use of pre-distortion at the transmitter (discussed in next section) appears almost mandatory.

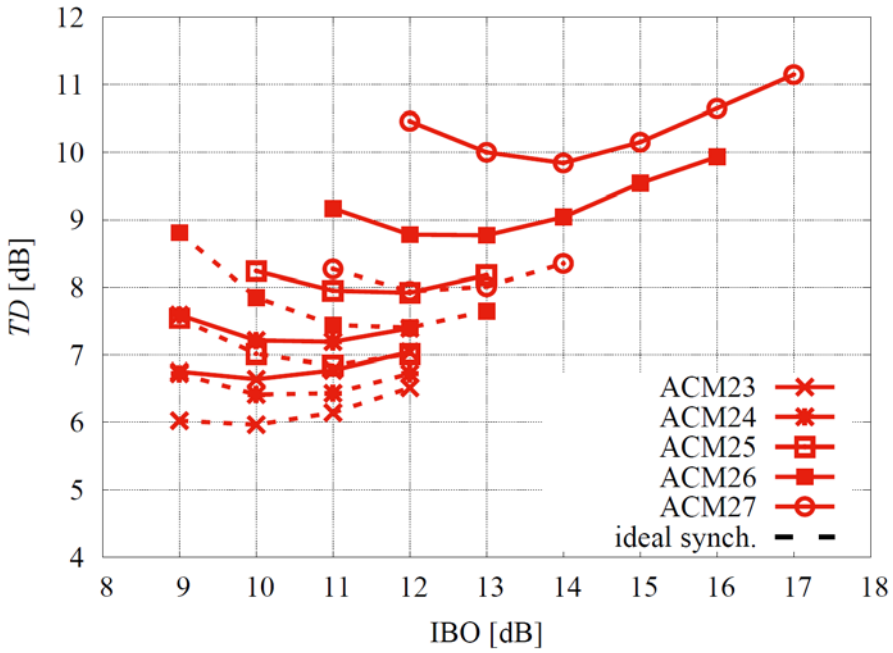

Figure 6-2: TD (end-to-end) for ACM formats from 23 till 27 (64APSK).

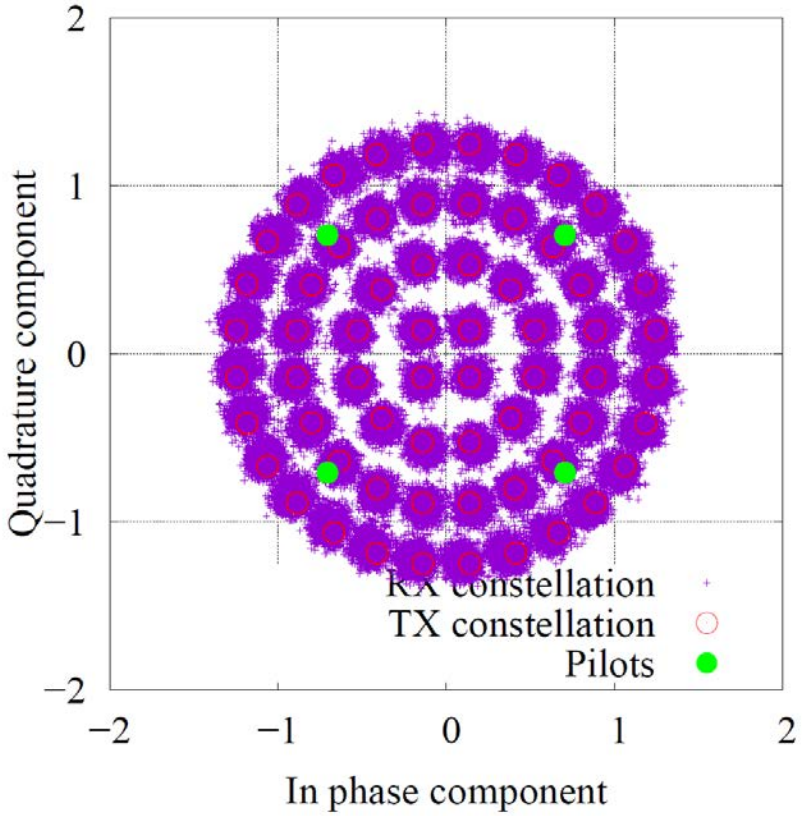

Figure 6-3: Scattering at the demodulator input for ACM27 at Eb/N0=17.5 dB, IBO=14 dB.

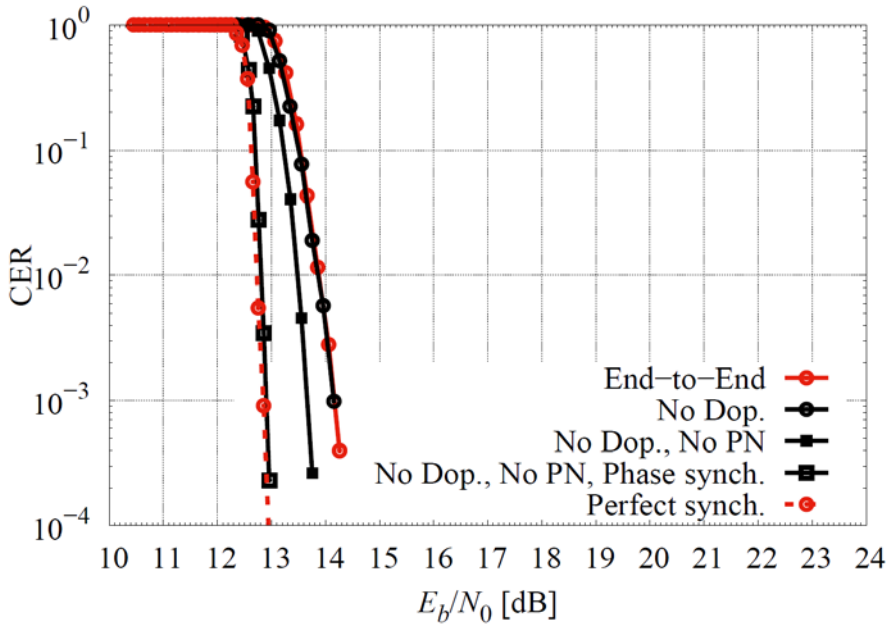

Figure 6-4: CER for ACM format 27, IBO=14 dB, for different impairments.

From Figure 6-5 to Figure 6-8 is shown the BER and CER for all the possible ACM formats using the optimal IBO found by means of the total degradation analysis. The corresponding SNR thresholds for CER equal to 10^{-4} and OBO for each individual ACM mode (to be taken into account when performing system level design) can be found in Table 6-1.

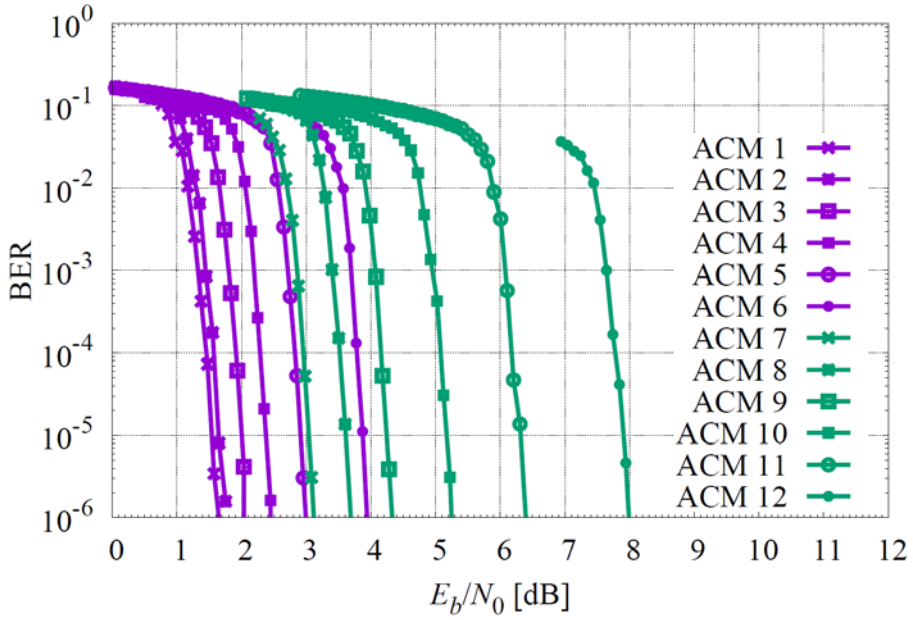

Figure 6-5: BER (end-to-end) for ACM formats from 1 to 12 (PSK modulations) with the optimal IBO.

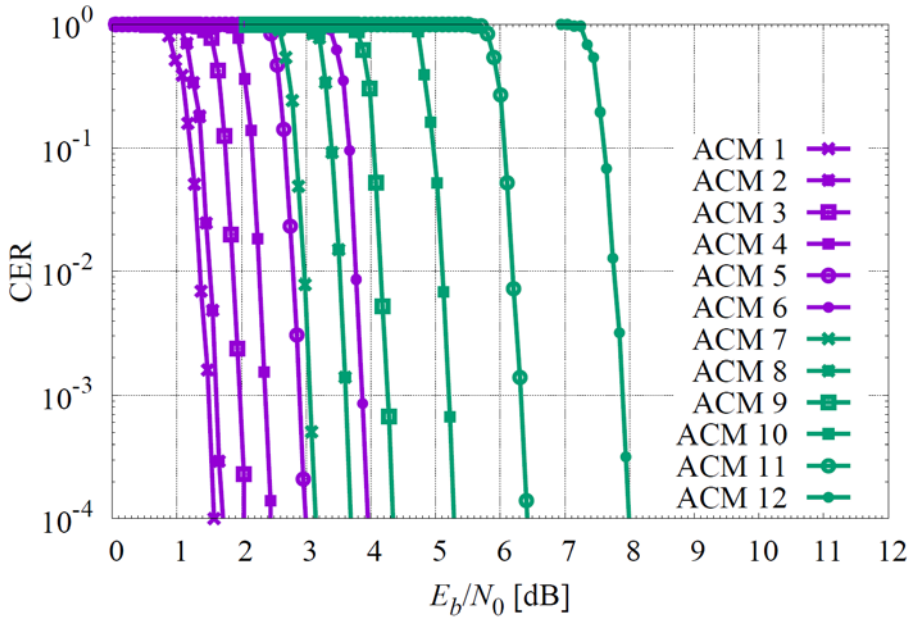

Figure 6-6: CER (end-to-end) for ACM formats from 1 to 12 (PSK modulations) with the optimal IBO.

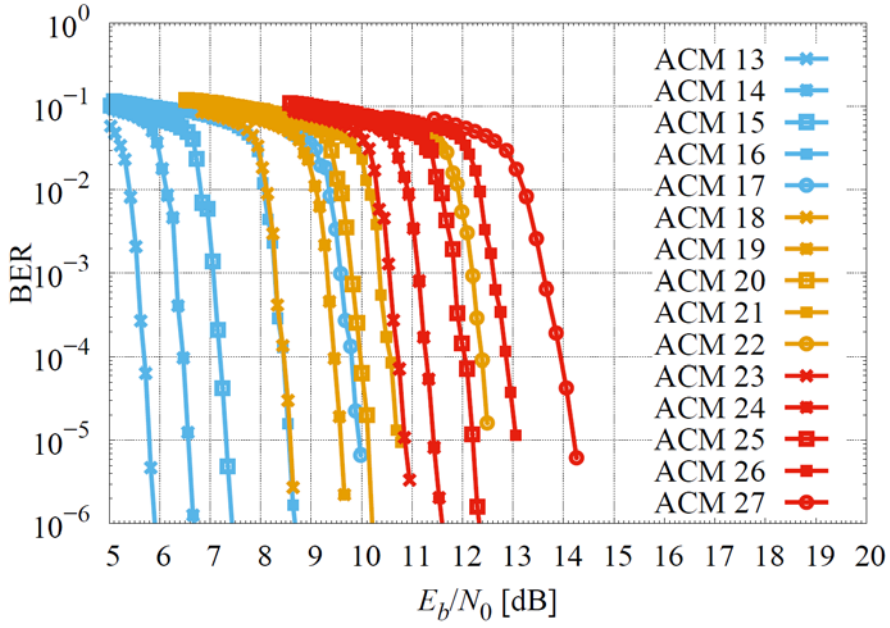

Figure 6-7: BER (end-to-end) for ACM formats from 13 to 27 (APSK modulations) with the optimal IBO.

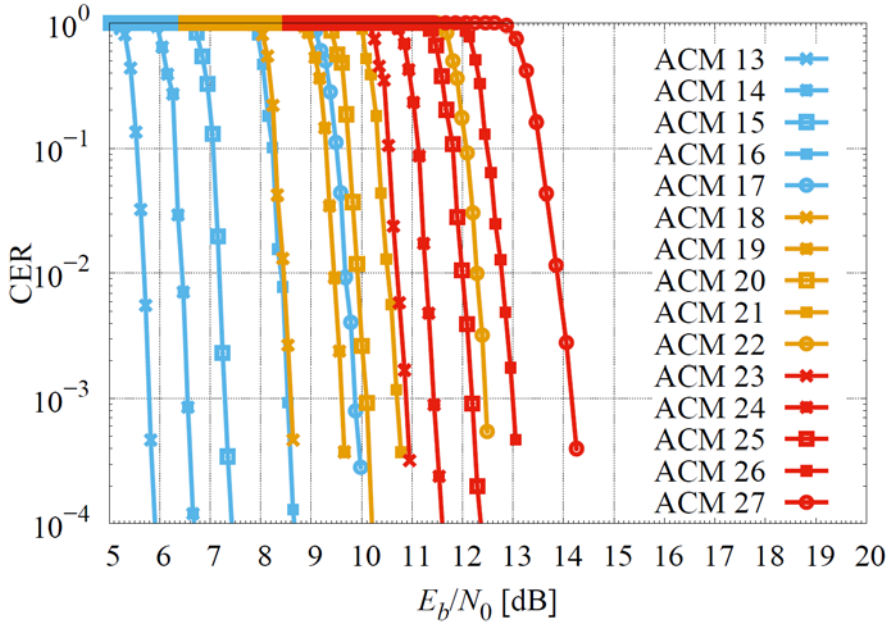

Figure 6-8: CER (end-to-end) for ACM formats from 13 to 27 (APSK modulations) with the optimal IBO.

Table 6-1: SNR thresholds for CER=1e-4, and corresponding OBO, TD, and bandwidth (for SRRC roll-off 0.35 after RF filtering), achieved by the recommended ACM formats with SRRC roll-off 0.35 in end-to-end simulations and without pre-distortion.

	ACM	E_s/N_0 [dB]	E_b/N_0 [dB]	OBO [dB]	TD [dB]	Bandwidth
QPSK	1	0.08	1.57	0.32	0.98	$1.29 \cdot R_{chs}$
	2	1.04	1.70	0.32	0.94	$1.29 \cdot R_{chs}$
	3	2.22	2.05	0.32	0.94	$1.29 \cdot R_{chs}$
	4	3.29	2.47	0.32	0.90	$1.29 \cdot R_{chs}$
	5	4.42	2.99	0.32	0.91	$1.29 \cdot R_{chs}$
	6	6.06	3.94	0.32	0.96	$1.29 \cdot R_{chs}$
8PSK	7	4.57	3.14	0.29	0.95	$1.29 \cdot R_{chs}$
	8	5.80	3.68	0.29	0.99	$1.29 \cdot R_{chs}$
	9	6.97	4.32	0.29	1.01	$1.29 \cdot R_{chs}$
	10	8.50	5.28	0.36	1.11	$1.27 \cdot R_{chs}$
	11	10.15	6.41	0.36	1.30	$1.27 \cdot R_{chs}$
	12	12.19	7.97	0.36	1.65	$1.27 \cdot R_{chs}$
16APSK	13	9.62	5.87	1.34	2.78	$1.24 \cdot R_{chs}$
	14	10.87	6.65	1.34	2.97	$1.24 \cdot R_{chs}$
	15	12.01	7.39	1.63	3.30	$1.23 \cdot R_{chs}$
	16	13.68	8.63	1.63	3.76	$1.23 \cdot R_{chs}$
	17	15.46	10.02	1.99	4.43	$1.21 \cdot R_{chs}$
32APSK	18	13.77	8.72	3.12	5.43	$1.20 \cdot R_{chs}$
	19	15.15	9.71	3.12	5.75	$1.20 \cdot R_{chs}$
	20	16.00	10.18	3.68	6.19	$1.19 \cdot R_{chs}$
	21	17.04	10.90	4.27	6.69	$1.18 \cdot R_{chs}$
	22	19.14	12.66	4.27	7.37	$1.18 \cdot R_{chs}$
64APSK	23	17.17	11.02	4.21	6.64	$1.18 \cdot R_{chs}$
	24	18.05	11.57	4.88	7.19	$1.18 \cdot R_{chs}$
	25	19.14	12.36	5.61	7.92	$1.17 \cdot R_{chs}$
	26	20.22	13.17	6.40	8.77	$1.17 \cdot R_{chs}$
	27	21.72	14.40	7.22	9.84	$1.17 \cdot R_{chs}$

6.2.2 STATIC PRE-DISTORTION

The total degradation can be effectively decreased by means of pre-distortion for those ACM formats using APSK modulations (17-27). A static data pre-distorter (at the transmitter), as

the one in [7], was assumed for the simulations presented in this section. Such pre-distortion is basically a simple look-up table that transmits the constellation symbols with a fixed correction of the radii amplitudes and phases (computed off-line).

Figure 6-9 shows the total degradation for a subset of the ACM formats as function of the IBO, in particular ACM format 17 (16APSK), 22 (32APSK), and 27 (64APSK). For comparison the total degradation with ideal synchronization (results of Section 4.3.2) and without pre-distortion (previous section) have been reported. From the figure it can be seen that when using pre-distortion, the optimal IBO/OBO is approximately the same derived for ideal synchronization. In particular, an increase of 0.6 dB in OBO has been found as worst case. On the other hand, a performance loss between 0.7 dB and 1.0 dB has been found due to the synchronization when in presence of phase noise, Doppler, and nonlinear distortions.

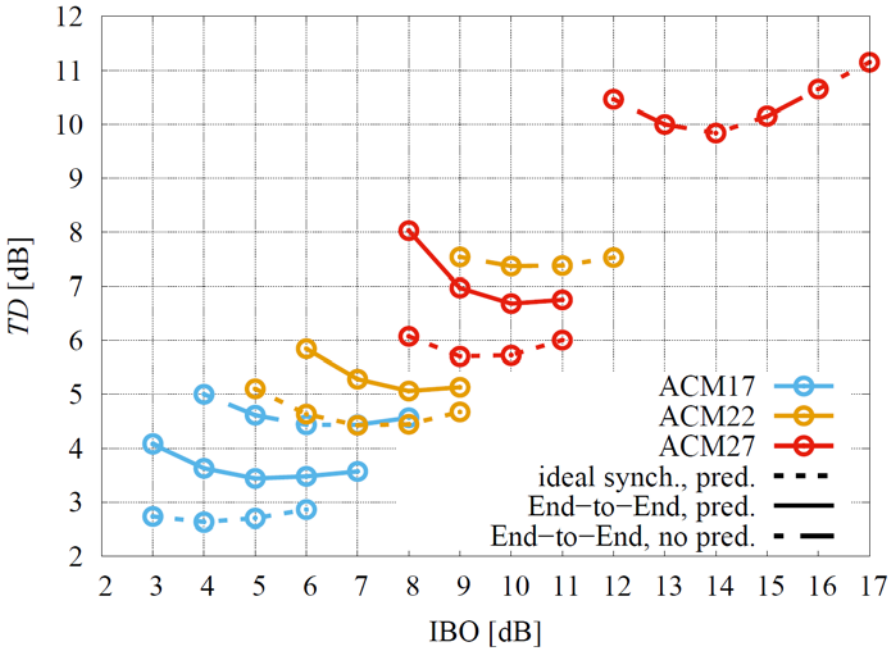

Figure 6-9: TD (end-to-end) for ACM formats 17, 22, and 27, with pre-distortion.

Similarly to previous section, the loss from ideal synchronization was investigated in detailed. In particular the loss w.r.t. ideal synchronization has been found due to two main components, the presence phase noise, and the use of a phase synchronizer operating on the FM and pilots (see previous section for detailed discussion on the phase synchronizer). This is proven by the example in Figure 6-10 that shows the CER for ACM format 27 when the different impairments are enabled one by one.

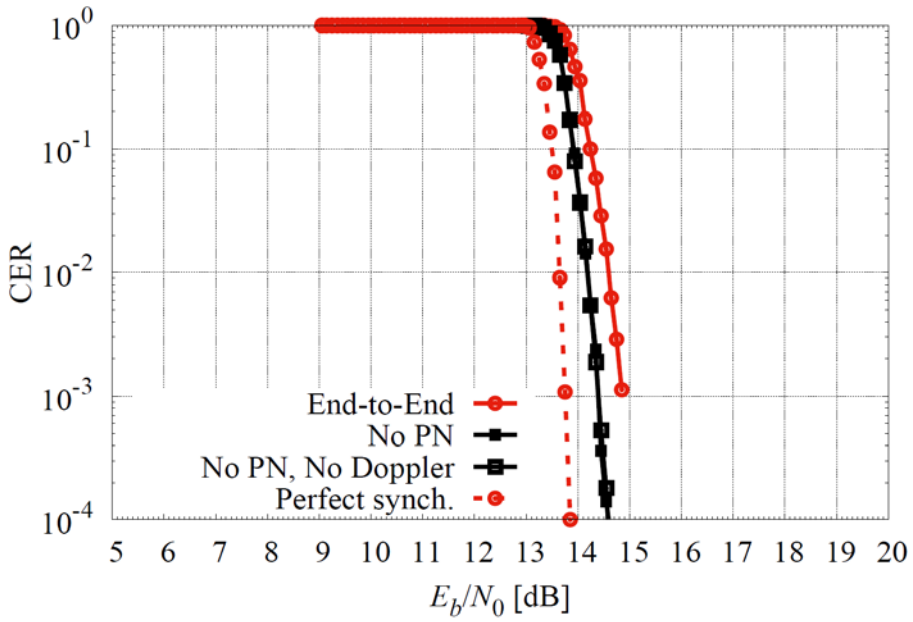

Figure 6-10: CER for ACM format 27, with static pre-distortion, IBO=9 dB, for different impairments.

Figure 6-11 and Figure 6-12 show the BER and CER for all the possible ACM using the optimal IBO found by means of the total degradation analysis. Finally, the SNR values for APSK modulations that allows a CER equal to 10^{-4} when static pre-distortion is adopted are summarized in Table 6-2. In the table is reported also the corresponding OBO, total degradation TD, and its gain w.r.t. the scenario without pre-distortion (i.e., Table 6-1).

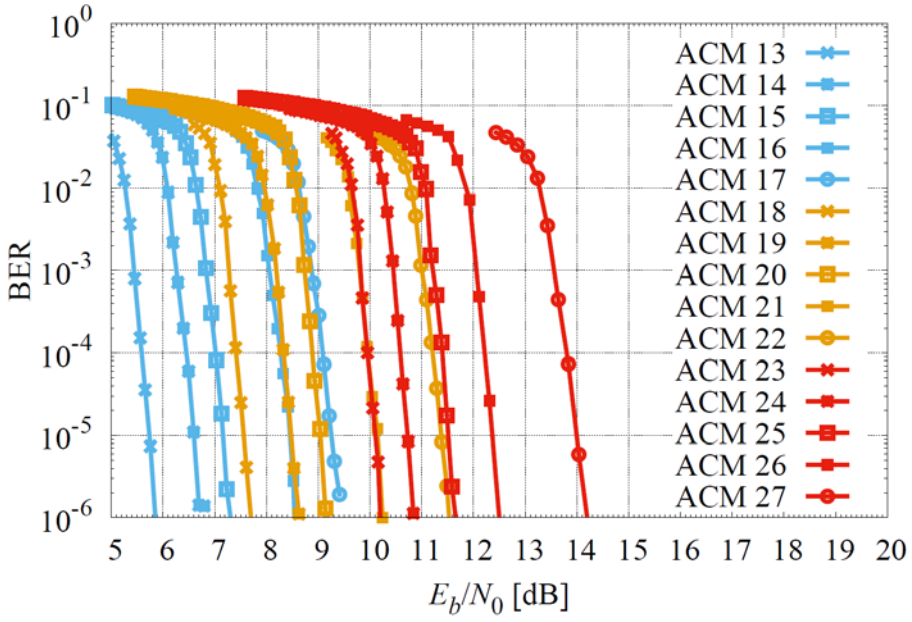

Figure 6-11: BER (end-to-end), with static pre-distortion, for ACM formats from 13 to 27 (APSK modulations) with the optimal IBO.

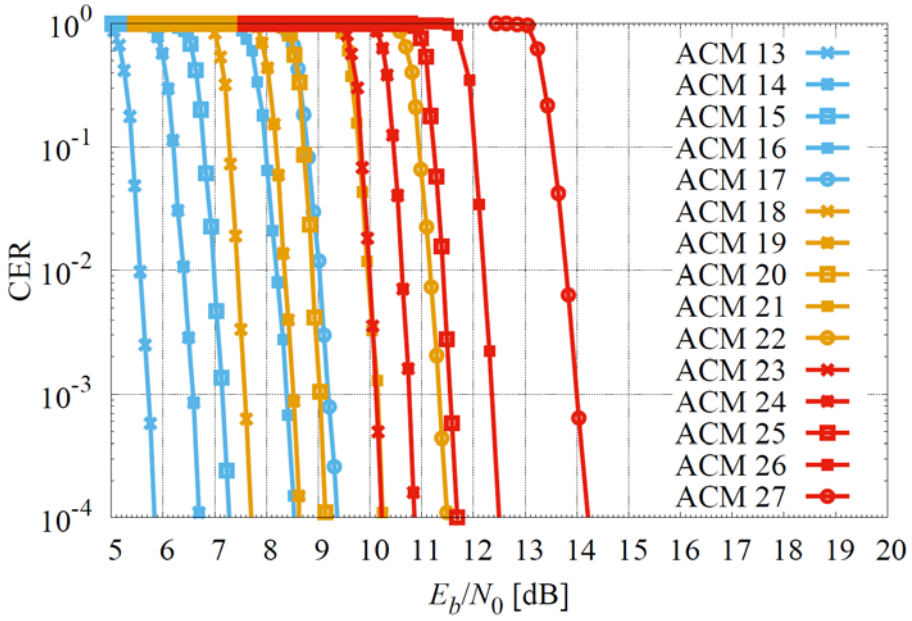

Figure 6-12: CER (end-to-end) , with static pre-distortion, for ACM formats from 13 to 27 (APSK modulations) with the optimal IBO.

Table 6-2: SNR thresholds for CER=1e-4, and corresponding OBO, TD, and bandwidth (for SRRC roll-off 0.35 after RF filtering), achieved by the recommended ACM formats with SRRC roll-off 0.35 in end-to-end simulations and with pre-distortion.

	ACM	E_s/N_0 [dB]	E_b/N_0 [dB]	OBO [dB]	TD [dB]	TD Gain [dB]	Bandwidth
16APSK	13	9.59	5.84	0.99	2.40	0.38	1.31· R_{chs}
	14	10.92	6.70	0.99	2.67	0.30	1.31· R_{chs}
	15	11.91	7.28	1.14	2.71	0.59	1.27· R_{chs}
	16	13.14	8.08	1.36	2.95	0.82	1.24· R_{chs}
	17	14.81	9.37	1.65	3.44	0.99	1.23· R_{chs}
32APSK	18	12.75	7.70	2.34	3.63	1.79	1.22· R_{chs}
	19	14.08	8.64	2.34	3.90	1.85	1.22· R_{chs}
	20	14.97	9.15	2.74	4.22	1.97	1.21· R_{chs}
	21	16.36	10.21	2.74	4.48	2.21	1.21· R_{chs}
	22	17.96	11.49	3.14	5.06	2.30	1.20· R_{chs}
64APSK	23	16.39	10.24	2.59	4.25	2.39	1.20· R_{chs}
	24	17.34	10.87	3.08	4.68	2.50	1.20· R_{chs}
	25	18.48	11.69	3.62	5.27	2.65	1.19· R_{chs}
	26	19.56	12.52	4.23	5.94	2.83	1.18· R_{chs}
	27	21.54	14.22	4.24	6.68	3.16	1.18· R_{chs}

7 TEST RESULTS

In this section, results of the compatibility testing between one transmitter and one receiver implementing CCSDS 131.2-B are reported. Out of the transmitter/receiver models developed under ESA contracts or other means, the tests reported herein refer to an Engineering Model transmitter (see Figure 7-1) developed by Tesat Spacecomm (DE) and one receiver developed by Konsberg Spacetec (NO) [15].

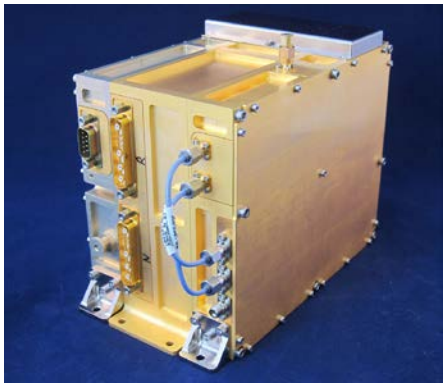

Figure 7-1: Tesat transmitter EM.

The test setup used in the measurement campaign is shown in Figure 7-2 and it includes a K-band TWTA (EM model) as well as a noise source and other elements as appropriate. The tests were performed at K-band (26.25 GHz), with a 500 MBaud signal generated by the EM transmitter, amplified by the TWTA, down-mixed to IF (1.2 GHz, where noise was added) and demodulated and decoded by the receiver.

The setup was used extensively for the verification of the EM transmitter and the receiver. A minimal subset of results is reported here, for information.

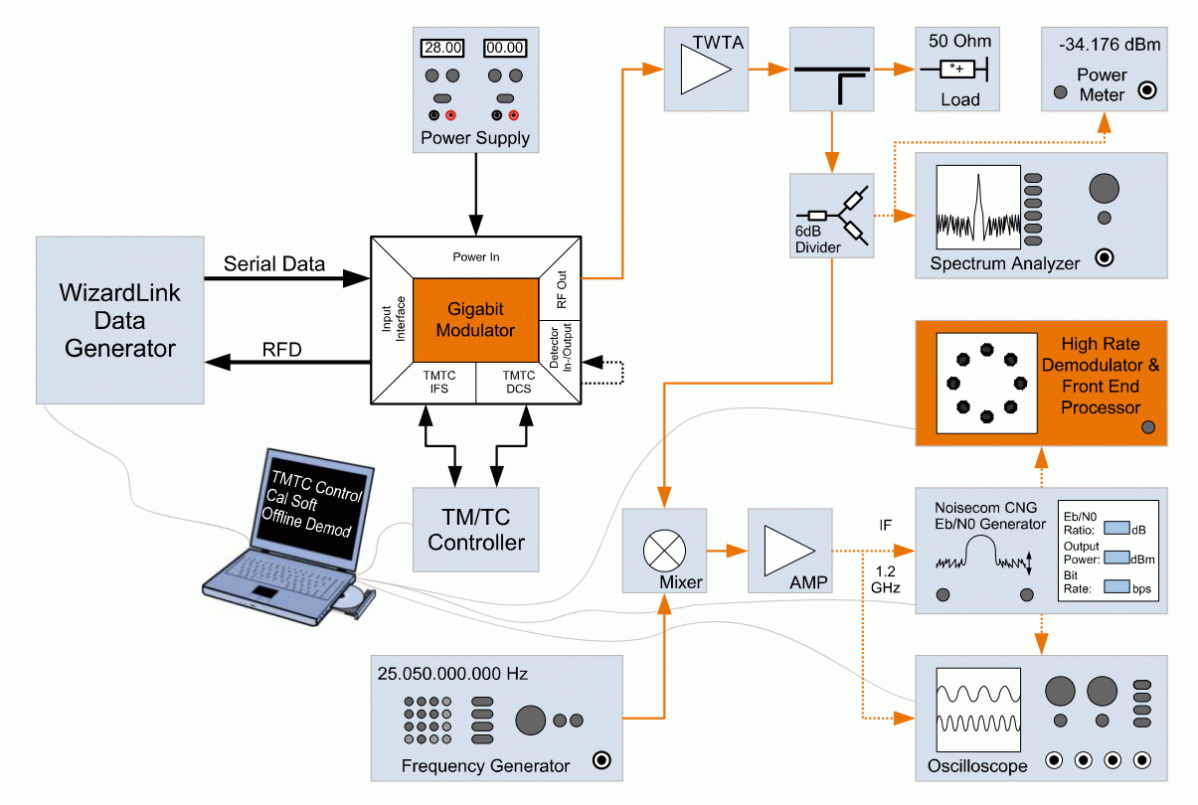

Figure 7-2 End-to-end test setup.

A scatter plot obtained with 64-APSK modulation is shown in Figure 7-3, comparing the results over a linear channel (w/o TWTA) with the measurement taken with the TWTA (back-off of 2.8 dB). The modulator employed a digital pre-distortion technique with better performance than the one used for the simulations shown in the previous section.

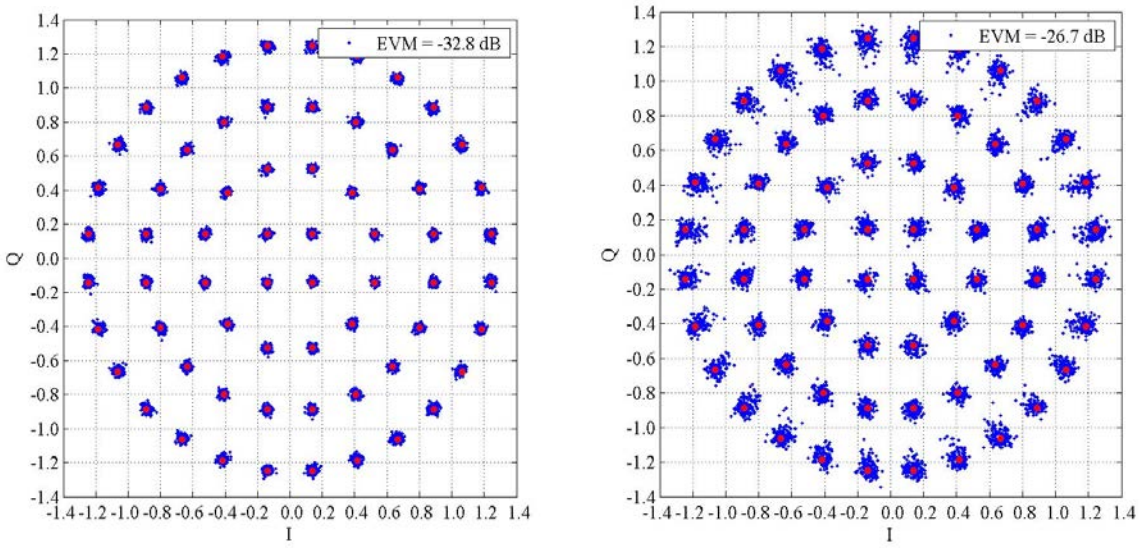

Figure 7-3 Modulator in 64-APSK mode, without TWTA (left-side) and with TWTA (2.8 dB back-off).

The modulator phase noise was measured in different configurations (e.g. central frequencies) resulting always lower that 1 deg rms when integrated between 10 kHz and 250 MHz. As an example, a snapshot of the phase noise measurement taken for a central frequency of 26.25 GHz is shown in Figure 7-4.

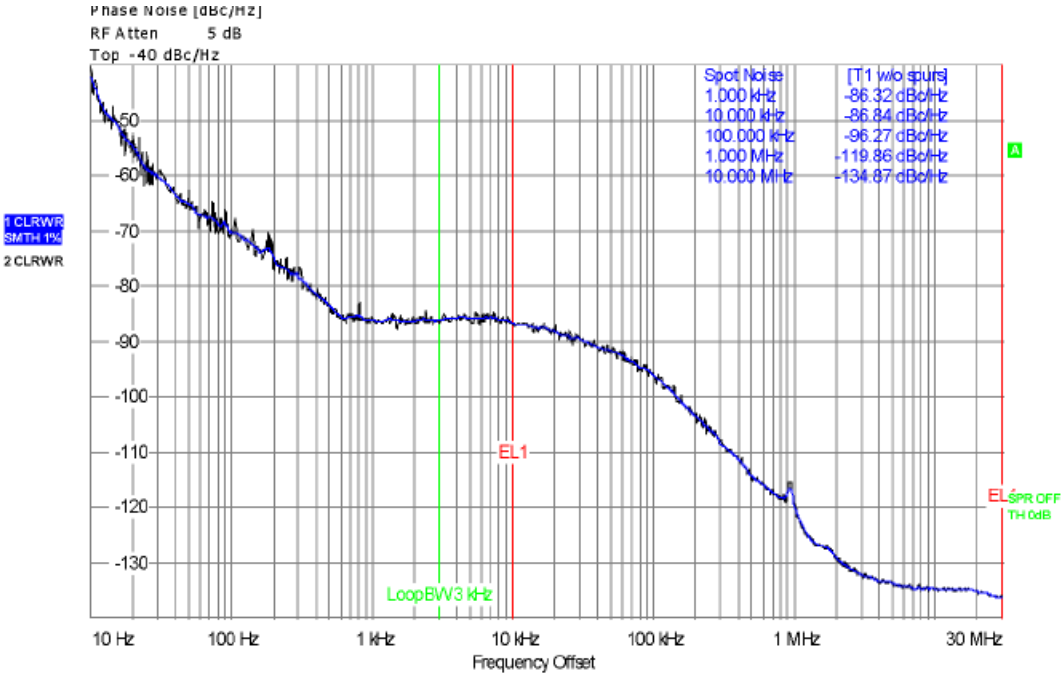

Figure 7-4 Modulator phase noise (26.25 GHz, ambient).

Bit error rate measurement results are shown in Figure 7-5, where one ModCod for each modulation order is included, with channel symbol rate set at 500 MBaud. Different back-off values are used for the different modulations, with a maximum of 2.8 dB for the 64-APSK case.

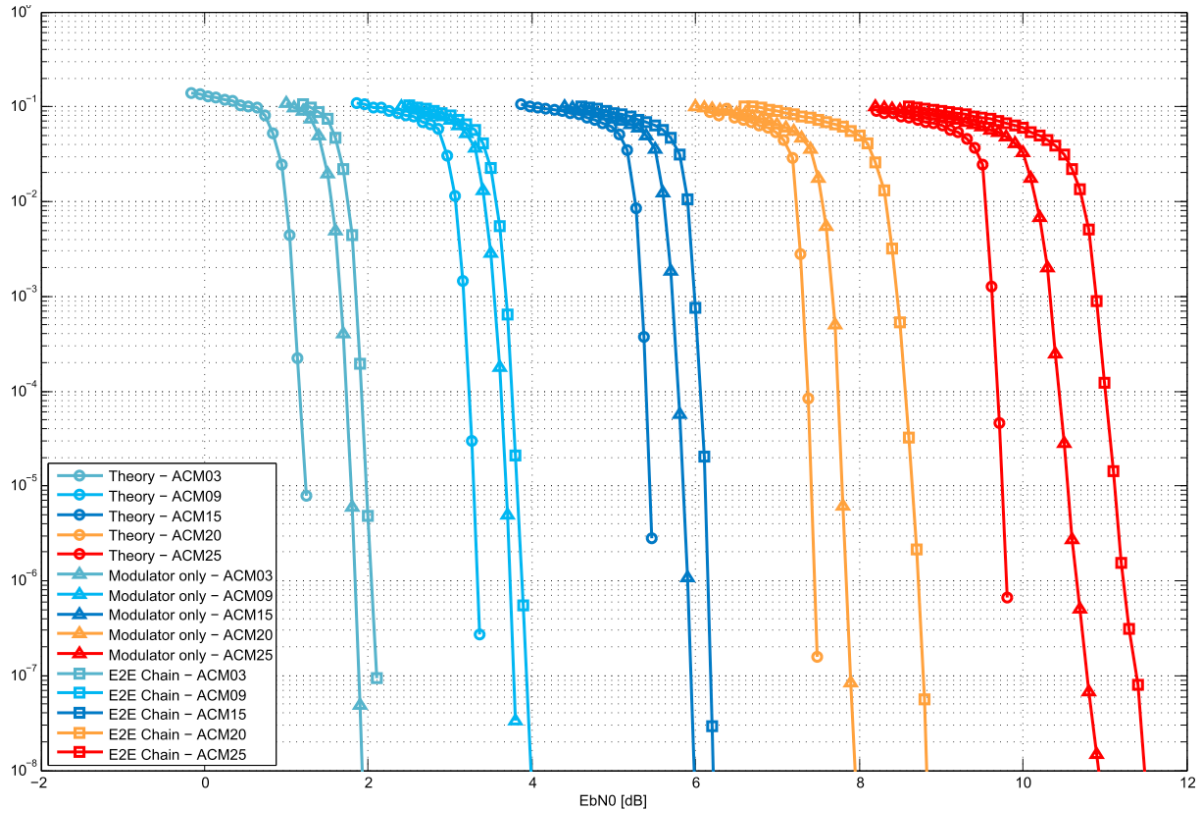

Figure 7-5 BER performance.

Reference[4] results (without impairments other than Gaussian noise) are compared with the actual measurement taken with or without the TWTA in the chain. The latter case shows the overall (transmitter/receiver) implementation losses as well as the impact of phase noise and other imbalances, while the formal shows the degradation introduced the non-linear amplification (the back-off should be added to this to obtain the total degradation as used in previous section).

[4] Tesat proprietary simulation model.

8 CONCLUSIONS

This Report provided additional informative material for [1].

Section 2 covered a tutorial overview of CCSDS specification in [1] with description of the main functions and parameters.

Section 3 assessed the performance of the recommended codes and modulations by means of BER/CER curves on the AWGN channel assuming ideal synchronization.

Section 4 provided the performance of the recommended codes and modulations in presence of a nonlinear distortions, aimed at modelling nonlinear effects due to amplification. A preliminary optimization of the IBO/OBO, and assessment of occupied bandwidth (99% of the signal power) was carried out, and performance reported by means of BER/CER curves. The same section also showed that pre-distortion at the transmitter can improve noticeably the performance for those ACM formats using APSK modulations.

Section 5 focused on the synchronization for the recommended codes and modulations. A possible synchronization chain was provided and performance evaluated on the linear AWGN channel in presence of phase noise, Doppler shift, and Doppler rate. The section showed that synchronization can be achieved with a loss less than 0.4 dB with respect AWGN results.

Finally, Section 6 provided performance of the full chain (end-to-end) when the channel is nonlinear as in Section 4, and the synchronization chain adopted is the one in Section 5. The section showed that in absence of pre-distortion, the AM/PM effect can impair the phase synchronization, causing huge performance losses on the ACM formats using APSK modulations (especially 64APSK). Differently, if pre-distortion at the transmitter is adopted, the performance analysis showed on the nonlinear channel a loss (worst case) limited to 1 dB with respect ideal synchronization. Hence, the use of pre-distortion at the transmitter appeared mandatory. As a validation of the simulation campaign, Section 7 reported a subset of the results obtained with an extensive test campaign performed for the performance validation of one transmitter model and one receiver developed under ESA contracts.

ANNEX A

FLL tuning for the reference receiver

This Annex shows the detailed analysis that has been carried out for tuning the FLL presented in Section 5.6 that, for the reader's convenience, the linearized model is shown again in Figure A-1.

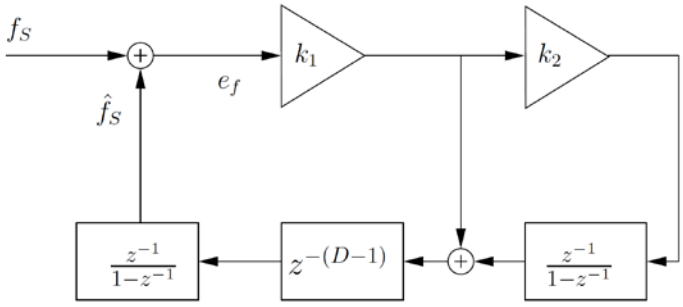

Figure A-1: Linearized scheme of the adopted FLL.

The FLL has been first tested considering $k_2 = 0$, i.e., a FLL of the first type, to see if the residual frequency error due to Doppler rate is still acceptable. As mentioned, the FLL operates almost in noise-free condition, hence when considering a FLL of the first type the coefficient k_1 can be selected as the value providing the best convergence and stability. This can be easily done by means of the root locus as shown in Figure A-2, where it is shown that for $k_1 \in [0,0.25]$ the roots are real and they provide a damped convergence, while for $k_1 \in [0.25,1.0)$ the roots are complex conjugate and the response is undamped. Figure A-3, shows exactly this behavior when the FLL with FFT-based frequency detector is simulated for the ACM format 1 at low SNR ($E_s/N_0 = -0.9$ dB, i.e., $E_b/N_0 = 0.6$ dB for ACM format 1). Hence, for tuning the first-type FLL, $k_1 = 0.2$ was selected.

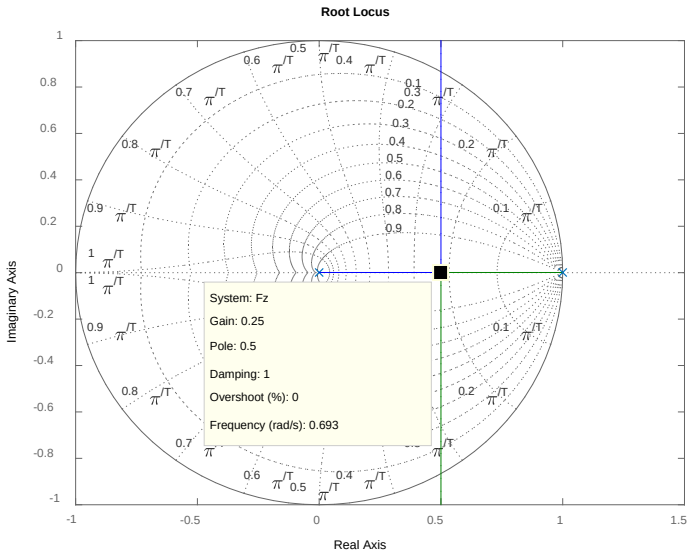

Figure A-2: Root locus for the first-type FLL.

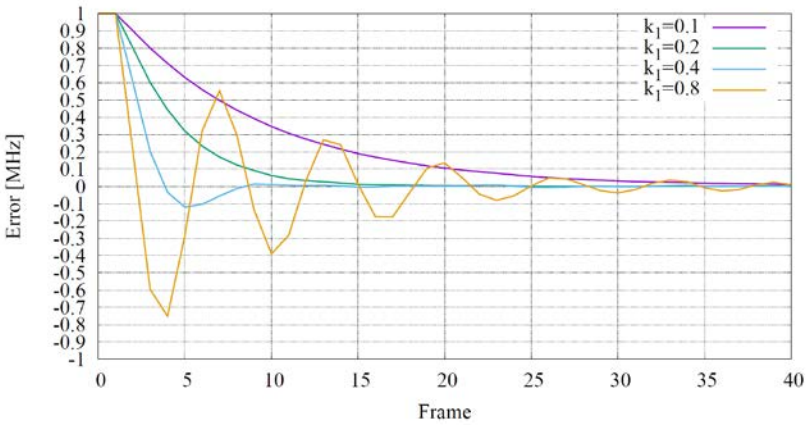

Figure A-3: Simulated frequency error convergence at Es/N0=-0.9 dB (Eb/N0=0.6 dB for ACM1).

Once the FLL first-type has been tuned, the residual error due to Doppler rate was assessed. It can be shown that for this FLL the error is given by

$$e_f = \frac{f_{\mathrm{R}}}{k_1 R_{FM}} \quad ,$$

where R_{FM} is the number of FM per second, i.e. $R_{FM} = R_{chs}/133760$ (when using pilot fields), and f_{R} is the Doppler rate. Hence, when considering a Doppler rate (worst case) of 50 kHz/s, and channel symbol rate $R_{chs} = 100$ MBaud, it holds that the residual error e_f when using a FLL of the first type is

$$e_f < 334.4 \text{ Hz}$$

Normally this could require the use of second-type FLL. However, the adopted phase estimator (see Section 5.5), because of the linear interpolation, can correct a residual frequency error as long as this is under the maximum slope of the linear interpolation. As already discussed, the linear interpolation is able to interpolate a maximum phase variation of $\pm\pi$ over 540 channel symbols. Hence, the maximum residual frequency error acceptable at the phase synchronizer is given by

$$\frac{1}{2\pi} \cdot \frac{\pi R_{chs}}{540} = 92.6 \text{ kHz} \quad .$$

Notice that this value is well above the residual error $e_f = 334.4$ Hz, meaning that a first-type FLL with $k_1 = 0.2$ and $k_2 = 0$ is sufficient for the considered scenarios.

As further proof, simulations of the full synchronization chain were done for checking the maximum acceptable Doppler rate. Figure A-4 shows the measured residual frequency error as function of the time (reported as PL frame number) at $E_s/N_0 = -0.9$ dB when using a triangular Doppler profile (see Section 5.1) with Doppler shift $f_{\mathrm{D}} = 1$ MHz and increasing Doppler rate f_{R}. For comparison the figure also shows the maximum residual frequency error by the phase synchronizer that has been formulated as 92.6 kHz. From the figure it can be seen that Doppler rate even up to 7 MHz/s are well inside the theoretical limit, whereas only Doppler rate values as high as 12 MHz/s could cause a loss of synchronization. This has been

confirmed by means of CER curves as shown in Figure A-5 and Figure A-6 for ACM format 1 and 27 respectively.

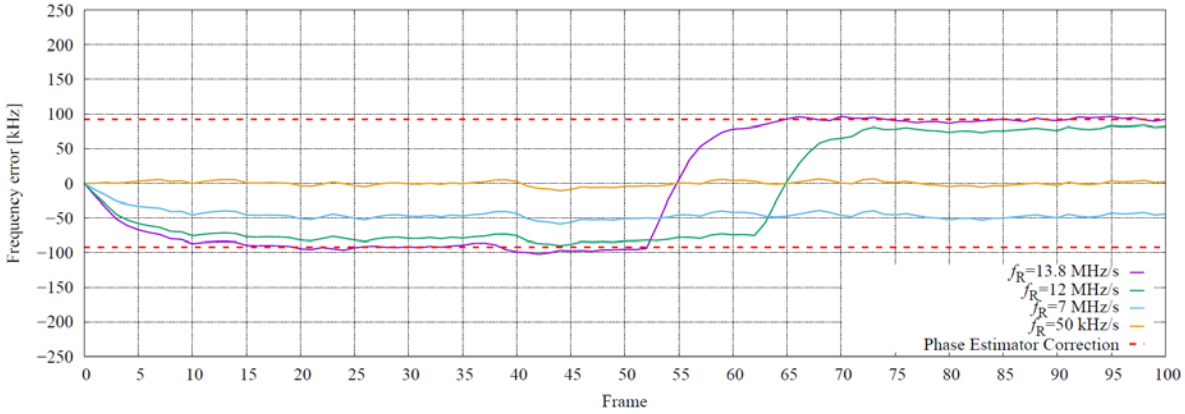

Figure A-4: Frequency error convergence for first-type FLL ($k_1 = 0.2$), at Es/N0=-0.9 dB, and triangular Doppler profile with $f_D = 1$ MHz and increasing Doppler rate f_R.

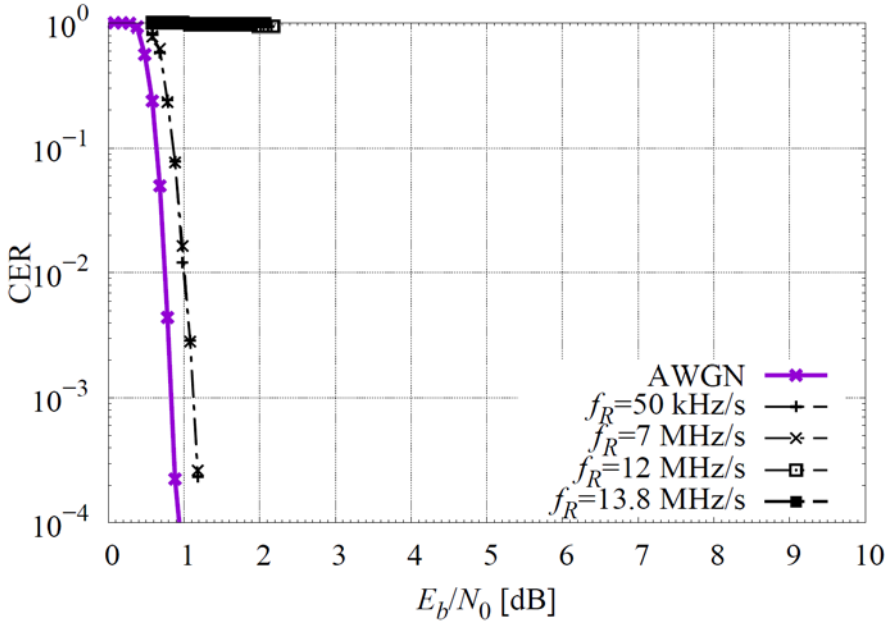

Figure A-5: CER for ACM format 1, triangular Doppler profile with $f_D = 1$ MHz and increasing Doppler rate f_R, first-type FLL ($k_1 = 0.2$).

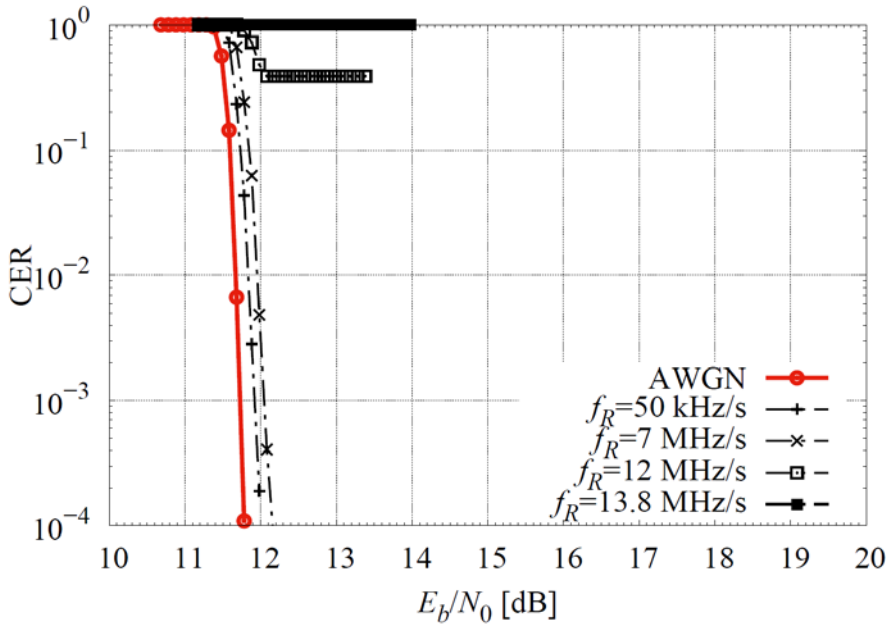

Figure A-6: CER for ACM format 27, triangular Doppler profile with $f_D = 1$ MHz and increasing Doppler rate f_R, first-type FLL ($k_1 = 0.2$).

The simulation has been repeated also with the sinusoidal Doppler profile (see Section 5.1) with Doppler shift $f_D = 1$ MHz and increasing Doppler rate f_R, and results are shown in Figure A-7, Figure A-8, and Figure A-9. It can be seen that similar conclusion holds.

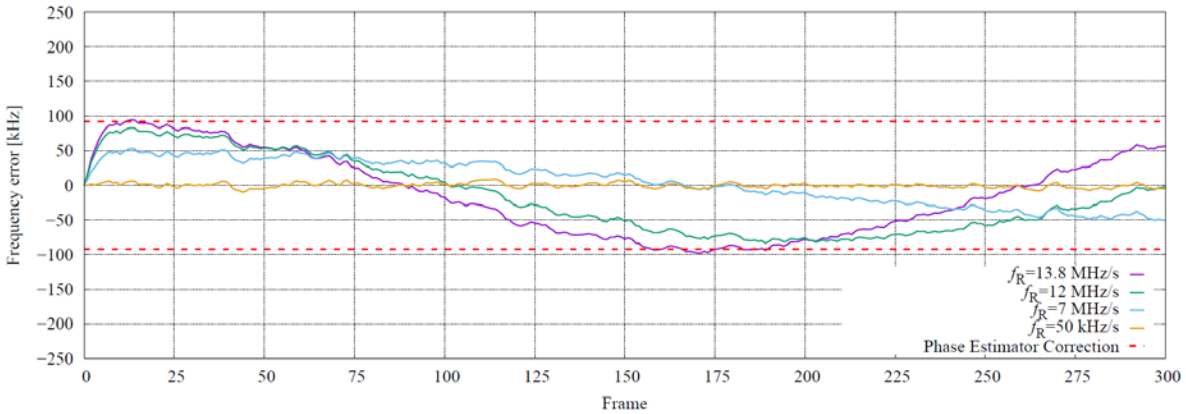

Figure A-7: Frequency error convergence for first-type FLL ($k_1 = 0.2$), at Es/N0=-0.9 dB, and sinusoidal Doppler profile with $f_D = 1$ MHz and increasing Doppler rate f_R.

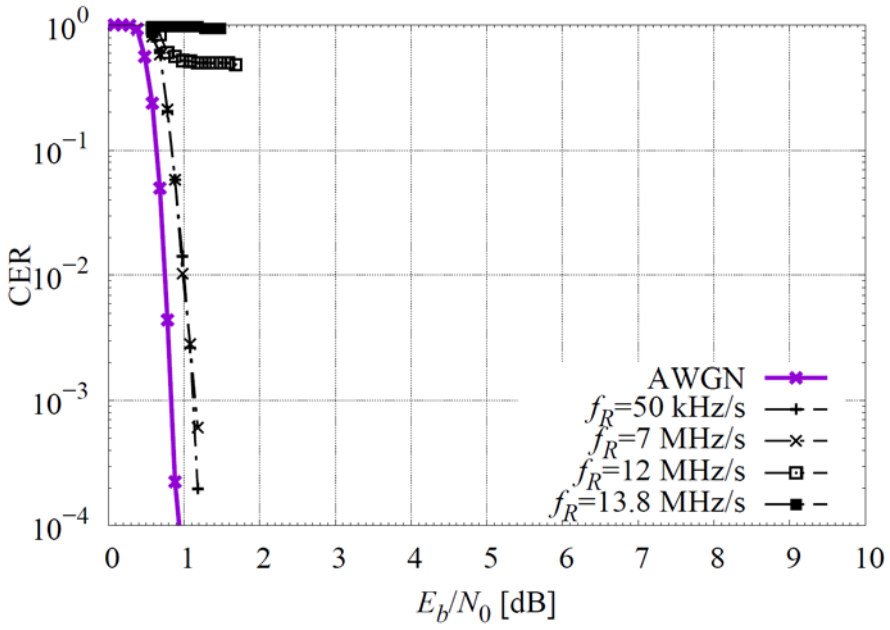

Figure A-8: CER for ACM format 1, sinusoidal Doppler profile with $f_D = 1$ MHz and increasing Doppler rate f_R, first-type FLL ($k_1 = 0.2$).

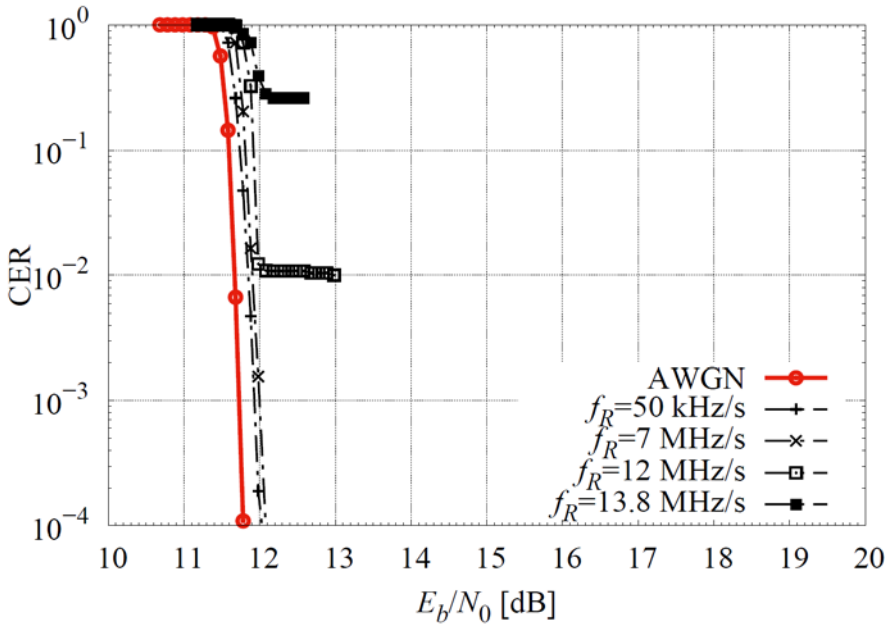

Figure A-9: CER for ACM format 27, sinusoidal Doppler profile with $f_D = 1$ MHz and increasing Doppler rate f_R, first-type FLL ($k_1 = 0.2$).

As final cross-check (reported for reader's reference) simulation by using a second-type FLL have been also carried out. Figure A-10 shows the measured residual frequency error as function of the time (reported as PL frame number) at $E_s/N_0 = -0.9$ dB when using a sinusoidal Doppler profile, while Figure A-11 and Figure A-12 the corresponding CER

curves. It can be seen that the use of a second-type FLL, as expected, decreases the residual frequency error due to the Doppler rate improving resilience, although this improvement is not required for the considered scenarios.

In conclusion, it has been found analytically and by simulations that for the considered scenarios a first-type FLL is more than sufficient, even in presence of a Doppler rate of 50 kHz/s. This is possible thanks to the adopted phase synchronizer that is able to correct residual frequency errors well above the maximum residual error estimated for the adopted FLL.

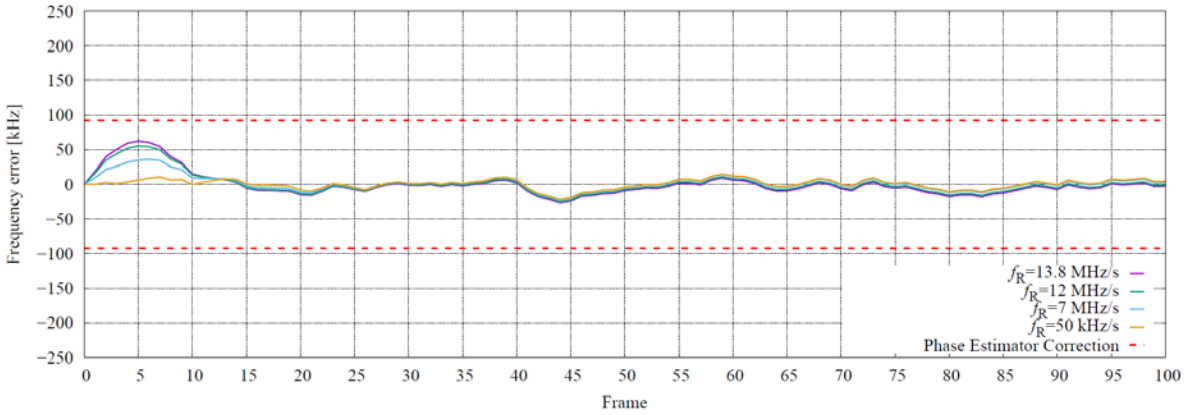

Figure A-10: Frequency error convergence for second-type FLL ($k_1 = 0.32, k_2 = 0.16$), at Es/N0=-0.9 dB, and sinusoidal Doppler profile with $f_D = 1$ MHz and increasing Doppler rate f_R.

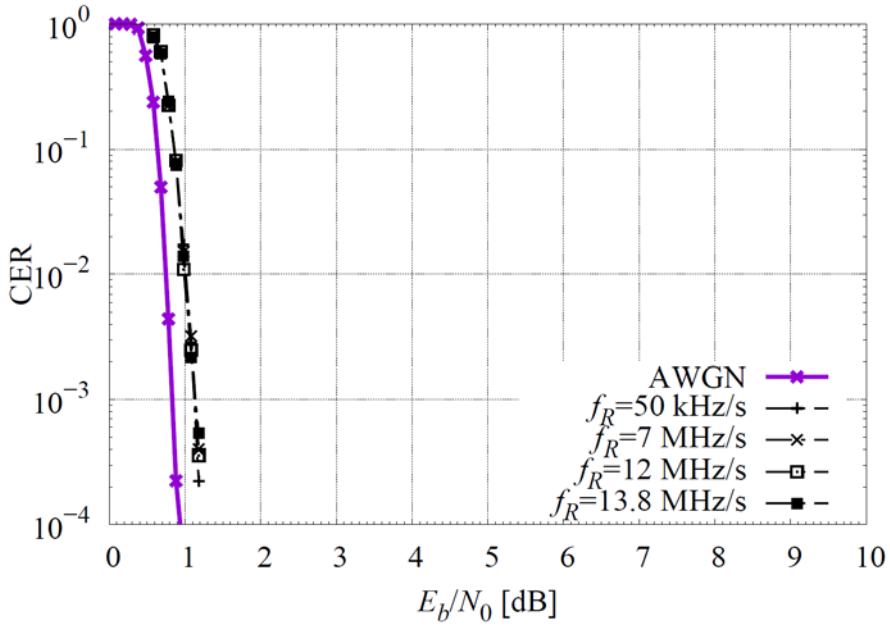

Figure A-11: CER for ACM format 1, sinusoidal Doppler profile with $f_D = 1$ MHz and increasing Doppler rate f_R, second-type FLL ($k_1 = 0.32, k_2 = 0.16$).

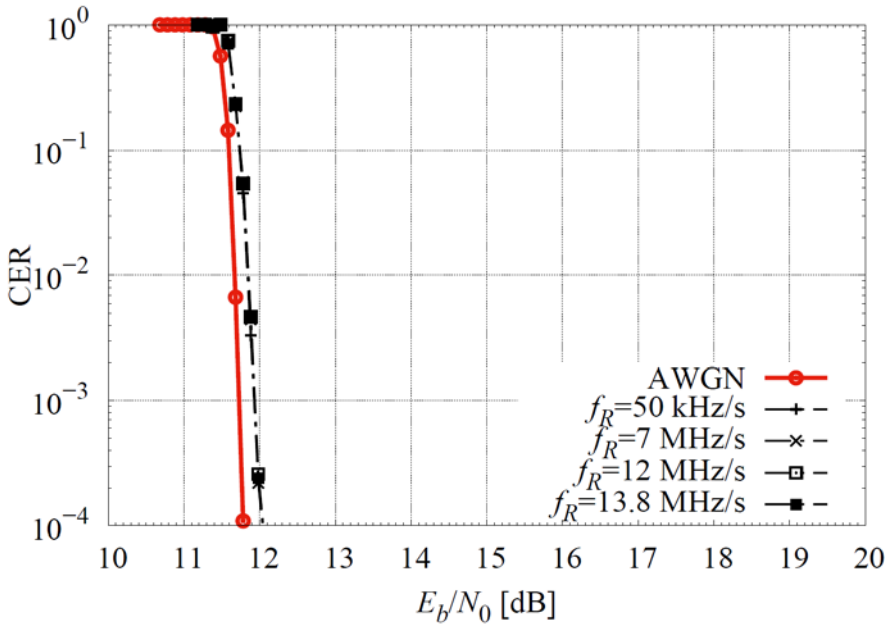

Figure A-12: CER for ACM format 27, sinusoidal Doppler profile with $f_D = 1$ MHz and increasing Doppler rate f_R, second-type FLL ($k_1 = 0.32, k_2 = 0.16$).